

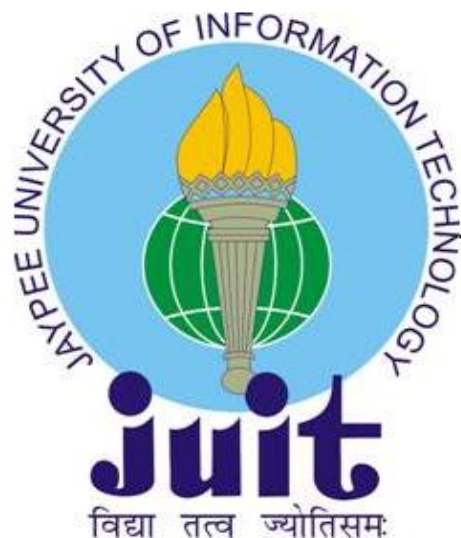
SEMICONDUCTING BINARY AND ALLOYED SILVER CHALCOGENIDE QUANTUM DOTS: STRUCTURAL, MORPHOLOGICAL AND OPTICAL BAND GAP TUNING

Thesis submitted in fulfillment of the requirements for the Degree of

DOCTOR OF PHILOSOPHY

By

SUBHASH CHAND



DEPARTMENT OF PHYSICS AND MATERIALS SCIENCE
JAYPEE UNIVERSITY OF INFORMATION TECHNOLOGY
WAKNAGHAT, DISTRICT SOLAN, H.P., INDIA

JUNE 2019

Copyright

@

JAYPEE UNIVERSITY OF INFORMATION TECHNOLOGY

WAKNAGHAT

JUNE 2019

ALL RIGHTS RESERVED

CONTENTS

Cover page	<i>i</i>
Copyright	<i>ii</i>
Table of contents	<i>iii-vi</i>
Declaration by the Scholar	<i>vii</i>
Supervisor's certificate	<i>ix</i>
Acknowledgement	<i>xi-xiv</i>
Abstract	<i>xv</i>
List of abbreviations	<i>xvii-xviii</i>
List of figures	<i>xix-xxii</i>
List of tables	<i>xxiii-xxiv</i>
List of publications	<i>xxv</i>
CHAPTER-1	1-30
Introduction	
1.1 Nanotechnology	
1.2 Quantum dots	
1.2.1 Quantum confinement effects	
1.2.1.1 The exciton	
1.2.1.2 Frenkel excitons	
1.2.1.3 Wannier–Mott excitons	
1.2.1.4 Charge-transfer excitons	
1.2.1.5 Surface excitons	
1.2.2 Effective Mass Approximation for defining quantum confinement effect	
1.2.3 Quantum dots stability factors	
1.2.3.1 Size control	
1.2.3.2 Stabilization	
1.2.3.2.1 Steric stabilization	
1.2.3.2.2 Electrostatic stabilization	
1.3 Properties of quantum dots	
1.3.1 Optical properties	

- 1.3.2 Electrical properties
- 1.3.3 Structural properties
- 1.4 Literature survey
- 1.5 Applications of silver chalcogenide QDs
 - 1.5.1 Solar cells applications
 - 1.5.2 Quantum computation and quantum information processing
 - 1.5.3 Biological applications
 - 1.5.4 Light emitting diodes
 - 1.5.5 Counterfeiting applications
 - 1.5.6 Thermoelectric applications
 - 1.5.7 Photonic devices
 - 1.5.8 Photocatalysts
- 1.6 Motivation of thesis work
- 1.7 Outline of the thesis

CHAPTER-2

31-56

Experimental details

- 2.1 Synthesis of quantum dots
 - 2.1.1 Top to down approach
 - 2.1.2 Down to up approach
 - 2.1.2.1 Wet chemical methods
 - 2.1.2.1.1 Sol-gel approach
 - 2.1.2.1.2 Hot injection approach
 - 2.1.2.1.3 Arrested precipitation (co-precipitation) approach
 - 2.1.2.1.4 Hydrothermal method
 - 2.1.2.1.5 Cation-exchange of QDs
 - 2.1.2.1.6 Vapour phase method or molecular beam epitaxy (MBE)
- 2.2 Characterization technique
 - 2.2.1 X-ray diffractometer
 - 2.2.2 Transmission electron microscopy (TEM)

2.2.3 Energy dispersive X-ray spectroscopy (EDX or EDS)

2.2.4 Optical characterizations

2.2.4.1 UV-VIS-NIR Spectrophotometer

2.2.4.2 Fourier transforms infrared spectroscopy (FTIR)

2.2.4.3 Raman spectroscopy

2.3 Some relevant equations

CHAPTER-3

57-72

Optimization of conditions for the synthesis of Ag₂Se QDs

3.1 Introduction

3.2 Synthesis and characterization of Ag₂Se nanoparticles

3.2.1 Experimental details

3.2.2 Structural properties

3.3 Synthesis and characterization of Ag₂Se QDs

3.3.1 Experimental details

3.3.2 Structural properties

3.3.3 Optical properties

3.4 Conclusion

CHAPTER-4

73-84

Structural, morphological and optical properties of co-precipitated Ag₂S QDs

4.1 Introduction

4.2 Experimental details

4.3 Results and discussion

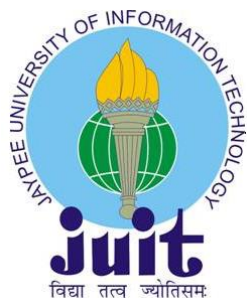
4.3.1 Structural properties

4.3.2 Morphology of QDs

4.3.3 Optical properties

4.3.3 .1 UV-VIS-IR spectroscopy

	4.3.3.2 Raman spectroscopy	
	4.4 Conclusion	
CHAPTER-5		85-102
	Structural, morphological and optical properties of co-precipitated alloyed $\text{Ag}_2\text{Se}_x\text{S}_{1-x}$ QDs	
	5.1 Introduction	
	5.2 Experimental details	
	5.3 Results and discussion	
	5.3.1 Reaction mechanism	
	5.3.2 Structural properties	
	5.3.3 Morphology of QDs	
	5.3.4 Optical properties	
	5.3.4.1 UV-VIS-NIR spectroscopy	
	5.3.4.2 Raman spectroscopy	
	5.4 Conclusion	
CHAPTER-6		103-108
	Summary and future scope	
	6.1 Summary	
	6.2 Future work	
BIBLIOGRAPHY		109-133



JAYPEE UNIVERSITY OF INFORMATION TECHNOLOGY

(Established by H.P. State Legislative vide Act No. 14 of 2002)
Dumehar Bani, Kandaghat, Distt. Solan – 173234 (H.P.) INDIA

Website: www.juit.ac.in

Phone No. (91) 07192-257999 (30 Lines)

Fax: (91) 01792 245362

DECLARATION

I hereby declare that the work contained in the Ph.D. thesis entitled **“SEMICONDUCTING BINARY AND ALLOYED SILVER CHALCOGENIDE QUANTUM DOTS: STRUCTURAL, MORPHOLOGICAL AND OPTICAL BAND GAP TUNING”** is original and has been done by me under the supervision of Dr. Pankaj Sharma (Supervisor) submitted to **Jaypee University of Information Technology, Wagnaghat, India**. The work has not been submitted to any other organization for any degree or diploma.

SUBHASH CHAND

Enrollment Number-156951

Department of Physics and Materials Science

Jaypee University of Information Technology

Wagnaghat, Solan, H.P. India-173234

Dated:



JAYPEE UNIVERSITY OF INFORMATION TECHNOLOGY

(Established by H.P. State Legislative vide Act No. 14 of 2002)
Dumehar Bani, Kandaghat, Distt. Solan – 173234 (H.P.) INDIA

Website: www.juit.ac.in

Phone No. (91) 07192-257999 (30 Lines)

Fax: (91) 01792 245362

CERTIFICATE

This is to certify that the work reported in the Ph.D. thesis entitled **“SEMICONDUCTING BINARY AND ALLOYED SILVER CHALCOGENIDE QUANTUM DOTS: STRUCTURAL, MORPHOLOGICAL AND OPTICAL BAND GAP TUNING”**, which is being submitted by **Mr. Subhash Chand** for the award of degree of Doctor of Philosophy from the Department of Physics and Materials Science by Jaypee University of Information Technology, Waknaghat, India, is the record of the candidate’s own work, carried out under my supervision. This work has not been submitted partially or wholly to any other university or institute for the award of this or any other degree or diploma.

Dr. Pankaj Sharma

Supervisor

Associate Professor

Department of Physics and Materials Science

Jaypee University of Information Technology

Waknaghat, Solan, H.P. India-173234

Dated:



**DEDICATED TO
MY BELOVED
PARENTS &
FAMILY**

ACKNOWLEDGEMENTS

GOD is my ultimate strength and power who bring best out of me

I deem it my privilege and honors to consign my appreciation and thanks to the following without whose supervision, support and apprehension I would not have been able to complete my Ph. D thesis.

*I feel fortunate to convey my deep sense of reverence and gratitude to my revered mentor, **Dr. Pankaj Sharma**, for his support, immaculate guidance, constructive criticism, constant encouragement and providing requisite facilities to persist my research which otherwise would have remained incomplete. His nurturing and gentle concern has been a stimulus which I will always cherish. I also appreciate his untiring efforts during the entire tenure of my research work and patience during writing of this thesis. I have no words to express my gratitude for everything he has contributed in my Ph.D and without his blessings it was surely impossible for me to finish my work. I thank him from bottom of my heart.*

*I emphatically express my loyal and venerable thanks to **Prof. (Dr.) Vinod Kumar** (Vice Chancellor, JUIT), **Prof. (Dr.) Samir Dev Gupta** (Director & Academic Head, JUIT) for giving an opportunity to pursue Doctorate Degree. I would like to thank **SERB-DST** vide project grant number EMR/2014/001108 for providing me fellowship.*

*I gratefully acknowledge the help rendered by **Prof. P. B. Barman** (HOD, Department of Physics and Materials Science) for his encouragement, timely help and cooperation throughout my research work. It gives me immense pleasure to express my gratitude to him for his positive disposition coming to my rescue in solving my problems and suggestions which helped me in maintaining my confidence.*

*This document would have remained an infant had it not received its necessary 'diet' in the form of comments, suggestions etc. by **Dr. Vineet Sharma, Prof. (Dr.) Sunil Kumar Khah, Dr. Vivek Kumar Sehna, Dr. Surajit Kumar Hazra, Dr. Dheeraj Sharma, Dr. Rajesh Kumar, Dr. Ragini Raj Singh, and Dr. Sanjiv Kumar Tiwari.***

*I appreciatively acknowledge the help rendered by **Prof. Nagesh Thakur** and **Prof. Nainjeet Singh Negi** (Department of Physics, Himachal Pradesh University, Summer Hill, Shimla), **Prof. (Dr.) Ravi Kumar** (Department of Material Science and Engineering, NIT Hamirpur), **Dr. Manoj Kumar** (Department of Physics and Material*

Science, Jaypee Institute of Information Technology, Noida) for their stimulating suggestions and huge help throughout my whole research work.

I am also grateful to all the members of technical and non-technical staff of the department **Er. Kamlesh Mishra, Mr. Ravendra Tiwari and Mr. Deepak Singh** for their help and precious assistance.

I am fortunate to have seniors and friends who have always stood beside me. I extend my heartfelt thanks to my best friends and colleagues **Vinod Kumar, Sunil Kumar, Rohit Sharma, Prasahant Thakur, Manoj Kumar, Birender Thakur, Tejender, Sanjeev, Hitesh, Avinsh, Amit and Prag**, and who have always been listened my insane thoughts and ideas in spite of not understanding a bit of it. I am also grateful to my Seniors **Dr. Hitanshu Kumar, Dr. Rajinder, Dr. Dikshita Gupta, Dr. Bandna Bharti, Dr. Rajender Singh, Dr. Pawan, Dr. Rohit Randhawa, Mr. Hakikat Sharma, Mr. Desh Raj and Mrs. Neha Sharma** for being there so as to make me sail through all the twists and turns of this journey. It is my pleasure to express my gratitude to **Jonny Dhiman, Neha Kondal, Kavita, Sampan Attri, Dr. Rishi Mahajan, Asha, Dipti Rawat, Ekta Sharma, Rajan Sharma, Sanjay Kumar Shandil, Kanchan Thakur, Neha, Priyanka Sharma, Shikha Sinha, Anuradha, Achyut Sharma, Pooja, Swati Sharma, Deepak Sharma, Keshav Kondal** and all the research scholars of the JUIT for keeping me blessed with best wishes. I would like to thank my all students for to provide me positive energy. The time spent with them will be cherished throughout my life. I would like to thank every person who gave me positive and negative experience throughout my life.

The intention of this acknowledgement will be imperfect if I fail to appreciate the moral support and encouragement rendered by the most important person of my life i.e. my **parents and sister (Kanchan Thakur)** who has always been my inspiration and never let me felt abandoned. It was their blessings and love which constantly motivated me and helped in the successful completion of my research work. I would like to express my heartfelt gratitude to all those who have contributed directly or indirectly towards obtaining my doctorate degree and apologize if have missed out anyone.

SUBHASH CHAND

DATE

ABSTRACT

The eco-friendly quantum dots (QDs) are useful for the conversion of solar radiations to electrical energy due to their unique properties *i.e.* multiple electron generation, effective charge transfers, bandgap tuning. Silver-based QDs are comparatively eco-friendly than lead and cadmium based QDs. Silver selenide (Ag_2Se) QDs are synthesized by optimizing various parameters in co-precipitation approach. The bandgap of Ag_2Se decreases from 1.8 eV to 0.99 eV with the increase in the size from 5 nm to 31.6 nm. The hydrothermal approach is also tested but the size obtained is beyond QD size. So, co-precipitation approach is used for further synthesis. The size of co-precipitated silver sulphide (Ag_2S) changes from 24.1 ± 10 nm to 4.8 ± 0.75 nm with synthesis time from 5 minutes to 60 minutes. The size calculated by transmission electron microscopy (TEM) and Brus equation is in good agreement. Quantum confinement (QC) arises with the phase-change as confirmed by X-ray diffraction (XRD) and Raman spectra. The size of co-precipitated selenium alloyed $\text{Ag}_2\text{Se}_x\text{S}_{1-x}$ ($x = 0, 0.4, 0.6$ and 1.0) QDs calculated using Williamson-Hall plot, TEM and Brus equation is in good agreement. The redshift in first exciton peak of UV-VIS-NIR spectroscopy indicate QC. The bandgap (Tauc plot) of $\text{Ag}_2\text{Se}_x\text{S}_{1-x}$ QDs decrease from 1.3 eV to 0.88 eV showing QC depends upon size and composition. Raman spectra show the formation of the desired alloyed structure. The synthesized QDs may be suitable for devices requiring QC that are influenced by even a little change in size.

ABBREVIATIONS

QD	Quantum dot
QW	Quantum wire
NC	Nanocrystal
HOMO	Highest unoccupied molecular orbital
LUMO	Lowest occupied molecular orbital
a_0	Bohr radius
SE	Schrodinger equation
EDS or EDX	Energy dispersive X-Ray spectroscopy
XRD	X-ray diffractometer
UV-VIS-NIR	Ultraviolet visible near infrared
FTIR	Fourier transform infrared spectroscopy
TEM	Transmission electron microscopy
HRTEM	High resolution transmission electron microscopy
SAD	Selected area electron diffraction
JCPDS	Joint Committee on Powder Diffraction Standards
FWHM	Full width at half maximum
pH	Potential of hydrogen
IR	Infrared
DW	Distilled water
MR	Molar ratio
ppt	Precipitates
K	Kelvin
°C	Celsius
D	Crystallite size
ϵ	Strain
W-H	Williamson-Hall
δ	Dislocation density
TOP	Trioctylphoshine
TOPM	Trioctylphoshine metal
MBE	Molecular beam epitaxy
MEG	Multiple electron hole pair generation
OA	Oleic acid

2 MPA	2- Mercaptoethanol
3 MPA	3- Mercaptopropionic acid
QDSSC	Quantum dots sensitized solar cells
H.D.	Hydrazinhydrate
IBM	International Business Machines
CB and VB	Conduction and valence band
V_o	Open circuit voltage
J_{sc}	Short circuit current density
TOPSe	Tri-n-octylphosphine selenide
TOPO	Trioctylphoshine oxide
CCD	Charge Coupled Device
RHEED	Reflection high-energy electron diffraction
AR	Analytical Reagent

Figure Number	Caption	Page no.
Figure 1.1	(a) Energy band gap alteration between bulk material, QDs and atom (b) Variations in the density of states of materials from bulk to QDs	5
Figure 1.2	Tunable emission of QDs by changing the size 1 nm to 3.5 nm. All the QDs are illuminated with the same radiation but, the emission is different for different size QD	6
Figure 1.3	Excitons formation (a) An electron and a hole pair formed upon single excitation. (b) Two electron-hole pair formed upon single excitation	9
Figure 1.4	Energy levels formation in bulk material (continuous) and QDs	11
Figure 1.5	Different types of excitons formed in different materials a) Molecular exciton b) free exciton c) Charge-transfer excitons on adjacent molecules d) Exciton formed on the Surface of material	12
Figure 2.1	QDs synthesize by sol-gel technique	35
Figure 2.2	(a) TOPX (X = S, Se, Te) solution; (b) TOPM (M = Cd) and TOPO solution mixed at an elevated temperature; (c) tiny aliquots of the solution chosen at varied time intervals throughout the synthesis method.	37
Figure 2.3	(a) Maxwell Boltzmann distribution curve for the monomer species involved in the reaction; (b) Change in total free energy.	39
Figure 2.4	Co-precipitation technique for preparations of QDs.	41
Figure 2.5	X-Ray diffractometer used for XRD analysis.	46
Figure 2.6	The arrangement of different components used in X-Ray diffractometer experiment.	46
Figure 2.7	Different basic components used in the transmission electron microscope.	49
Figure 2.8	Transmission electron microscope used for	50

List of figures

	morphology analysis.	
Figure 2.9	UV-VIS-NIR spectrophotometer used for the analysis of QDs.	51
Figure 2.10	Block diagram to show the operation of UV-VIS-NIR Spectrophotometer.	52
Figure 2.11	FTIR equipment used for the analysis of QDs.	53
Figure 2.12	Arrangements of different components used in FTIR.	53
Figure 2.13	Raman Spectroscopy with Photoluminescence Spectrophotometer photograph used for the analysis of QDs.	54
Figure 2.14	Different components used in Luminescence Spectrophotometer.	55
Figure 3.1	The schematic diagram of the synthesis process.	61
Figure 3.2	XRD patterns of different Ag ₂ Se nanoparticles.	62
Figure 3.3	WH plot of Ag ₂ Se samples.	64
Figure 3.4	EDX spectra of different Ag ₂ Se samples.	66
Figure 3.5	TEM images of Ag ₂ Se samples.	67
Figure 3.6	Histogram plots of Ag ₂ Se samples.	68
Figure 3.7	Absorption spectra of Ag ₂ Se material.	69
Figure 3.8	Tauc plot of Ag ₂ Se material.	70
Figure 4.1	XRD patterns of different Ag ₂ S nanocrystals.	77
Figure 4.2	TEM images of Ag ₂ S samples.	78
Figure 4.3	Histogram of Ag ₂ S samples with Gaussian fit.	79
Figure 4.4	(a) The high-resolution TEM image, and (b) inverse fast Fourier transform configuration of sample 3 Ag ₂ S QDs.	80
Figure 4.5	UV-VIS-NIR absorption spectra of various Ag ₂ S samples	81
Figure 4.6	Raman spectra of Ag ₂ S samples.	83
Figure 5.1	Synthesis of Ag ₂ Se _x S _{1-x} QDs (a) the creation of Ag capped by 3-MPA NCs and (b) the creation of Ag ₂ Se _x S _{1-x} QDs capped by 3-MPA.	90
Figure 5.2	(a) XRD configurations of Ag ₂ Se _x S _{1-x} NCs (b) XRD	91

	configurations of most intense peaks.	
Figure 5.3	Williamson–Hall plot of $\text{Ag}_2\text{Se}_x\text{S}_{1-x}$ nanocrystals.	92
Figure 5.4	EDX spectrum of $\text{Ag}_2\text{Se}_x\text{S}_{1-x}$ nanocrystals.	93
Figure 5.5	FTIR spectrum of different $\text{Ag}_2\text{Se}_x\text{S}_{1-x}$ samples.	94
Figure 5.6	TEM images of $\text{Ag}_2\text{Se}_x\text{S}_{1-x}$ materials and SAD pattern of S2 and S4.	95
Figure 5.7	Histogram of different $\text{Ag}_2\text{Se}_x\text{S}_{1-x}$ samples.	96
Figure 5.8	Variation of size (polynomial equation of order second has been used to fit data) and Bandgap with the composition of $\text{Ag}_2\text{Se}_x\text{S}_{1-x}$ NCs.	97
Figure 5.9	Absorption spectra of $\text{Ag}_2\text{Se}_x\text{S}_{1-x}$ samples.	98
Figure 5.10	Tauc plot of $\text{Ag}_2\text{Se}_x\text{S}_{1-x}$ QDs.	99
Figure 5.11	Raman spectra of $\text{Ag}_2\text{Se}_x\text{S}_{1-x}$ nanocrystals.	101
Figure 6.1	(a) Operating principle of QDSSC. (b) Role of quantum confinement on the charge transfer from quantum dots to the TiO_2 .	107

Table Number	Caption	Page no.
Table 3.1	Different precursor ratios and other parameters used for the synthesis of Ag ₂ Se samples	61
Table 3.2	The various parameters calculated from XRD spectra of Ag ₂ Se samples	63
Table 3.3	Crystallite size and strain calculated by WH plot method	64
Table 3.4	The various parameters calculated by TEM images and UV-VIS-NIR spectroscopy for Ag ₂ Se samples	70
Table 4.1	Various parameters have been calculated from TEM and UV-VIS-NIR spectroscopy	80
Table 5.1	Various parameters calculated by the WH PLOT and TEM images of Ag ₂ Se _x S _{1-x} samples	92
Table 5.2	Atomic percentage for different elements in Ag ₂ Se _x S _{1-x} samples.	93
Table 5.3	The different parameters calculated from TEM images, UV-VIS-NIR and Raman spectroscopy of Ag ₂ Se _x S _{1-x} samples	96

Journals

1. "**Subhash Chand**, Ekta Sharma, and Pankaj Sharma. *Phase change induced quantization in NIR emitting Ag₂S nanocrystals: Structural and optical response for solar energy applications*. **Journal of Alloys and Compounds** 770 (2019) 1173-1180 (**WoS, Scopus indexed, I.F. = 4.175**)".
2. "**Subhash Chand**, and Pankaj Sharma. *Synthesis and characterization of Ag-chalcogenide nanoparticles for possible applications in photovoltaics*. **Materials Science-Poland** 36(3) (2018) 375-380 (**WoS, Scopus indexed, I.F. = 0.918**)".
3. "**Subhash Chand**, N. Thakur, S. C. Katyal, P. B. Barman, V. Sharma, and Pankaj Sharma, *Recent developments on the synthesis, structural and optical properties of chalcogenide quantum dots*, **Solar Energy Materials and Solar Cells**, 168 (2017) 183–200 (**WoS, Scopus indexed, I.F. = 6.019**)".
4. "**Subhash Chand**, Dhruv Sharma, Vineet Sharma, and Pankaj Sharma *Morphological and optical study of Ag₂Se quantum dots*, **AIP Conf. Proc.** 2009 (2018) 020026 (1-4) (**Scopus indexed**)".
5. "**Subhash Chand**, A. Dahshan, N. Thakur, V. Sharma, Pankaj Sharma, *Alloyed Ag₂Se_xS_{1-x} quantum dots with red to NIR shift: the band gap tuning with dopant content for energy harvesting applications*, (2019) (**Communicated to SCI, Scopus Indexed Journal**)".

Conferences/Workshops attended

1. "**Subhash Chand**, and Pankaj Sharma, *Synthesis, Structural and Optical analysis of Silver Selenide Nanoparticles*, 3rd National conference on Multifunctional Advanced Materials at Shoolini University Solan, 11-13 May 2016".
2. "**Subhash Chand**, D. Sharma, V. Sharma, Pankaj Sharma *Morphological and Optical Study of Ag₂Se Quantum Dots*, National Conference on Advanced Materials and Nanotechnology (AMN-2018) Jaypee Institute of Information Technology, Noida, 15-17 March 2018".
3. **Subhash Chand**, Participated in workshop on "Technical manuscript preparation with latex" at JUIT, Wagnaghat, 29 November 2015.

CHAPTER- 1 *

Introduction

* “**S. Chand**, N. Thakur, S. C. Katyal, P. B. Barman, V. Sharma, and P. Sharma, Recent developments on the synthesis, structural and optical properties of chalcogenide quantum dots, *Sol. Energy Mater. Sol. Cells*, vol. 168, no. August 2016, pp. 183–200, 2017.”

Materials play an important role in our daily life. Materials are used in our daily life in different forms and conditions like in transportation, houses, communication and food products *etc.* Man has tried to synthesize different materials from ancient times to fill their needs. In fact, early civilization has been known by their materials developments like stone age, bronze age, and iron age. Man has always tried to discover new materials which are superior in their properties than the available materials. It has been discovered that the properties of materials can be altered using heat treatments, the addition of other substances *etc.* Materials have been generally divided into metallic, ceramic and polymers forms. The properties of matter depend on the type of atoms and how these are bonded to each other. The atomic structure primarily affects the chemical, physical, optical and electrical properties. Microstructure and macrostructure largely affect the mechanical properties of the materials. The properties of any solid material depend on its chemical composition, atomic structure, and the size of the material.

1.1 Nanotechnology

Nanotechnology has made up of two words nano and technology. The scientific meaning of nano means a scale corresponding to 10^{-9} m. Nanotechnology deals with the matters having the size equal to or in between 1 to 100 nm. Nanotechnology in the traditional sense has been known as building things from bottom up. The word building things from bottom up has first coined up by the renowned physicist Richard Feynman. In 1959 Richard Feynman has discussed the strange and complex phenomenon of the materials by manipulating and controlling the size of materials.

The word “Nanotechnology” was first used in 1974 by the Japanese scientist Norio of Tokyo University of Science in a conference on paper production technology. In this paper, the ion beam milling and deposition of thin film to limit things over nanometre were discussed. He defined nanotechnology as, "Nano-technology mainly consists of the processing of, separation, consolidation, and deformation of materials by one atom or one molecule." During the 1980s, the thought of nanotechnology *i.e.* dealing with specific molecules and atoms was revealed as molecular nanotechnology. The credit of the development of molecular nanotechnology goes to K. Eric Drexler. He has explored the different ideas of nano-scale work for devices

through speeches and books. He described that Molecular nanotechnology can help to do nanosystems machinery manufacturing.

In the early 1980s, two main developments have encouraged the advancement in nanoscience. These developments include the discovery of the scanning tunnelling microscope (STM) and cluster science [1]. In 1985, these techniques lead to the breakthrough in the structural distribution of carbon nanotubes and fullerenes.

Gerd Binnig and Heinrich Rohrer developed the STM at International Business Machines (IBM) Zurich Research Laboratory [2]. This instrument has been utilized for imaging material surfaces at the atomic level. In 1986, Calvin Quate and Christoph Gerber have designed the atomic force microscope. Later on, in 1989, Don Eigler has manipulated the atoms by using STM. With the passage of time different studies on semiconductor nanocrystals has resulted in the development of quantum dots (QDs). These have possessed properties in between bulk semiconductors and the discrete molecules.

1.2 Quantum Dots

With the new innovation in the modern multidisciplinary research fields, semiconductor quantum dots have attracted researchers related to different fields like physics, engineering, material science, chemistry, and biology. Russian physicist Alexei Ekimov has discovered QDs in glass matrix of solids during working at the State Optical Institute (Vavilov) in 1980 [3]. Louis E. Brus (American chemist) had discovered the same QDs in colloidal solutions while working at Bell Laboratories in 1982 [4]. Louis E. Brus had found in his research that as the nanocrystals increase in size with time, the wavelength emitted/absorbed by nanocrystals changes. These results cause to conclude that this behaviour of QDs may be due to the particle confinement and leads to the quantum properties inside the materials occur with the passage of time.

QDs has shown distinctive behaviour in between atoms/molecules and bulk materials as given in figure 1.1 (a). The QDs roughly comprises 100 to 1000 atoms having a size in between 2 to 10 nm. QDs exhibit unique quantum properties when confined by the potential barriers to a small region having a “size less than the de-Broglie wavelength of charge carriers” [5]. The density of states of charge carrier’s

behaviour has shown parabolic, stepwise, spikes and discrete states (figure 1.1 (b)). These states of the material are corresponding to bulk, quantum well, quantum wire (QW) and a quantum dot. In nanomaterials, when the size of one dimension out of three dimensions of nanomaterial is reduced to the small nano-range while others remain above nano-range then the structure formed is known as quantum well. This leads to the confinement in one dimension of the material i.e. quantum laws applicable.

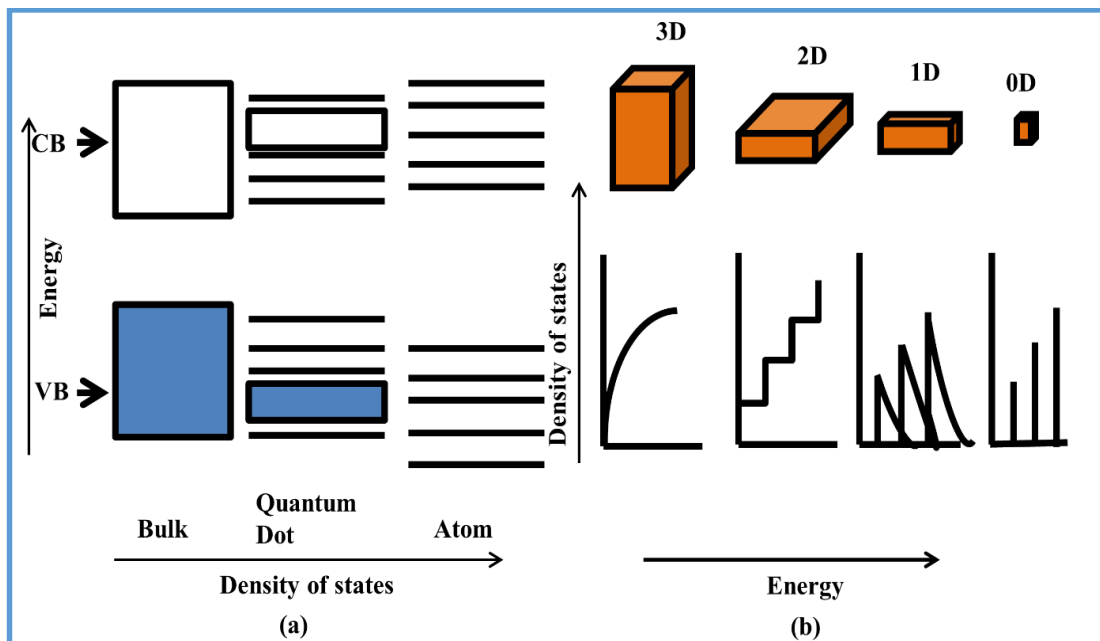


Figure 1.1 (a) Energy band gap alteration between bulk material, QDs and atom; (b) Variations in the density of states of materials from bulk to QDs.

1.2.1 Quantum Confinement Effects

Quantum confinement in semiconductor nanocrystal (NC) can be observed through experimentally as well as theoretically. Quantum confinement is used to calculate the bandgap of nanocrystal directly. Atoms have degenerate, discrete energy levels at which electrons can be located. When atoms come close to each other starts interacting with each other. In this process, the energy levels of valence electrons are modified and give rise to the lowest unoccupied molecular orbital (LUMO) and the highest occupied molecular orbital (HOMO) states. The energy gap between LUMO and HOMO is known as bandgap of the molecule. In the case of a bulk material number of atoms are increases and the interaction between the valence electrons of each atom

modified the energy levels of individual atoms. The interaction of atoms leads to the splitting of states into numerous energy levels. These numerous energy levels are considered continuous because the spacing between adjacent energy levels is very small. The inter atoms distance is changed with the decreases in the size of material below a certain limit. This change in inter atoms distance affects the bandgap of the material. These forms conduction and valence bands (CB and VB) depend upon the internuclear distance. This behaviour can be explained on the basis of a particle in a box for conduction and valence band.

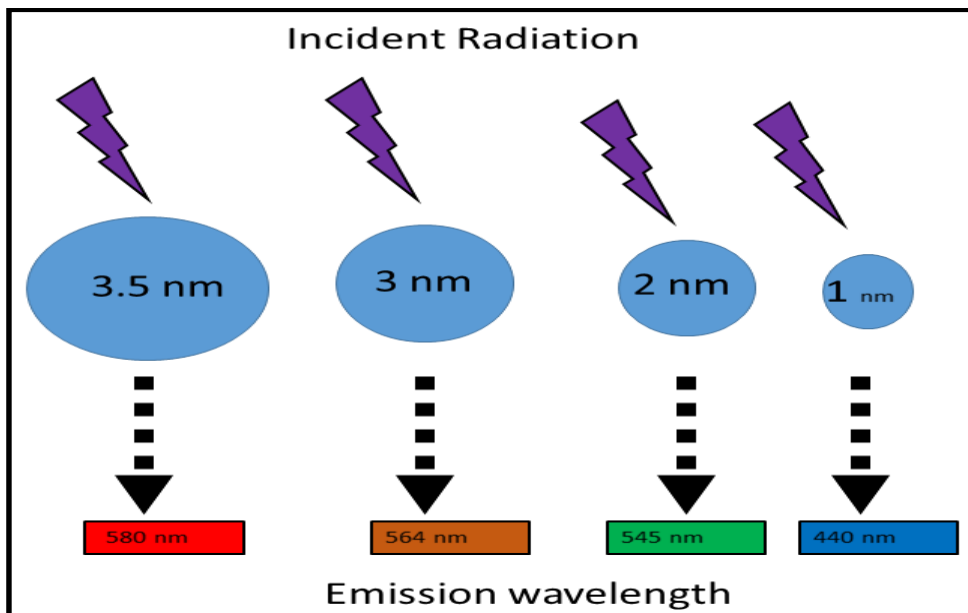


Figure 1.2: Tunable emission of QDs by changing the size 1 nm to 3.5 nm. All the QDs are illuminated with the same radiation but, the emission is different for different size QD.

In quantum confinement, there is a shift of the band gap edge toward the blue wavelengths i.e. towards lower wavelength. So, as the size of QDs decreases, there is an increase in the bandgap observed. This is a material dependent phenomenon and known as tuneable bandgap material. The tuneable band gap in QDs has a concept of the apprehension which originates by the quantum confinement (Figure1.2). The confinement occurs in the QDs having a size smaller than the thrice or twice the Bohr exciton radius (a_0). The properties of quantum wire and QDs are changed with the

variation in the chemical composition, size, phases, dimension of the layers and bandgap energies. More is the decrease in the size of material more is confinement in QDs. Generally, the effect of quantum confinement is significant when the charges restricted in a box of dimensions less than or equal to 10 nm. The quantum well width, depth, and height decide the overall discrete states in QDs.

This confinement concept can be understood by unravelling the problem of a particle in a box. Materials properties remain constant when the particle is free to move in any dimension (no boundary conditions apply). But, as one of the dimension comes under localization means there is some kind of potential applies to the material in one dimension. This leads to the restriction on the free movement of the particle in one dimension. To explore the properties of a particle in a quantum well type structure, take a particle in a rectangular box having length L_a , L_b , and L_c . Let us consider that localized dimension is L_c . Then, from the Schrodinger equation (SE) the energy for this particle is [6].

$$E = \frac{\hbar^2 (k_a^2 + k_b^2)}{2m} + \frac{\hbar^2 \pi^2}{2m} \left(\frac{n_c^2}{L_c^2} \right) \quad (1.1)$$

The discrete energy levels occur in L_c direction while the density of states remains continuous in the remaining two directions. Quantum wire (QW) has possessed two dimensions in the localized portion and the remaining third dimension in a non-localized portion of the material. Here, the localized dimensions are L_b and L_c . Then, from the SE the energy of the particle is [6];

$$E = \frac{\hbar^2 k_a^2}{2m} + \frac{\hbar^2 \pi^2}{2m} \left(\frac{n_y^2}{L_b^2} + \frac{n_z^2}{L_c^2} \right) \quad (1.2)$$

QD exists in three confinement dimensions and no non-localized dimension. The localized dimensions are L_a , L_b , and L_c in directions a, b and c respectively. The particle has no free momentum in any direction *i.e.* particle momentum has been localized in all the three directions. Then, from the SE the energy for this particle is given by [7]:

$$E = \frac{\hbar^2 \pi^2}{2m} \left(\frac{n_a^2}{L_a^2} + \frac{n_b^2}{L_b^2} + \frac{n_c^2}{L_c^2} \right) \quad (1.3)$$

Here, the discrete energy levels occur in L_a , L_b , and L_c in directions a, b and c respectively. For a spherical nanocrystal of radius r , the details of obtaining the energy levels are a bit more difficult than for a rectangular nanocrystal, although the resulting expression for the energy levels is very similar [8],

$$E_n = \frac{\hbar^2 \pi^2 n^2}{2m^* r^2} \quad (1.4)$$

where m^* denotes the effective mass of the particle (electron or hole) and the value of n depends upon the Bessel function, which further is determined using the values of principal quantum numbers and azimuthal quantum number.

1.2.1.1 The Exciton

The effect of size variation on the band gap in a QD is determined using the confinement regime in which QD exists. When a photon incident on a semiconductor, the electron jumps from the energy level of the valence band to the energy level of conduction band leaving a hole behind in the valence band. The bound position of an electron and a hole is known as an exciton. In an exciton electron and hole are bound to each other through Coulomb attraction (Figure 1.3 (a)). This state as a unit is free to move through a semiconductor. The bound state of electron and hole having less energy than the unbound state of electron and hole. In general, the dimension of material lies in between 1- 10 nm but may vary material to material. Exciton is electrically neutral because the electron and the hole (vacant space) have equal and opposite electrical charges. This can transport energy from one point to another point inside the material. In an exciton, the recombination of the electron and hole ends up with the primal position of the material. The exciton may lose its energy to emit radiation or give its energy to excite the other electron-hole pair inside the material. This leads to the formation of another exciton inside the materials. In this process, more than one exciton is formed inside the material [9] (Figure 1.3 (b)). The bound state space between electron and hole is known as the effective a_0 .

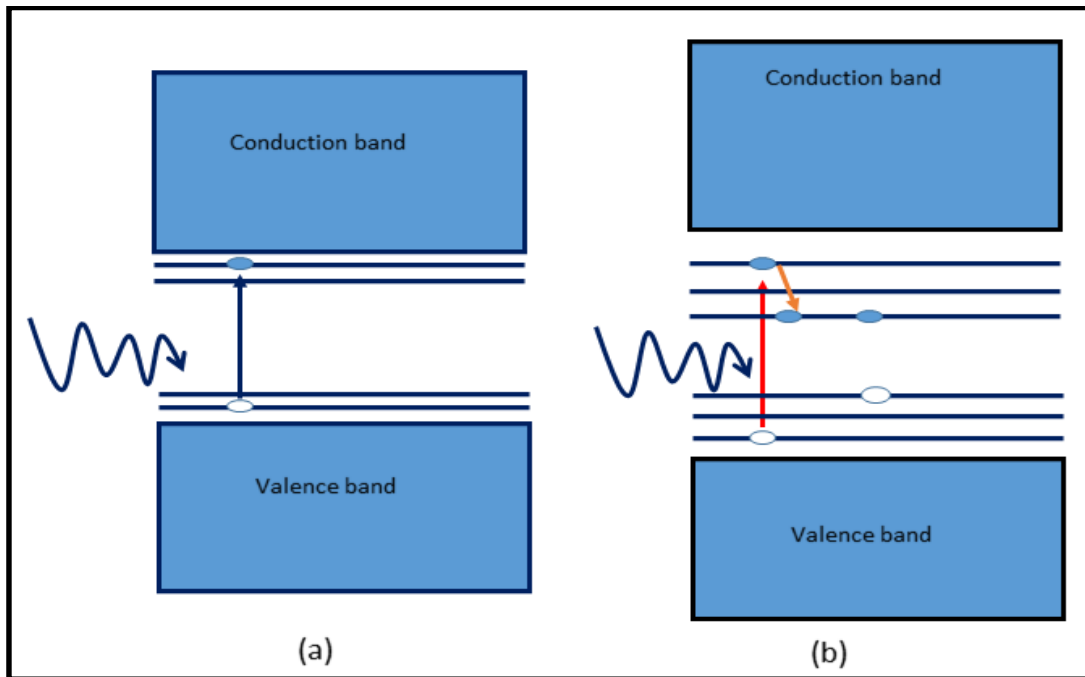


Figure 1.3: Excitons formation (a) An electron and a hole pair formed upon single excitation. (b) Two electron-hole pair formed upon single excitation.

The exciton Bohr radius (a_0) for a specific material can be calculated by equation 1.5. In the weak confinement region, the size (radius) of QD is less than $2a_0$ or $3a_0$. In this regime, quantum effects feebly influence the properties of the material. In the strong confinement region, the size (radius) of QD is less than a_0 . In this regime, quantum effects strongly modify the properties of the material (optical, electronic, etc.) by increasing the discreteness of energy levels below the conduction band and above the conduction band [5]. Exciton Bohr's radius can be expressed as:

$$a_0 = \frac{4\pi \hbar^2 \epsilon}{m_g^* e^2} \quad (1.5)$$

where \hbar and ϵ are the Planck's constant and dielectric constant of the material.

$$\frac{1}{m_g^*} = \frac{m_e^* + m_h^*}{m_e^* m_h^*} \quad (1.6)$$

where m_e^* (m_h^*) is the effective mass of the electron (hole).

The electron and hole in exciton interact with each other like a hydrogen atom. By solving the hydrogen atom problem, the energy can be written as [10];

$$E = E_r + E_R \text{ and } E_R = \frac{\hbar^2 \vec{k}^2}{2M}, E_r = -\frac{R_y}{n^2} = E_x \quad (1.7)$$

where E_r , E_R and R_y represent the energy for the hydrogen atom with central potential, kinetic energy for the centre of the mass system and Rydberg energy respectively. M is the sum of the effective mass of electron and hole. Exciton energy for bulk specimen can be written as [11], [12]:

$$E_x(n, k) = E_g + \frac{\hbar^2 \vec{k}^2}{2M} - \frac{R_y^*}{n^2} \quad (1.8)$$

where E_x is the exciton energy, E_g is the bandgap energy. With the change in the n and k values the exciton energy changes respectively. Exciton energy in the quantum well can be written as:

$$E_{ex} = E_g + E_{nez} + E_{nhz} + E_{nm}^r + E^R \quad (1.9)$$

where E_{nhz} , E_{nez} , E_{nm}^r , and E^R represent the hole confinement energy in the valence band and electron confinement energy in the conduction band, kinetic energy for the centre of the mass system and energy owing to potential respectively. A similar method is used to calculate exciton energy for the quantum wire and QDs. In QDs exciton energy levels in a spherical potential well can be categorized into weak confinement and strong confinement region. In strong confinement region, the electron and hole interaction term are very small as compared to other terms so can be neglected. The confinement regime energy levels of QDs are extremely quantized and behave like artificial atoms. The contribution of the Coulomb term is very small and can be neglected. Then the bandgap of the nanocrystal can be written as [13]:

$$E_n = E_g + \frac{\hbar^2 n^2}{2m_e^* R} + \frac{\hbar^2 n^2}{2m_h^* R} \quad (1.10)$$

The energy levels for the electron and hole in valence and conduction band can be calculated using equation 1.3. The Bessel function values depend upon principle (n) and azimuthal quantum (l) numbers. Figure 1.4 represents the different energy levels for electron and holes. QD has no restrictions on the l and n quantum numbers as possessed by the hydrogen atom as $l < n - 1$. The deepest energy level $n = 1$ and $l = 0$ has the structure of $1s$ orbital. The $2l$ nd level is termed as $1P$ level corresponding to value n

= 1, $l = 1$. Similarly, the IIIrd energy level is termed as 1D corresponding to value $n = 1, l = 2$ and IVth energy level as 2S corresponding value $n = 2, l = 0$ and so on.

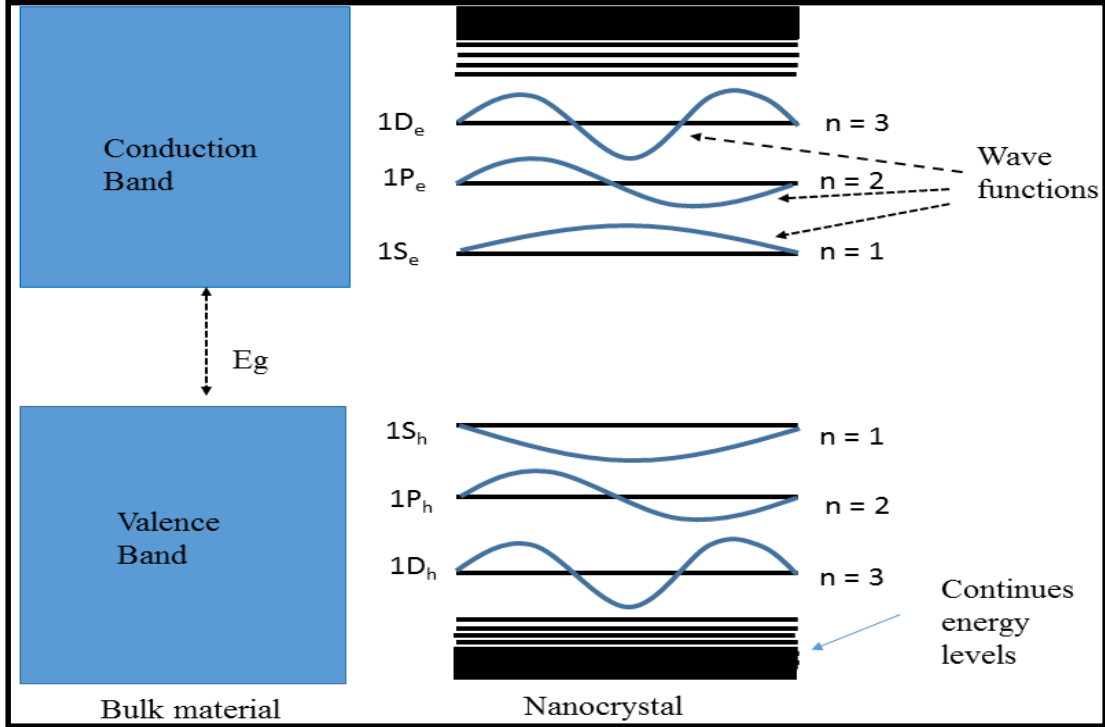


Figure 1.4: Energy levels formation in bulk material (continuous) and QDs.

If the dimension of the QDs is in the weak confinement region, then the Coulomb energy of exciton interaction cannot be neglected. In this type of confinement, potential turn out to be larger than the Coulomb forces. In the weak confinement regime, quantum dots contain a large number of atoms but are less than its bulk material. Bragg reflection from a large number of atoms at the periodic lattice results in the formation of continuous energy bands. Few numbers of levels below the conduction band and above the valence band shows discrete behaviour due to the delocalization electrons wave. In the above limit, the behaviour of exciton as a quasiparticle is well conserved. Different energy levels in bulk and in QDs are shown in figure 1.4. In a weak regime, the Coulomb term energy has shown a dominant contribution. The bandgap for the nanocrystal can be written as [14]:

$$E_n = E_g + \frac{\hbar^2 \pi^2}{2R^2} \left(\frac{1}{m_e^*} + \frac{1}{m_h^*} \right) - J_{e-h} + E_p^{pol} + E_h^{pol} - 0.248 E_{Ry}^* \quad (1.11)$$

where the IInd term on the right side of equation (1.11) denotes the discrete exciton energy, IIIrd term is equal to $1.786e^2/\epsilon R$ and denotes the effective Coulomb interaction between electrons and holes, IVth term E_e^{pol} denotes the self-polarization energies of the electron and Vth terms denotes E_h^{pol} the self-polarization energies of the hole, VIth term is depending on e^2/r . The term E_{Ry}^* represents the exciton Rydberg energy of electron and hole pair. The difference in energy between two energy states in the weak confinement region is less than 100 meV. The difference in energy between two energy states in the strong confinement region is more than the weak confinement region. Excitons are divided into the following types:

1.2.1.2 Frenkel excitons

Frenkel exciton size is approximately equal to the same order as the dimension of the unit cell of a material. This type of exciton has strong Coulomb interaction and small dielectric constant leads to small valued exciton. This is also known as molecular exciton because it is located on the same molecule (Figure 1.5 (a)).

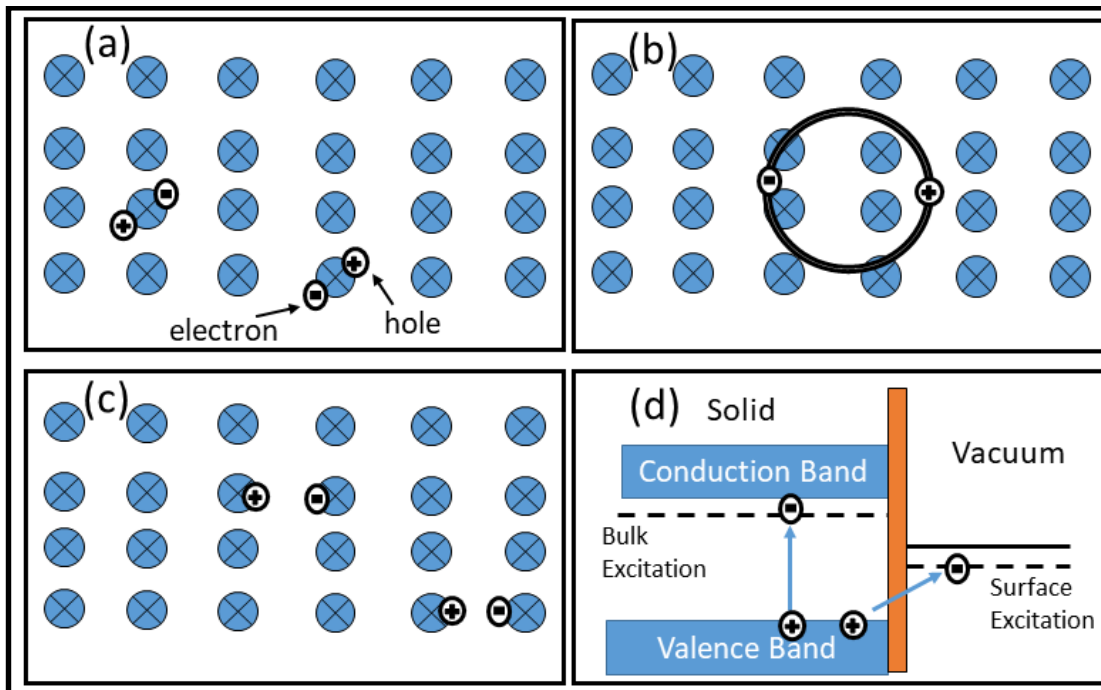


Figure 1.5: Different types of excitons formed in different materials (a) Molecular exciton; (b) free exciton; (c) Charge-transfer excitons on adjacent molecules (d) Exciton formed on the surface of material.

This exciton was discovered by Yakov Frenkel. The binding energy of Frenkel exciton approximately lies between 0.1 to 1 eV. Aromatic molecules like anthracene and tetracene composed of organic molecular crystals and alkali halide crystals are the examples of Frenkel excitons.

1.2.1.3 Wannier–Mott excitons

Excitons formed inside the semiconductor material are known as Wannier–Mott excitons (Figure 1.5 (b)). These excitons have a large radius as compared to Frenkel exciton. These excitons can move freely inside the material. So, sometimes this quasi-particle is also called as a free exciton. Free movement occurs due to the delocalization of exciton wave functions over many lattice constants. The separation between electron and hole are large as compared to the Frenkel exciton. Wannier–Mott excitons transfer the excitation energy from one point of the material to another point of material without transfer of charge.

1.2.1.4 Charge-transfer excitons

An exciton in which electron and hole occupy positions on adjacent molecules are called Charge-transfer excitons (Figure 1.5 (c)). The properties of Charge-transfer excitons are existing in between Frenkel exciton and Wannier–Mott exciton. These are formed generally in ionic crystal materials and possess a static electric dipole moment.

1.2.1.5 Surface excitons

An exciton in which electron is in the vacuum and the hole is inside the solid is known as surface excitons (Figure 1.5 (d)). This is possible due to the formation of image *states* on surfaces of materials. These type of excitons can only move along the surfaces of the material.

1.2.2 Effective Mass Approximation for defining quantum confinement effect

Brus equation is widely known as an effective mass approximation (EMA). EMA is a theoretical model to explain quantum confinement. The EMA approximation is mostly used in slowly varying perturbations to explain the electronic motion. The effective mass of electron or hole is the mass when it interacts with other identical particles in a thermal distribution. The movement of electron/hole in materials over the longer distance than lattice unit may result in different interactions. So, to include these

interactions in band structures the term effective mass is used instead of free mass. The effective mass for a material can be considered as a simple constant.

In the EMA model, electrons and holes are considered as free and non-relativistic spinless particles. Spherical polar coordinates of these particles can be written as r, θ, ϕ . The EMA approximation is based on the parabolic curve of energy (E) and wave vector (K). The energy levels and wave functions can be calculated by the solution of the Schrodinger equation. The EMA for charge carriers can be written as after solving the SE with appropriate Hamiltonian;

$$\left[-\frac{\hbar^2 \nabla_e^2}{2m_e^*} - \frac{\hbar^2 \nabla_h^2}{2m_h^*} - \frac{e^2}{4\pi\epsilon_0\epsilon(r_{eh})} + V_0 \right] \psi(r_e, r_h) = E\psi(r_e, r_h) \quad (1.12)$$

where r and m represent the position vector and mass, $r_{eh} = |r_e - r_h|$, ϵ_0 is the permittivity in the vacuum and ϵ is the relative dielectric constant of the specimen. Assuming $V = \infty$ outside the QDs and $V = 0$ inside the QDs. Efros and Brus [15] solve the equation (1.12) and proposed the energy values for the band gap of a QD having radius R .

$$E_n = E_g + \frac{\hbar^2}{2} \left(\frac{1}{m_e^*} + \frac{1}{m_h^*} \right) \frac{\pi^2}{R^2} - 1.786 \frac{e^2}{\epsilon R} \quad (1.13)$$

where E_g is the bandgap of the bulk semiconductor material. In this model Ist term denotes bulk semiconductor bandgap, IInd term describes the confinement energy of electron & hole and the IIIrd term explains the Coulomb interaction between electron and hole. The EMA has been used to calculate the bandgap of different QDs. EMA gives good results for the calculation of the HOMO-LUMO gap for larger size nanocrystals.

The EMA for small quantum dots overshoots the size but giving a good understanding of the blue shift of the optical absorption edge in QDs. failure of the EMA in small size QDs may be due to the assumption of parabolic relation between E and K diagram. Brus [15], Kayanuma [16] and Momiji [17] have reported the screened attractive Coulomb interactions between electrons and holes following absorption of a phonon of appropriate energy. In case of small size nanocrystals, the lowest energy level of the exciton is now delocalized over the entire QDs. The Coulomb interaction is completely neglected and the electron and hole are taken as the free particle in a

quantum dots. Multi-band EMA theory provides an improvement to the EMA. The semiconductors in which only the conduction band is non-degenerate, the electron effective mass can be well defined by the single band theory. The top part of the valence band is often degenerate. So, hole properties can be explained by taking the contribution of different energy levels to the valence band edge. Norris and Bawendi have reported 10 excited states of absorption spectra in CdSe QDs [18], [19]. This approach includes the valence band degeneracy. This approach fails to couple the valence and conduction band degeneracy. Later on Wang et al [20], and Nosaka et al [21] have reported further modification in EMA.

1.2.3 Quantum dots stability factors

QDs synthesized by any approach should be stable, so that these can be used in multiple fields. Following are the significant facts related to the stability of QDs.

1.2.3.1 Size control

Size of QDs depends upon various factors. These include temperature, pH of the solution, the concentration of ligands, material composition, precursor materials, growth rate, etc. According to need size can be controlled by changing one or more factors. Mostly, these factors affect the size of QDs during the synthesis process.

1.2.3.2 Stabilization

QDs have an ultra small size. This small size increases the surface to volume ratio of the material. These surface states become extra reactive as the size reduced. These smaller nanocrystals have a large tendency to agglomerate to form bigger size crystallites. So, generally, the stabilization of QDs has been performed by reducing the dangling bonds on the surface of nanocrystals with the help of capping agents or ligands. Capping agent provides stabilization basically by two types: one is steric stabilization and other is electrostatic stabilization by the surrounding molecules.

1.2.3.2.1 Steric Stabilization

It is a process in which additives (surfactants) inhibits the coagulation of suspensions. These additives include certain hydrophilic and hydrophobic chains of surfactants. These additives cover the nanocrystals in such a way that long tails extend out into solution. The surfactant hydrophobic end connects to the nanocrystal surface and the hydrophilic end is dispersed into the solution. Hydrophilic ends are repelling each other. This leads to the stabilization of the nanocrystals in the solution even

the zeta potentials of the surfaces are reduced to near zero. This approach is effective in both aqueous and non-aqueous media. This approach is less sensitive to impurities and other some trace additives than electrostatic stabilization.

1.2.3.2.2 Electrostatic Stabilization

Electrostatic stabilization is used to stabilize the NCs in colloidal solution. The NCs inside the colloidal solution is surrounded by the electrical double layer. If the charge on the surface of NCs is negative than positively charged ions from the solution are closely attached to the surface of NCs and form the first layer of ions. The second layer of ions is also formed on the surface of NCs but, with less attraction and is called diffusion layer or hydrodynamic layer. The first layer and second layer formed outside the NCs surface are electrically neutral. The van der Waals forces between different NCs have a tendency to attract each other. These attraction forces are conquered by the repulsion between the surrounding diffusion layers of NCs. So, in this process, the electrical double layer provides the necessary stabilization of colloidal NCs. In this method, a change in the electrolyte concentration may destroy the electric double layer. This process may result in an increase in the size of nanocrystals by agglomeration [22].

1.2.3.3 Passivation of surface states

The surfaces of QDs have a high density of surface states (uncoordinated bonds) which leads to the formation of dangling bonds. Radiative/ Non-radiative recombination takes place at the surface of QDs through a very strong interaction of the electron/hole wave functions at surface states. In general, passivation means the creation of an outer coating of any material on the surface of NCs by the formation of a micro coating and that is created by a chemical reaction with the base material. In this technique, passivation is achieved through a light coat of a suitable material such as capping agents or to create a shell of a different material. Passivation requires some certain conditions. This is used to enhance the properties of the material and preserves the appearance of nanocrystals.

1.3 Properties of quantum dots

The QDs have shown unique absorption and emission of radiation depending upon the nature of materials. Radiative transition time reduces from nanoseconds to picoseconds in QDs [23], [24]. The emission colour purity of QDs has a dependence

upon the morphology, the size and the quantum yield [25], [26]. Wide size distribution, *i.e.* wide full width at half maximum (FWHM), occur when water is used as solvent whereas if organic solvents are used then narrow size distribution has been reported (monodisperse nature).

1.3.1 Optical properties

QDs have shown size dependent optoelectronic property. The surface to volume ratio has increased with a reduction in the dimension of QDs. For two sized QDs derived from the same material, one having a larger surface area to volume ratio has exhibited less absorption and scattering losses. So, the total optical gain for larger surface QDs should be higher in comparison to other NCs. The NCs have shown different wavelength absorption/emission depends upon the size, composition and surface states (dangling bonds). The ultraviolet-visible-near infrared (UV-VIS-NIR) and photoluminescence (PL) spectrophotometer have been used to analyze the optical behaviour of NCs. In UV-VIS-NIR spectrophotometer, the continuous desired electromagnetic radiations are allowed to interact with QDs. In this process, the electrons get desirable energy and are excited to the higher levels which may include vibrational and rotational energy levels excitation and leads to the desired absorption of the incident radiations. Generally, the oxidation on the surface of nanocrystals results in the surface defects. These surface defects may result in undesired emission or sometimes destroy the exciton formed inside the NCs. In some cases, QDs having a higher degree of oxidation means a number of surface defects are there. The bandgap of such NCs between the HOMO and LUMO strongly depends on the presence of oxygen atoms. Sometimes the red shift in PL may be an indication of an increase in the degree of surface oxidation *i.e.* the bandgap is decreasing [27], [28]. Researchers have described that the dimension of QDs plays a significant role in the modification of band level energy in the QDs [29]. This has affected the frequency of fluorescent light emitted or absorbed by QDs. To increase the stability of QDs and intensity of emission core-shell structured QDs have been preferred. For example, a QDs of lead selenide have possessed a protective shell of lead sulfide.

1.3.2 Electrical properties

It has been reported that the smaller the size of QDs the greater the chance of the charge carriers to reach on the surface [30]. Electron or hole on the surface can transfer through thermionic emission or tunnelling to increase the conductivity.

1.3.3 Structural properties

The X-ray diffraction (XRD) pattern of QDs generally consists of broad or diffused peaks. The broadening in different peaks of XRD in QDs pattern is mainly due to the smaller size of the nanocrystals [31]. Other factors like instrumental setup, nanocrystal size, strain, *etc.* may contribute to the broadening of XRD peaks [31]. The contribution of broadening because the instrument is small so, it has to be removed from the total broadening. As the size of the NC increases the intensity of peaks increase and become sharper. Generally, the XRD configuration of NC and core-shell structure are different [32].

1.4 Literature survey

Chalcogenide materials consist of at least one element from S, Se, and Te. These materials may be binary, ternary, quaternary, *etc.* depending on the number of elements involved. Generally, chalcogenide materials are of two types one is crystalline and other is non-crystalline (amorphous). The crystalline materials possess a long range of regular arrangements of the atoms in three-dimensional spaces *i.e.* periodicity of atoms occurs. Amorphous samples have small range regularity of the order of atomic length scale because of chemical attachment between the atoms [33]. Polycrystalline materials (nanoparticles) category exists in between crystalline and amorphous materials. The range of nanoparticles (1 nm to 100 nm) can be divided into three parts: one is quantum well, second is quantum wire and third is QDs.

In most cases, QDs have shown an inverse relation between quantum confinement and dimension. The change in the dimension of NCs has affected the bandgap and optical characteristics of the sample. Long Yan *et al.* [34] synthesized NIR emitting different size PbSe QDs by hot injection approach. The dimension of QDs varies from 2.5 nm to 6.1 nm. The absorption and emission spectra of PbSe QDs have been observed by dispersing the QDs in tetrachloroethylene solution. The absorption peaks have been observed in between 845 nm and 1856 nm. The emission peak

wavelength has been observed between 946 nm and 1955 nm and has shown a Gaussian shape. Murphy *et al.* [35] presented the synthesis of PbTe QDs using one-pot synthesis approach. Oleic acid and 1-octadecene have been employed as a surfacing agent for PbTe QDs. The size has been calculated by transmission electron microscopy (TEM) ranging 3.3 nm, 5.8 nm, 6.4 and 8.3 nm and the first exciton peak of these QDs has been observed at 1194 nm, 1534 nm, 1614 nm, and 2054 nm respectively. For different sized PbTe QDs, the multiple electron hole pair generation (MEG) has been observed with the help of absorption spectra. Zhao *et al.* [36] investigated that the formation of bare lead sulphide QDs and lead sulphide /cadmium sulphide core/cell QDs. First, bare lead sulphide QDs have been synthesized by a wet chemical approach. Then PbS/CdS QDs have been synthesized by cation exchange on adding bare PbS QDs into CdO solution. The size of the core has been controlled by the shell thickness of CdS material. The size of bare PbS QDs has been calculated by TEM images as 4.9 nm, 5.2 nm, and 6.5 nm and the first exciton peak of bare PbS QDs has been reported at 1361 nm, 1414 nm, and 1620 nm respectively. The redshift in the absorption peak has been observed with the increase in the size of bare QDs. Zhang *et al.* [37] reported the formation of PbS QDs by way of Hines method. In this method, different sized PbS QDs have been synthesized by varying the capping agent (oleic acid) quantity and the temperature of the solution. These QDs have been utilized to fabricate photovoltaic cells. The power conversion efficiency has been found to be independent of the temperature of the solution but, V_O (open circuit voltage) and J_{sc} (short circuit current density) of the solar cell vary.

Aboulaich *et al.* [38] described the formation of CdS QDs through the one-pot hydrothermal approach. The reaction mixture has been heated in Teflon coated cylinders at 100 °C. The effect of capping agent, precursor solutions and pH have been observed on the size and optical properties of CdS QDs. The size has been calculated by Brus equation as 2.7 nm, 3.1 nm, and 3.5 nm with synthesis time 1 hour, 1.5 hours, and 2 hours respectively. The first exciton peak has been observed at 369 nm, 382 nm, and 387 nm for QDs synthesized at 1 h, 1.5 h, and 2 h. respectively. This red shift in absorption peak indicates that the bandgap of CdS QDs decreases *i.e.* Quantum confinement decreases. Comparatively better optical properties of CdS QDs have been observed at moderate pH value and at a slow growth rate. Shreedhar *et al* [39] reported

CdSe QDs sensitized strontium titanate (SrTiO_3) as a photoelectrochemical for water splitting. The SrTiO_3 powder has been synthesized via a hydrothermal approach. The CdSe QDs of different sizes have been synthesized by using tri-n-octylphosphine selenide (TOPSe) as selenium source and trioctylphosphine oxide (TOPO) as capping agent. The optical band gap has been calculated by first exciton peak corresponds to the green, yellow and red portion of the electromagnetic spectrum. Haram *et al.* [40] have reported the synthesis of different sized CdTe QDs by way of wet chemical synthesis route and results have also been confirmed theoretically using density functional theory. The size has been calculated by sizing curve changes from 2.4 nm to 4.7 nm which leads to the change in the HOMO and LUMO gap of CdTe QDs from 2.4 eV to 1.88 eV.

Hocaoglu *et al.* [41] have presented the synthesis of near IR emitting Ag_2S QDs by way of a wet chemical route. The initial precursors like silver nitrate, sodium sulfide, 2- mercaptopropionic acid and acetic acid have been used. The pH of the solution has been fixed to 7.5 by sodium hydroxide and acidic acid solution. The molar ratio of silver nitrate to 2- mercaptopropionic acid has been changed to get the desired size Ag_2S QDs. The emission peak wavelength of Ag_2S QDs has been tuned near IR region (786 nm - 851 nm). The of Ag_2S QDs has been used for cell imaging and have shown good potential in medical applications. Gu *et al.* [42] reported different sized Ag_2Se QDs having potential applications in bioimaging. The Ag_2Se QDs have been found to be monodisperse in nature and the size ranging from by 1.5 nm to 2.4 nm. The temperature of the solution has been fixed at 90 °C and observed a tuneable fluorescence. These QDs have been described to be water dispersible and hence, are easily operable for bioimaging without ligand changing process. Mir *et al.* [43] have narrated the preparation of silver sulphide QDs through the ion exchange of cadmium sulphide QDs with size changes 1.6 nm to 4.1 nm. The Ag_2S QDs have shown defect-related emission for a synthesis time of 10 minutes. The Ag_2S QDs have shown excitonic emission at 858 nm with a synthesis time of 20 minutes. The Ag_2S QDs have exhibited excitonic emission at 1088 nm with the synthesis time of 60 minutes. Langevin *et al.* [44] have prepared Ag_2Se QDs through the colloidal route and observed that QDs emit in near IR region of the electromagnetic spectrum. The Ag_2Se QDs has been found in the orthorhombic phase with size ranging from 1.9 nm to 9.4 nm. The absorption spectra

of Ag₂Se QDs has been observed by suspending QDs in chloroform solution. The absorption peaks have small intensity so, the baseline of absorption data fitted with polynomial and first exciton peak has been observed by Gaussian fit of the absorption data. Zhu *et al.* [45] have reported different sized Ag₂Se QDs for deep tissue penetration in vivo imaging. Ag₂Se QDs show tuneable emission in the second IR region (1000 nm -1400 nm). Initial precursors like silver acetate, 1- octadecene and TOPSe have been used in the hot-injection approach. 1-octadecene, oleylamine (OA) and tetradecylphosphonic acid (TDPA) have been used as capping agents. OA and TDPA capped QDs have not shown good quality as compared to 1- octadecene capped QDs. Bandgap has been calculated using the Tauc plot and found to vary from 1.5 eV to 1.1 eV. Chen *et al.* [46] have described the formation of bare silver telluride QDs and silver telluride /zinc sulphide core/shell QDs by way of the cation exchange approach. Ag₂Te QDs have shown tuneable emission in the second IR region from 1042 nm to 1120 nm. These QDs have been shown good colloidal, photostability and small hydrodynamic size. The change in the size of Ag₂Te/ZnS QDs has been observed with the change in the shell thickness ZnS. Jiang *et al.* [47] have synthesized Ag₂S QDs using a two-step wet chemical approach. The precursors, like hexamethyldisilathiane, myristic acid, 1- octadecene, silver acetate and octylamine, have been used to prepare different sized Ag₂S QDs. The size of Ag₂S QDs have been calculated by TEM images and show a narrow size distribution. Yarema *et al.* [48] have reported Ag₂X (X = Se, S and Te) QDs synthesized by way of silylamide promoted synthesis approach. The QDs of different size Ag₂X have been synthesized by changing the concentration of the TOPX (X = Se, S, and Te) solution and temperature of the solution. Sahu *et al.* [49] have described the synthesis of different size Ag₂Se QDs through the hot-injection approach. The size has been calculated by TEM images and it changes from 2.8 nm to 10.4 nm. The absorption wavelength has been altered from near IR to the mid-IR portion of the electromagnetic spectrum. The strong and weak confinement regimes of Ag₂Se QDs are shown by curve between reciprocal of the radius of QDs and lowest transition energy (absorption peak). Yang *et al.* [50] have described the synthesis of bright emitting in near IR-2 Ag₂S QDs. The water dispersible approach has been used to prepare Ag₂S QDs for in-vivo imaging applications. Different characterization techniques such as XRD, Fourier transform infrared spectroscopy (FTIR), TEM have

been used to explore the properties of Ag₂S QDs. These QDs have been shown good biocompatibility. Ji *et al.* [51] have depicted the synthesis of different sized Ag₂Se QDs by modified hot-injection approach. 1-octanethiol and 1-octadecene has been used as capping agents. The size of QDs has been observed to change from 4.2 nm to 3.2 nm by varying the synthesis temperature of the solution. The bandgap of the material has been increased from 0.8 eV to 1.2 eV with the reduction in size of QDs. The Ag₂Se QDs show emission from surface states as well as from the core of material by Gaussian fitting of PL spectra. Shi *et al.* [52] have described the synthesis of Ag₂Se QDs by taking 1-octanethiol, 1-octadecene and silver acetate as initial materials in a modified hot-injection approach. Different sized QDs have been acquired by varying the growth time. TEM images have been used to calculate the size and that changing from 1.9 nm to 3.1 nm. The absorption and emission peak of Ag₂S, Ag₂Se, and Ag₂Te QDs have been found to shift towards longer wavelength with the rise in the dimension of QDs.

1.5 Applications of silver chalcogenide QDs

In modern life, most of the devices depend upon the semiconductor industry. Semiconductor nanocrystals have shown their importance as an agent in multicolour imaging, multiplexed, biomedical research and detection [53], [54]. The formation of water-soluble QDs has resolved the problems of the short-life period, low quantum yield, and chemical sensitivity. These QDs linked with biocompatible molecules may be used for ultrasensitive and long-term fluorescence imaging of molecular spots in living cells of animal and human [55]–[57].

The thin films and powder sample of QDs consisting of chalcogenide materials may be used in electrical, chemical and optical fields of sciences. These materials show different applications in different areas like such as waveguides, photonic crystals, non-linear optics properties, photo and image sensors, thermoelectric energy generators, solar cells, selectors, phase change memory, displays related fields, optical memory, phosphors and channel material for different thin film transistors, liquid crystal displays *etc.* [58]–[62]. From the last decade, enormous efforts are going on to improve the properties of the materials using various routes like doping with suitable materials, defects, make active and passive devices and bandgap engineering [63]–[65].

These QDs may become a magnificent material as biocompatible carriers of comparable sizes and surface properties can be composed for clinical uses. Recent applications of QDs in drug delivery are classified into two fields; first QDs acts as carriers and second as labelling in medical therapy (drug carriers). Some remarkable processes that have been studied in semiconductor structures are like tunnelling effect, quantum Hall effect, multiple exciton generations etc [66]–[68].

NCs of semiconductors have shown great promises in a number of fields including transportation, health, biomedicine, computers, environmental uses, scientific materials, power, private maintenance products, and consumer goods [69]–[73]. To accomplish these above purposes QDs needs to be designed in such a way to achieve specific performance goals in different fields.

1.5.1 Solar cells applications

The sunlight in the near IR region comprises half of the solar radiation that falls on the earth. Most solar cells are incapable to harvest energy from IR radiations. QDs sensitized solar cells are devices that can be employed to harvest the IR radiations. Semiconductors NCs have the great promise to support new developments in solar cell engineering. The QDs sensitized solar cells have the ability to tune band gap which leads to the absorption of different radiations. QDs have the ability to increase the bandgap of the materials which results in an increase in the output voltage in solar cells and hence increases the efficiency significantly.

The working of solar cells primarily comprises absorption of radiation, charge separation (electron-hole pair) transportation and collection. QDs can be used in solar cells mainly in three ways: 1) The QD-sensitized solar cells like dye-sensitized solar cells [74], 2) Inorganic QDs used solar cells, 3) Organic-inorganic hybrid QDs used solar cells [75]. The main idea is to stack different sized QDs to utilize solar radiations over a wider range to increase efficiency significantly. Briefly, a combination of surface chemistry engineering and development of new device architectures contributes to recent progress. QDs possess high absorption coefficient as compared to organic dyes [76]. In a bulk semiconductor, radiation of energy ($h\nu$) more than or equal to bandgap (E_g) falls on the material dissipated its extra energy ($h\nu - E_g$) in the form of heat through the phonons vibrations. These phonons vibrations may be reduced by extracting the hot carriers before the return to the band edge. This process is known as phonon bottleneck.

In QDs, the relaxation time of hot carriers increases with the increase in the quantum confinement. This relaxation time of hot carriers in bulk semiconductor is in the range of picoseconds (ps) and in QDs is in the range of nanoseconds (ns) [77]–[82]. The creation of the large number of bound pairs of electron and hole with a radiation-induced on QDs has been termed as MEG capabilities [83]–[86], [87]. This formation of more than one electron-hole pair is due to the increased Coulomb forces between the electron-hole and conservation of momentum laws [88], [89]. This process is presented in figure 1.3 (b).

1.5.2 Quantum computation and quantum information processing

Quantum information processing theory has been imagined as an encouraging tool of current classical binary computation by using the unique properties of quantum mechanics [90]. In this theory, the classical bit (one or zero) is replaced by a quantum bit that could not only take the values one and zero but, take a linear combination of both (zero and one). Electron spins of QDs have been proposed as q-bits due to their remarkable coherence time ($\sim 200 \mu\text{s}$) [91]. In these, electric fields have been used to attain the quantum confinements. The information of an electron-hole pair recombines provided by spin selection rules. The polarization of the released photon conveys about the spin of the electron and hole. Different optical-selection rules decide the use of initial parameters in QDs [92]. The different discrete energy levels of spins in QDs are being utilized for quantum simulations.

1.5.3 Biological applications

QDs of semiconductors have attracted significant consideration in the scientific community over the past few years due to their applications in biological world which include: building blocks of novel biosensors, drug delivery, recognition of pathogens, tissue engineering, gene delivery, cancer detection, examining of DNA structure and influential fluorescent probes [93]. The new emerging QDs having enhanced biocompatibility promote their biological uses. QDs show promising use in the required biomolecules recognitions [94]. These mainly comprise of protein and nucleic acids recognition. These QDs has shown promising applications in the field of in vitro recognition and cellular targeting. Cancer diagnosis and other intuitive information can be accessed by the use of QDs [95], [96]. The QDs can be utilized in the form of

fluorescent biological labels. Conventionally, organic dyes have been used for such biological labels. IR emitting QDs are suitable materials for such type of applications.

1.5.4 Light emitting diodes

During the last two decades of research, different researchers are able to obtain the performance of QDs light emitting diodes (QLEDs) in the vicinity of the organic light emitting diodes (OLEDs) [97]–[99]. QDs has emerged as a contender of single-material for full-colour light sources [100]. In the last decade, significant attention has been paid on QLEDs to increase the efficiency with the use of distinct properties of QDs [101], [102]. Nanocrystals used in LEDs offer significant advantages over organic OLEDs. In OLEDs, organic fluorophores are used to emit radiation. This leads to poor photostability and short lifetimes relative to QLEDs. QLEDs are also cost-effective for the manufacturing of high-quality white light LEDs. The use of QDs in QLEDs has been reported by researchers in the form of thin films [103], [104]. The electron and hole are created in the QDs layer by the absorption of radiation. The electrons are moved through the electron carrying layer. Similarly, holes are moved through the hole carrying layer. These carriers move through the cathode and anode layers respectively to get desired QLED device operation [105]

1.5.5 Counterfeiting applications

The reputed brands and companies are facing the problem of counterfeiting of their products. Despite a number of efforts made to counter the counterfeiting problems but, still, it persists. The general anti-counterfeiting methods comprise marking the goods with dye, codes, ink or assigning particular trademarks which differentiate from fake items. Nanocrystals tagged materials would be extremely difficult to duplicate. This is possible due to the specific emission and excitation wavelength possessed by QDs.

1.5.6 Thermoelectric applications

In the thermoelectric devices, electrical current is converted into heat and vice versa. These devices made-up of nanocrystals can be used in silicon chip engineering for a specific purpose. The performance of various components of devices may be degraded due to the heat produced by the use of electrical current. Nanocrystals based thermoelectric silicon chips are ideal to cool the silicon chips electrically which reduced the damage to the device caused by heat.

1.5.7 Photonic devices

Photonic devices deal with the light (photon) generation, detection, and manipulation through emission, transmission, etc. To exhibit high performance and flexibility by photonic transport systems requires optical frequency resources with wide capacity. The QDs may act as photoactive materials for production and carrying of charge carriers. The probability of MEG in QDs per excitation has great importance for photo-driven applications. The main constituent of integrated optics is the optical waveguide. Optical waveguides are significant in photonic technology because of confined structure and transmit the light into an integrated optical device having reduced dimensions. The QDs properties like gain and propagation length of the light travelling along the structure are basic parameters used in an active waveguide material.

In general, QDs may act as quantum emitters, switches and non-linear optical media [106]. In photonic devices, the quantum emitters act as a basic block. The materials with emission or quantum states can be controlled optically and that is required for the quantum information processing in photonic devices. QDs is a suitable material to control the spin states of electron and holes through optical pulses. The electromagnetic waves are strongly localized in photonic devices. This strong localization increases the interaction between photons and QDs. The QD structures are projected for broadband optical gain materials [107].

1.5.8 Photocatalysts

The use of QDs as photocatalysts depends upon the bandgap and quantum confinement [108]. The QDs have been used as photocatalysts in a chemical reaction to separate hydrogen from water molecules [109]. The incident photon excites the electron from the ground state to excited state to form an electron and hole pair which initiates the redox reaction in the chemical reaction. The chemical energy stored in QDs depends upon the size of bandgap and that governs the excited electron energy. The main disadvantage of QDs as photocatalysts is the reactivity of capping agents present on the surface of QDs in the chemical reaction and this decrease the transfer rate of the electron.

1.6 Motivation of thesis work

Our energy consumption is broadly depending on fossil fuels. Fossil fuels have been considered as a main ecological hazard on account of their significant impact in producing greenhouse gases. The eco-friendly sources of energy are accomplished through the conversion of solar radiations to electrical energy by polymers, piezoelectric vibrations, QDs based solar cells, and inorganic dye. Among them, QDs have unique properties *i.e.* MEG, effective charge transfers to the conduction band upon irradiation of suitable wavelength, band gaps tuning due to quantum confinement effects. These factors may result in the effective harvesting of solar energy when employed in various sized QDs. Theoretically, the QDs sensitized solar cells (QDSSCs) can enhance the power transformation efficiency up to 66 percent but, experimentally its value is smaller. So, there is a possibility to increase the efficiency of QDSSCs up to its theoretical value by adjusting the various parameters during synthesis and device fabrication process. The tuneable properties of band edges of QDs may result in desired charge separation and photochemical stability. QDs have strong light harvesting efficiency in the UV, visible and NIR regions. The broad solar spectrum of visible and infrared ranges can be exploited by varying the dimension of the QDs. During the last few years, the use of QDs as radiation harvesters has encouraged a lot of attention on account of its greater extinction coefficient in comparison to conventional dyes for controlled light energy conversion [110]–[113]. Because of size quantization properties, optical and electronic possessions of the QDs can be modified to further tune the response of QDSCs [114]–[116].

Generally, most of the existing QDs have shown absorption and emission in UV and visible region. To synthesize durable light absorbers and to broaden the spectral response of the photo-sensitizers particularly in visible and NIR regions silver chalcogenide QDs have been proposed. Presently, most of the existing QDs (Cd and Pb based chalcogenides *etc.*) are radiated in the UV region and emitted in the visible region. These type of QDs are not suitable for our ecological system. Quenching effect has been observed in biological constituents, like haemoglobin and water by absorbing and scattering light in the visible region [117]–[119]. Living tissues also show autofluorescence in the visible spectrum region [120]. Penetration depth by light waves has restricted up to the visible region [121]. The NIR emitting QDs are encouraging

contender for biomedical imaging in alive tissues because it solves the problem of autofluorescence by reducing the fluorescence background and improve tissue penetration depth. The NIR emitting QDs have been synthesized by various researchers *e.g.* PbX (X= S, Se, and Te) but, these are toxic in nature. In the imaging window particularly for vivo bio-applications, toxicity is considered as the main hindrance in the practical use of QDs. So, comparatively more environmental friendly silver chalcogenide based QDs have been proposed and may show emission in the NIR region.

Most of the NIR radiating QDs have been prepared in non-aqueous method or ion exchange method. Therefore, it is of great importance to invent an effective route for the synthesis of water-soluble functionalized NIR emitting silver chalcogenide QDs for targeting tumour imaging in vivo applications. The different properties of QDs depend upon the various factors involved in the synthesis process. Wet chemical approaches have been preferred on account of their easiness. Different synthesis approaches under different situations result in changing the properties of QDs. The main factors which influence the properties of QDs during the synthesis process are initial precursors used, solvent, the temperature of the solution, pH of the solution, synthesis time, *etc.* [120], [122].

Researchers from different fields have reported the change in the size of QDs with the change in the pH of the solution. Similarly, change in temperature of solution and synthesis time also changes the size of QDs which alters the absorption and emission properties of QDs. The devices fabricated with these types of QDs need to be precisely tuned for obtaining the maximum conversion of specific wavelength's energy to current or voltage to achieve maximum radiation harvesting efficiency.

Surface-active agents also play a very important role to control the dimension of nanocrystals during the synthesis process [123]. Excessive use of capping agent may restrict the formation of nanocrystals whereas the smaller quantity of capping agent may not provide effective passivation required for the formation of QDs. So, the quantity of capping agent must be optimized to get desired size QDs. Low-temperature synthesis approach has been preferred since it is easy to handle.

Most researchers have reported that quantum confinement occurs in the material due to the reduction in the dimension of nanocrystals. The phase change of material

may change the properties of the material. So, the phase change may induce a quantization effect inside the material. Few researchers have been reported that with the change in the composition of material bandgap can also be tuned (quantum confinement). Composition-dependent QDs changes the properties (bandgap, extinction coefficient *etc.*) of sensitized devices without much altering the device size. Alloyed materials may show improved properties over their binary counterparts due to changes in structural, and optical properties of materials.

Considering the above points eco-friendly QDs of silver chalcogenides {Ag₂S, Ag₂Se, and Ag₂Se_xS_{1-x}(x = 0, 0.4, 0.6 and 1.0)} have been synthesized by wet chemical approach (co-precipitation approach, *etc.*) and the QDs have been characterized for their morphological, structural and optical properties by TEM, XRD, UV-VIS-NIR absorption spectroscopy, FTIR spectroscopy and Raman spectroscopy.

This thesis work has been carried out for three objectives:

- Optimization of conditions for the synthesis of Ag₂Se QDs
- Structural, morphological and optical properties of co-precipitated Ag₂S QDs
- Structural, morphological and optical properties of co-precipitated alloyed Ag₂Se_xS_{1-x} QDs

1.7 Outline of the thesis

The thesis has been divided into six chapters. Chapter 1, contains the broad introduction of nanotechnology, QDs, properties of QDs, a literature survey on different QDs and various applications of QDs. The quantum confinement, exciton, EMA and various stability factors have been discussed briefly in QDs section. The properties of QDs section has included the optical, electrical and structural properties. At the last of chapter 1, the motivation this thesis work has been discussed.

Chapter 2 comprises of different synthesis approaches and the characterization techniques. The synthesis methods have been distributed into the top to bottom and bottom to up techniques. Short information about the instrument and their working has also been discussed in the characterization section.

Chapter 3 depicts the synthesis and characterization of Ag₂Se nanoparticles. The condition (precursors, method *etc.*) for the synthesis of Ag₂Se QDs have been optimized in chapter 3.

Chapter 4 describes the synthesis and characterization of Ag₂S QDs. The phase change induced quantization has been depicted in this chapter. XRD, TEM, Raman spectroscopy, and UV-VIS-NIR absorption characterization techniques have been used for the structural, morphological and optical study of Ag₂S QDs respectively.

Chapter 5 includes the alloyed Ag₂Se_xS_{1-x} QDs. In this chapter, the synthesis and characterization of Ag₂Se_xS_{1-x} (x = 0, 0.4, 0.6 and 1.0) QDs has been described. XRD, FTIR, TEM, UV-VIS-NIR absorption, and Raman spectroscopy characterization techniques have been applied for the study of the structural, surface binding of nanocrystals, morphological and optical behaviour of alloyed QDs respectively.

Chapter 6 comprises the overall conclusion, discussion, and summary of the work reported in the thesis. The prospective opportunity of the work has been described in the last part of this chapter.

At the end of the thesis, the bibliography has been included.

The content of the first two chapters is related to all the results. Chapter 3, chapter 4 and chapter 5 have their individual introduction, experimental details, results, discussion and conclusion.

CHAPTER- 2 *

Experimental details

* “**S. Chand**, N. Thakur, S. C. Katyal, P. B. Barman, V. Sharma, and P. Sharma, Recent developments on the synthesis, structural and optical properties of chalcogenide quantum dots, *Sol. Energy Mater. Sol. Cells*, vol. 168, no. August 2016, pp. 183–200, 2017.”

This chapter includes different synthesis approaches of QDs and various experimental techniques employed to characterize them. Structural, morphological, and optical properties of synthesized QDs samples have been studied by “X-ray diffraction, Transmission Electron Microscopy, UV-Visible absorption spectroscopy, FTIR and Raman spectroscopy”.

There are numerous ways for the synthesis of QDs and that have been approached on the basis of their applications. Generally, the methods of synthesis include X-ray lithography, e-beam lithography, molecular beam epitaxy (MBE), ion implantation, sonochemistry, colloidal synthesis. For the majority of device fabrications, monodispersed QDs have been required owing to their properties *i.e.* narrow size distribution and non-agglomeration. During the synthesis, by using suitable surfactant (also called capping agents) the agglomeration of QDs can be prevented. Capping agents forms chemical bonds or adsorbed on the surface of the nanocrystal and hence provide the stability to QDs. Thiols are mostly used as capping agents in the course of the synthesis of NCs.

2.1 Synthesis of quantum dots

QDs have been synthesized by the various wet chemical methods like sol-gel, microemulsion, co-precipitation, sonochemical, cation exchange, facile approach *etc.* These wet chemical techniques have their own specific advantages and disadvantages. Different methods under different situations result in different sized QDs. Synthesis of QDs has been segregated into two types; first is top to the down method and second is down to up method. These two approaches are further subdivided and have been discussed below.

2.1.1 Top to down approach

In this approach, the desired nanocrystals have been synthesized by externally-controlling the initial macroscopic structures. Some of the examples are ball milling, etching through the mask, application of severe plastic deformation *etc.* [124]–[126]. In top to down approach, a bulk semiconductor has been thinned in a stepwise process. QDs of radius <15 nm have been obtained by electron beam lithography and reactive-ion etching [127], [128]. QDs of varied sizes and shapes have been synthesized with the required packing geometries. Various techniques such as laser beams and focused

ion have also been used to synthesize arrays of QDs [129]. A high resolution has been shown by focused-ion-beam approach and nanoparticles of size around 20 nm have been synthesized using it. A beam of gallium ions with a spot size of 5-6 nm has been accelerated in a high vacuum chamber. The accelerated beams strike on the material to be thinned and eject the atoms by relocating the surfaces on the material. Secondary electrons have been removed by accelerated beams and with required control formed the desired shapes of the material [130]. In the dual beam focussed ion beam approach, an extra electron gun has been possessed and this provides a good precision over the material reconstruction process. The top to down approach has also been including photolithography, printing, electron-beam lithography, and modelling and stamping [131]–[133]. The major drawback of this approach in the synthesis is the incorporation of impurities and crystal imperfections. [134].

2.1.2 Down to up approach

The down to up approach has additionally been remarked as the self-assembly method. This method includes the shrinking of chosen material constituents with self-assembly route and this leads to the creation of nanocrystals. In this approach, the physical forces engaging at the nanolevel are self-assembled to make primary constituents into larger stable assemblies. The typical examples of the synthesis of QDs are from epitaxial growth and from colloidal solution. The down to up approach has been divided into two methods *viz.* wet chemical and vapour phase.

2.1.2.1 Wet chemical methods

Wet chemical methods have also been referred to as colloidal chemistry approaches. This has been further divided into 5 approaches: 1) Sol-gel approach 2) Hot injection approach 3) Co-precipitation approach 4) Hydrothermal approach, and 5) Ion-exchange reactions approach. These approaches have been described briefly here.

2.1.2.1.1 Sol-gel approach

This approach has been employed to synthesize inorganic materials and ceramics [135]–[137]. This approach has been commonly applied for the handling of coatings, bulk oxides, and fibres. The SiO₂ synthesis from liquid Si metal–organic solutions is mainly explored sol-gel method. The sol-gel process has been divided into four steps: 1) The precursor solutions have been taken in a beaker and stirred to form solvated metal precursors known as a sol. 2) The gel formation takes place inside the

solution by hydrolysis and polycondensation process by the formation of a bridged network. These gels may be used directly to deposit on the substrate to form xerogels and further heating results in the formation of dense films. 3) The process of conversion of gel into a solid mass by continuous polycondensation reaction has been termed as ageing or syneresis. In this step, the Ostwald rippling and phase transformation of solution occur. 4) To remove the water from the gel networks drying of the solid mass solution has been performed. The drying process has been further divided into three steps: (a) the critical point (b) the constant rate period approximately 10-14 days, (c) the first falling rate and the second falling rate time periods. The isolated evaporation of solid mass solution has been resulted in the formation of xerogel. The supercritical drying of the solid mass solution has resulted in the formation of an *aerogel* [138], [139]. The different steps are implicated in sol-gel handling are shown in the schematic figure 2.1.

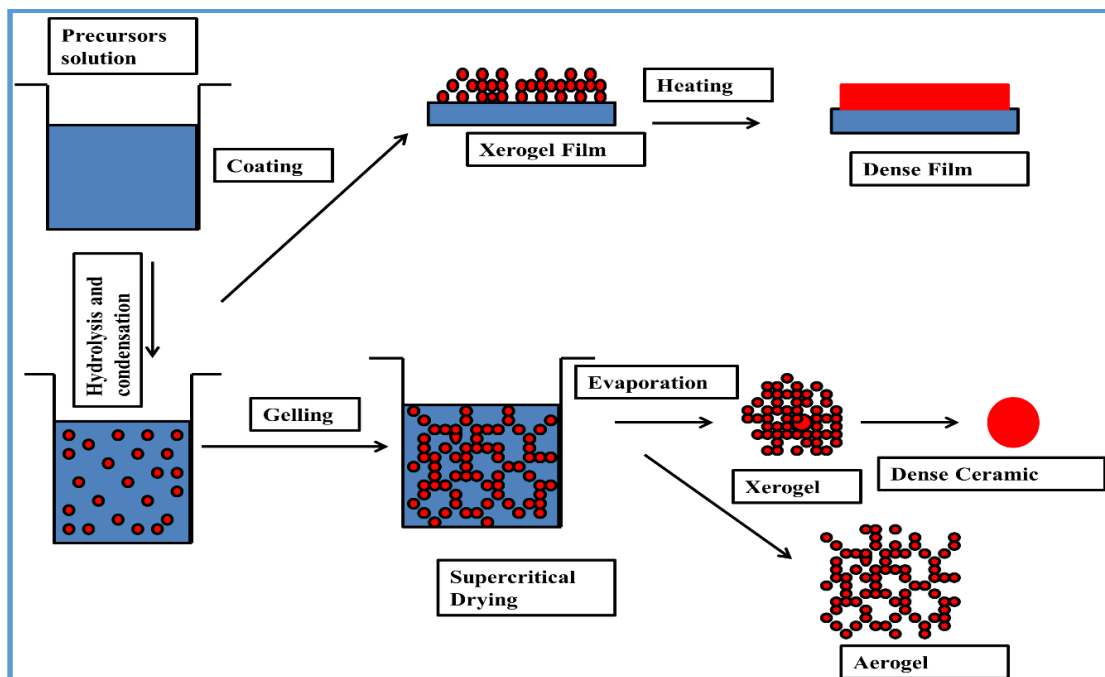


Figure 2.1: QDs synthesis by sol-gel technique.

Different processing parameters (the type of initial precursors, the concentration of ions formed inside the solution, temperature, *etc.*) affect the pore size, interconnectivity, and distribution of the QDs [140]. The porous gels arrange

themselves to form unique products [141]. Scientists in different fields have extended the sol-gel method to synthesize non-oxidic materials from the last decade. The first material of non-oxide aerogel has been prepared from pyrolysis of resorcinol-formaldehyde gel [142]. The gel formed in the sol-gel approach has been divided into three steps; thiolysis, condensation, and metathesis. Metal sulfide gels or precipitates have been formed by thiolysis of thiolates and metal alkyl solutions in the presence of hydrogen sulfide [143].

Thiolates molecules present on the surface of metal chalcogenide nanoparticles form a viscous sol inside the solution. The disulfide linkages form oligomers in the presence of oxidants. Further, the treatment of these oligomers leads to the formation of polymers or gels. Aerogels have been formed in solution when supercritical drying of gel takes place. The surfactants are generally Mercaptoundecanoic acid, 4-Florophenylthiol *etc.* Hydrogen peroxide (H_2O_2), tetranitromethane (TNM) and photo-oxidation are the oxidants have often been used in the oxidation process of surface thiols [144], [145]. In metathesis process, random aerogels have been formed inside the solution. The metal chalcogenide bonded materials act as a basic block for the construction of the random polymeric structures. Metal ions make bonds with the chalcogen ions in water and form a gel inside the solution [143].

Mohammad Reza Gaeni *et al.* [146] have developed CdSe quantum dots by sol-gel approach. The initial precursors like Se powder sodium borohydride, cadmium chloride, nitric acid, and sodium hydroxide have been used. The solution I of selenium powder in water has been prepared by stirring. Sodium borohydride has been added to the solution I with uninterrupted stirring until a clear solution is formed. The solution II has been formed by adding the desired amount of starch in cadmium chloride solution with continuous stirring. A small amount of nitric acid have been put in to get a clear solution. After this sodium hydroxide solution has been dropwise poured into the solution II until the pH reaches close to 12. Then, solution I has been poured into solution II with constant stirring. The color transformation of the mixed solution indicates the formation of cadmium selenide QDs. The gel of CdSe QDs has been formed by continuously stirred and aged solution. The advantages of sol-gel method contain high control of purity, low solution temperature, repeatable, ease, and

uniformity of the nanocrystals. This is a powerful method to maintain the size and shape of the nanostructures QDs.

2.1.2.1.2 Hot injection approach

This approach has been commonly employed to obtain monodisperse QDs in colloidal solution. The initial precursors used in this approach are, generally, TOP (trioctylphosphine), TOPO (trioctylphosphine oxide), X (Se, S, Te) powder and MO (metal oxide) or MCL (metal chloride). TOPO play as surfactant or capping agent role in the solution. This approach consists of three steps. The first step is to synthesize the TOPX solution by dissolving the appropriate amount of X powder in TOP solution. The second step is to synthesize the TOPM + TOPO solution.

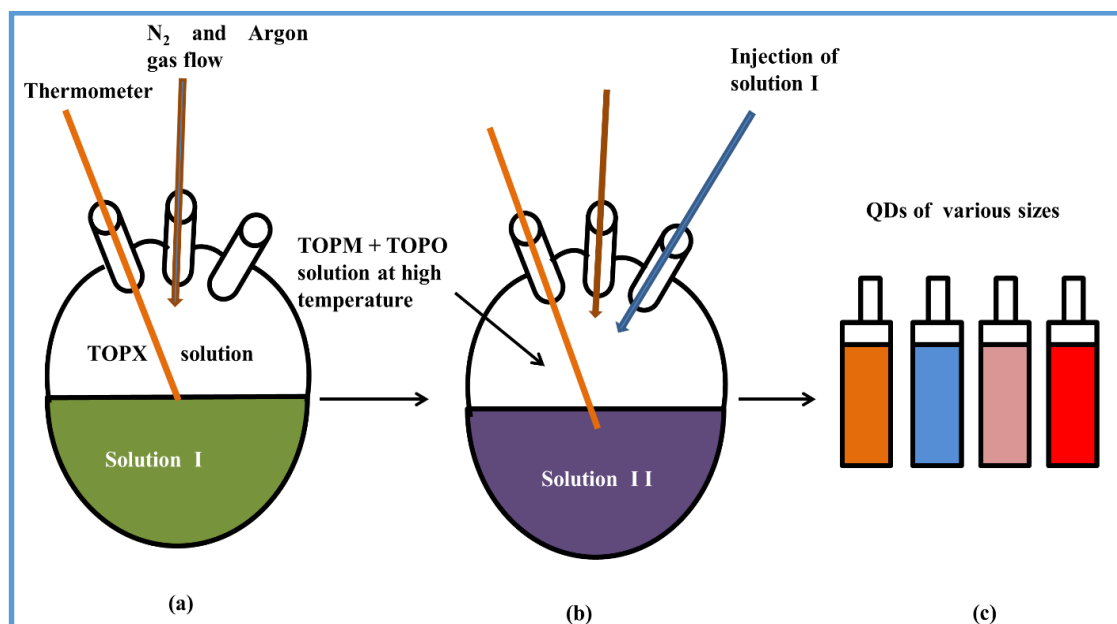


Figure 2.2: (a) TOPX (X = S, Se, Te) solution (b) TOPM (M = Cd) and TOPO solution mixed at an elevated temperature (c) tiny aliquots of the solution chosen at varied time intervals throughout the synthesis method.

The third step is to mix the TOPX solution with the TOPM + TOPO solution at high temperature. The formation of QDs has been validated by the transformation in the colour of the solution. Small aliquots of the solution have been drawn at periodic interval of time and represent the different size of QDs [147]. These aliquots change

the colour when exposed to UV or VIS or IR radiation depending upon the size of QDs due to the quantum confinement effect.

The capping agents perform a vital role in maintaining the dimensions of QDs. The capping agents at higher temperature continuously adsorbed and desorbed on the surface of QDs and determine the size of nanocrystals. The quantity of TOPX also changes the size of nanocrystals by reacting with the TOPM + TOPO solution. As the temperature decreases, the surfactants tightly bound to the surface of nanocrystals and remain dispersed in the solution. The process is uniform and leads to the formation of monodisperse QDs.

PbSe QDs have been synthesized by Capek *et al.* [148] with the help of the hot-injection approach. The synthesis process has been carried out in nitrogen and argon gas filled glove box. The solution I has been prepared by adding 0.2 molar and 0.4 molar Se powder in the desired amount of TOP solution. The solution has been stirred for 16 h to obtain pure TOPSe solution and to remove the excess of selenium powder from TOPSe solution fractional distillation has been performed in which colour of solution changes from yellow to colourless. Then, the solution has been cooled to room temperature. Solution –II has been synthesized by dissolving the requisite quantity of PbO, oleic acid (OA), and n-hexadecane. The solution has been heated and stirred until it becomes clear. 4 ml solution of TOPSe, TOP and diphenyl phosphine has been added immediately to the solution – II. The temperature of the mixed solution has been lowered to attain the uniform growth of NCs. A number of aliquots have been extracted at different time intervals. These aliquots have been dispersed in toluene, acetonitrile and ethanol solutions and centrifuged to obtain QDs. For further purification, the QDs has been put in hexane. Then ethanol has been added to precipitate QDs followed by centrifugation. The size of QDs has been observed to change with the variation in the ratio of lead oxide to oleic acid and the amount of diphenylphosphine and TOPSe solution.

The synthesis of QDs has been categorized into two basic steps of nucleation and growth. This further depends on the reaction temperature and also on the monomer quantity of the reactants. For temperature effect: entities solely react once they strike. This lead to the initiation of reaction provided that the striking particles have sufficient energy to initiate the reaction. This minimum

energy needed to initiate the reaction is generally known as the energy of activation. The particles enclosed in the area on the right side of figure 2.3 (a) have enough activation energy to start the reaction on mixing. A majority of species don't have enough energy to react. Thus, the temperature varies, generally, in between 140 °C, 170 °C, 210 °C and 220 °C for a constant time (e.g. 60 seconds) for the QDs synthesis through the hot-injection approach. The band gap shows a decrease and the PL shows a movement towards longer wavelength with the rise in reaction temperature. Thus, monomer species have more energy for increased reacting temperature and grow to increase its size, which result in a decrease in the band gap.

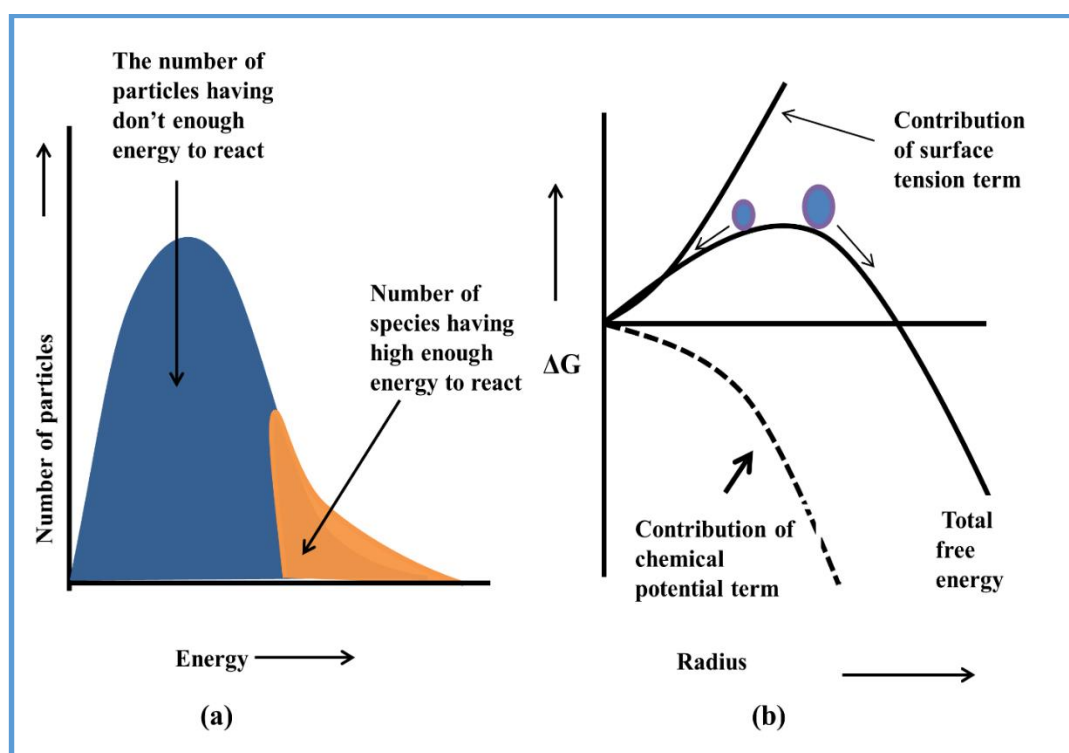


Figure 2.3: (a) Maxwell Boltzmann distribution curve for the monomer species involved in the reaction (b) Change in total free energy.

Classically, the monomer concentration effect is related to system's free energy. If the reaction process lowers the system's total free energy, then the reaction will occur. The free energy is divided into two terms *i.e.* surface tension term and chemical potential term (figure 2.3 (b)). The surface energy term is positive while the chemical potential term is negative [149]. The surface tension term arises due to the force

between the newly formed NCs boundary and the surrounding solution. The difference in chemical potential arises due to the number of crystal forming entities and the same entities inside the NCs. Generally, the NCs grow continuously if they overcome a certain critical size. The thermodynamic stability of QDs can be understood on the basis of the chemical potential well. The monomers inside the chemical potential well continuously attach and detach on the surface of NCs. The monomers tend to detach when size increases above a certain limit. In quick injection, process precursors are decomposed into a large number of monomers. These monomers form new nuclei. As the concentration of monomers decreases, the size of the new nuclei reaches to a certain limit but, growth continued through the Ostwald ripening. The monomers have not enough energy to cross the chemical potential well when the concentration of monomers decreases a certain level. At this stage, the extra precursor is added to increase the growth rate. As the monomers are consumed, the mean size will increase step by step whereas the dimensional distribution fairly broadens due to ostwald ripening [150]. Concisely, the initial concentration of the monomers and also the temperature of the reaction are the primary conditions for the productive synthesis of QDs with small dimensional spread.

2.1.2.1.3 Arrested precipitation (co-precipitation) approach

Co-precipitation method is used to precipitates the materials which are soluble under ambient conditions. Generally, in co-precipitation approach the metal salts or oxides (MCl, MOH, MO, etc. where M is metal) of two different materials are precipitated. The precipitation process started in solution with the help of some precipitating agent (*e.g.* sodium hydroxide). Precipitates are agitated for several minutes depending upon the properties of the material. Thereafter, the precipitates are separated, cleaned by distilled water (DW) centrifuged and dried at the required temperature. The general scheme for the synthesis for MX (X = S, Se, Te) NCs has been divided into three steps [151]. The first step involves the dissolving of precursor materials like MY (Y = chloride, nitrates, etc.), capping agent, X powder source material *etc.* in the desired amount of water. The solution is stirred until all the precursor materials are completely dissolved. In the second step, the required molar solution of the precipitating agent (sodium hydroxide) is to prepared. In the third step, the solution prepared in the first step and second step are mixed (figure 2.4).

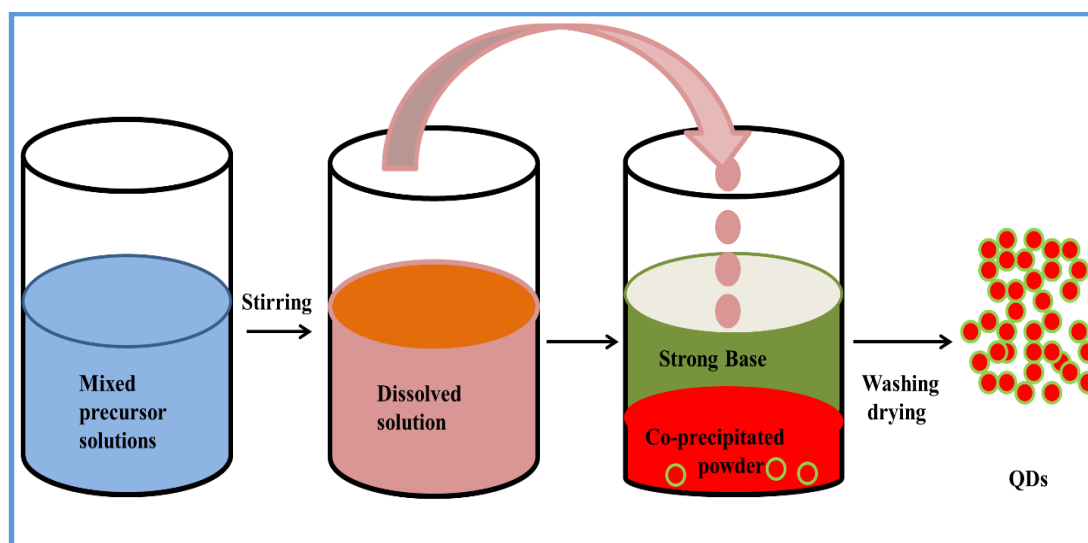


Figure 2.4: Co-precipitation technique for preparations of QDs.

This can be accomplished in four steps. The first step is to add the precursor solution dropwise to the sodium hydroxide solution. In a second step, add the sodium hydroxide solution dropwise to precursor solution. In a third step, mix both the solutions simultaneously in a beaker containing buffer solution at constant pH. In a fourth step, mix both the solutions simultaneously in another beaker and separate the precipitates continuously. The NCs are precipitated in solution. These QDs are washed and centrifuged with DW or ethanol to get rid of the impurities. The obtained QDs are dried below the synthesis temperature for the desired time. Fine powder of NCs has been formed using mortar pestle and are ready for characterization.

The size of nanocrystals and the optical properties can be altered by changing the value of pH [152], [153]. After mixing the two solutions, the time of stirring also affects the size of NCs [152]- [154], [155]. The type of capping agents also governs the size of NCs [156]. Nanocrystals size can also be controlled by varying the X precursor solution [151]. The size of nanocrystals can also be varied with the change in the molar ratio of the doping material in the original composition [157].

2.1.2.1.4 Hydrothermal method

In the hydrothermal method, nanocrystals are synthesized in an aqueous solution at high temperature and high vapour pressure. The main advantage of the hydrothermal method is to form crystalline materials which are not possible to

synthesize by other approaches directly. The hydrothermal approach provides good crystal growth, control on composition and phases of NCs. The materials, like silicates, which are not soluble under normal conditions have been synthesized at high temperature and high pressure using this approach. The size and other properties of NCs show dependence on the pH of the solution, reaction time, temperature and pressure inside the autoclave [158]–[163]. An autoclave is laboratory equipment, generally, made up of steel and that can bear high temperature and pressure.

The zinc selenide/zinc sulphide (core/cell) QDs have been synthesized by Dan Zhao *et al.* [159] with the hydrothermal approach. The precursor materials, like sodium borohydride, selenium powder, zinc chloride, N-acetyl-L-cysteine, sodium hydroxide are used. Solution-I has been synthesized by mixing the required molar ratio of sodium borohydride and selenium powder in DW. The solution has been stirred continuously till sodium hydroselenide formed. Solution-II has been synthesized by mixing ZnCl and N-acetyl-L-cysteine in 50 mL DW. The solution has been stirred continuously for approximately 30 minutes. The pH of the solution has been fixed to a particular value by adding the required molar solution of sodium hydroxide. Then, solution-I has been added to solution-II with continuous stirring. After this, load the mixed solution in an autoclave and put the autoclave in a furnace. The temperature of autoclave has been fixed to 200⁰C for 40 -80 minutes. Then take out the autoclave from the furnace and cool it to room temperature. The required QDs have been obtained by centrifuging the solution at 4000 rpm. Generally, the hydrolysis and other reactions take place at high temperature and pressure inside the autoclave. Main disadvantages of this approach are the possibility of an explosion, costly autoclaves and reaction cannot be perceived directly.

2.1.2.1.5 Cation-exchange of QDs

The direct methods of QDs synthesis require a careful approach to understand the effect of nucleation, growth and temperature kinetics [164]. The cation-exchange (CE) method has been employed under the circumstances in which direct approaches are inadequate for the synthesis of NCs of good quality [165]. The ion-exchange (IE) approach may be divided into cation-exchange and anion-exchange (AE) approach. In the CE approach, the positive ion of parental NCs has been replaced by the positive ion of newly formed NCs and negative ion of parent NCs remains unaffected. The anion-

exchange approach has been generally not preferred due to high synthesis temperature, a longer time for synthesis, internal strain induced in NCs structure, mismatch of lattice sites among parent and newly formed NCs [166]. So, cation-exchange is preferred over anion exchange. Cation-exchange depends upon the solubility product (K_{sp}). The efficient cation-exchange has been probable if the high value of K_{sp} (parent NCs) changes to the low value of K_{sp} (newly formed NCs).

Chen *et al.* [46] have reported the synthesis of Ag_2Te QDs by cation exchange approach. Sodium hydrogen tellurium solution has been formed by mixing 0.04g sodium borohydride and 0.06 g tellurium powder in 1 ml deionized water. The solution has been stirred for 8 h in an ice bath. The solution of cadmium has been formed by adding 0.095 g cadmium chloride in ten milliliter water. Silver nitrate solution has been formed by adding 0.033g silver nitrate in one milliliter water. The solution of glutathione has been formed by adding 0.123 g glutathione in ten milliliter water. This solution has worked as a stabilizer solution in reaction. Cadmium chloride solution (0.05 M) has been mixed with glutathione solution (0.04 M) in a beaker. The pH of the solution has been adjusted to 10 by adding sodium hydroxide solution with continuous stirring for 15 minutes. After this, sodium hydrogen tellurium (0.5 M) solution has been added with continuous stirring at a temperature of 95 °C. Different aliquots of the solution are drawn at quarter-hour, half hour, a quarter to hour, and hour provide the various size of CdTe QDs. Ag_2Te QDs of various sizes have been prepared by adding silver nitrate solution (0.2 M) in different aliquots of CdTe QDs. The difference in UV-VIS-NIR absorption and emission spectra of CdTe and Ag_2Te QDs have confirmed the successful cation exchange process. Further, the purification of Ag_2Te QDs has been performed by centrifugation. The disadvantage of this approach is the occurrence of a change in the volume of the newly formed NCs from parent NCs due to lattice mismatch [167].

2.1.2.1.6 Vapour phase method or Molecular beam epitaxy (MBE)

MBE has been used for the synthesis of high precision NCs. This is a solid phase synthesis approach for NCs. High energy electron diffraction tool of MBE is employed to analyze the growth of different layers deposited on the substrate material. In MBE, basically, the ultrapure elements are heated to evaporate and then condensed on the substrate wafer. The elements at the time of condensation at the substrate wafer may

react and form suitable material. For the synthesis of gallium arsenide material, ultra-pure gallium and arsenic elements have been used. In this method, beam defines that evaporated atoms inside the vacuum chamber have very little interaction with one another and whatever other gases until the vapours reach the wafer, due to the involvement of large distance of the beams *i.e.* the mean free paths. The substrate has been uniformly rotated to confirm a smooth growth above its surface. To control which type of semiconductor is deposited on substrate attained by operating mechanical shutters of cells. Generally, growth kinetics in MBE has strongly affected the size, density, and composition of self-assembled InAs QDs. Low-density InAs/InGaAs QDs having emission at the longer wavelength (1.3 μm) for single photon operation have been synthesized by the G Trevisi *et al.* [168].

ZnMnTe/ZnSe QDs has been synthesized by W.C. Fan *et al.* [169]. The synthesis can be divided mainly into two steps: 1) deposit ZnSe buffer on the substrate material, 2) deposit ZnMnTe QDs on the ZnSe buffer layer. The temperature of zinc, manganese, selenium, and tellerium maintained at 294 °C, 695 °C, 178 °C and 310 °C severally of an effusion cell. The growth and desorption checked by reflection high-energy electron diffraction (RHEED). Firstly, GaAs (100) substrate etched and then dried. For the ZnSe buffer layers' deposition substrate temperature fastened at 300 °C and therefore the rate is maintained at 0.4 $\text{\AA}/\text{s}$. For the deposition of ZnMnTe QDs, ZnSe buffer subjected to deposition of Mn, Zn and Te each for 5s. The desired number of monolayers have been deposited by the above procedure and then the QDs are capped by ZnSe 50 nm layer.

Germanium (Ge) QDs has been synthesized by MBE by Qimiao *et al.* [170]. Ge has an indirect bandgap. In this synthesis, of tensile strained Ge QDs by the MBE changes indirect band gap of Ge to direct band gap. In the QDs, the strain field has been found to be non-uniform. Strain, produced in the material strongly alters the electronic band structure through the deformation potentials. As a result, there is an increase in bandgap energy and a blueshift in the optical emission occurs which may surpass the confinement effects. MBE has effective check over the vertical position of QDs and gives rise to highly efficient luminescence defect-free structures [171].

Top to the down method has been expensive so colloidal approaches are generally preferred by the researchers. In down to up approaches, the sol-gel has been

found to be worthy for the thin film synthesis. The main disadvantage of this approach in the course of synthesis method is the difficulty in the vital management of aerogel pores. Hot-injection method provides good quantum yield but, the temperature used in this method is very high approximately above 250 °C. QDs synthesized by hydrothermal method shows less number of defects in the lattice formation but high temperature and pressure may lead to the explosion of autoclaves. The CE technique is employed to synthesize the QDs that are hard to create directly through the above approaches. Co-precipitation route is comparatively easier, cost-effective in comparison to the other approaches and suitable crystal structure of material may be obtained.

2.2 Characterization Technique

2.2.1 X-ray Diffractometer

The X-ray diffractometer (XRD) of Shimadzu Analytical: XRD 6000 with Cu-K wavelength 0.154056 nm has been used for structural analysis (figure 2.5). The arrangement of various parts utilized in XRD has been depicted in figure 2.6.

The XRD system consists of an X-ray tube (source of X-ray), incident beam optics (includes different conditions before it hit the sample), goniometer, sample and sample holder, the receiving beam optics (includes different conditions after the beam encountered the specimen), sophisticated detectors (to count the various X-rays scattered from the specimen) and a data processing unit (software) which controls the overall operation of the system. In XRD, X-rays are generated within the tube by the bombardment of fast electrons on the target material.

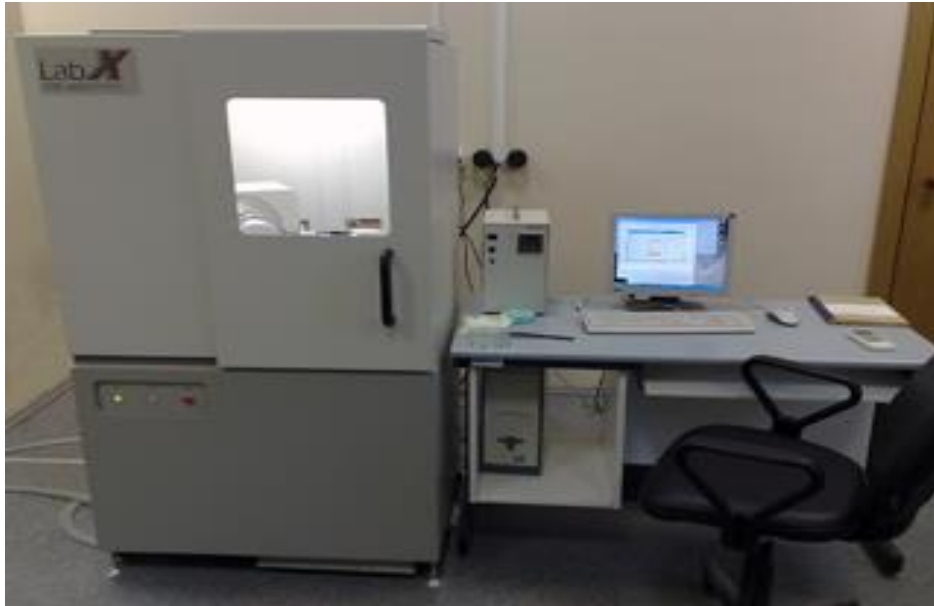


Figure 2.5: X-Ray diffractometer used for XRD analysis.

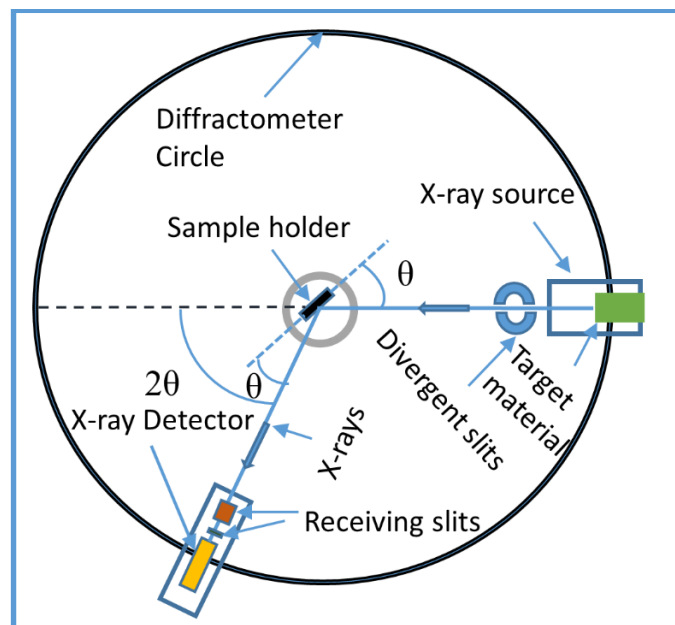


Figure 2.6: The arrangement of different components used in X-Ray diffractometer experiment.

These X-rays have been filtered to generate monochromatic X-ray. These monochromatic X-rays are narrowed and focused to hit the sample placed in the centre of the goniometer. X-ray, after diffraction from the different planes of samples, satisfies the Bragg equation (2.1) *i.e.* forms constructive or destructive interference.

$$2d\sin\theta = n\lambda \quad (2.1)$$

where d is the interplanar distance of NCs, λ is the wavelength and θ is the diffracted angle of X-rays. These are falls on the receiving slit which further detected by the scintillation detector. The detector processes the signal and transforms the signal to the count rate. These count rates are further processed by the software to convert in graphical or analytical form of data.

2.2.2 Transmission Electron Microscopy (TEM)

TEM is employed to check the particles having a size roughly less than hundred nanometer. TEM has shown resolution approximately 0.2 nm at 200 keV [172]. The different components of TEM have been shown in fig 2.7. TEM consists of mainly six parts: 1) Electron gun which supplies the continuous electron generation, 2) closely spaced magnetic coils which are used to focus the electrons on the sample by the magnetic field. These are positively charged and used to accelerate the electrons, 3) sample used ought to be ultra-thin thus, that electron wave will simply go through the sample, 4) magnetic coils used to magnify the transmitted electron beam so that these can be easily identified, 5) fluorescent screen is used to recognize the transmitted electrons signals, and 6) detectors used to detect the backscattered electrons from the sample. On the fluorescent screen, the incoming electrons produce the possible diffraction pattern. Ultra-thin preparation of the sample for TEM analysis has been done by dispersing the sample in a suitable solvent and sonicate to separate aggregated particles. Thereafter, put the sample on the substrate and dry it completely so that the solvent evaporates completely. In this process, sample particles are widely spaced on the substrate. Monodisperse and polydisperse distribution of the QDs have been obtained by calculating the various parameters from TEM images [173].

The photograph of the TEM instrument (FEI (FP 5022/22-Tecnai G2 20 S-TWIN)) has been shown in Figure 2.8. “High-resolution transmission electron microscopy (HRTEM)” has been employed to observe the lattice fringes of QDs. HRTEM images form columns of atoms on the screen by the phase change of electron waves. In HRTEM, images are formed on the phase contrast imaging technique. The electrons generating from source materials work as waves in this technique. HRTEM works on the basic operation which consists of interference between the transmitted and diffracted electron waves. The electron waves are diffracted by the sample and

others are passed without diffraction. This diffraction of electron waves with the sample is complex and computer added simulation required to analyze diffraction and phase changes takes place at the screen. The resolution of HRTEM images is very high *i.e.* approximately less than 0.1 nm. In HRTEM images, phase contrast has been achieved either by removing the objective lens or by inserting a large aperture objective lens.

Selected area diffraction (SAD) has been used to find the crystallographic information's. The electrons waves are moving through the sample and fall on the screen. This forms a series of spots on the screen by electron waves. This is due to the size of electron waves which is approximately equivalent to the spacing between the atoms column in crystals structure. The SAD aperture is placed below the sample to acquire the patterns of the desired beam passed through the samples. The little holes have been formed on the SAD aperture used to select the desired area diffraction pattern of the sample. For a single crystal, a clear series of spots are formed for SAD patterns. For the polycrystalline materials, diffused rings are observed due to the number of crystals structure involved in diffraction patterns. The series of spots have been used to calculate the interplanar distance (d). The formula used to find interplanar distance [174]:

$$rd = \lambda L \quad (2.2)$$

where λL is camera constant and r is the separation between the central spot and other spots.

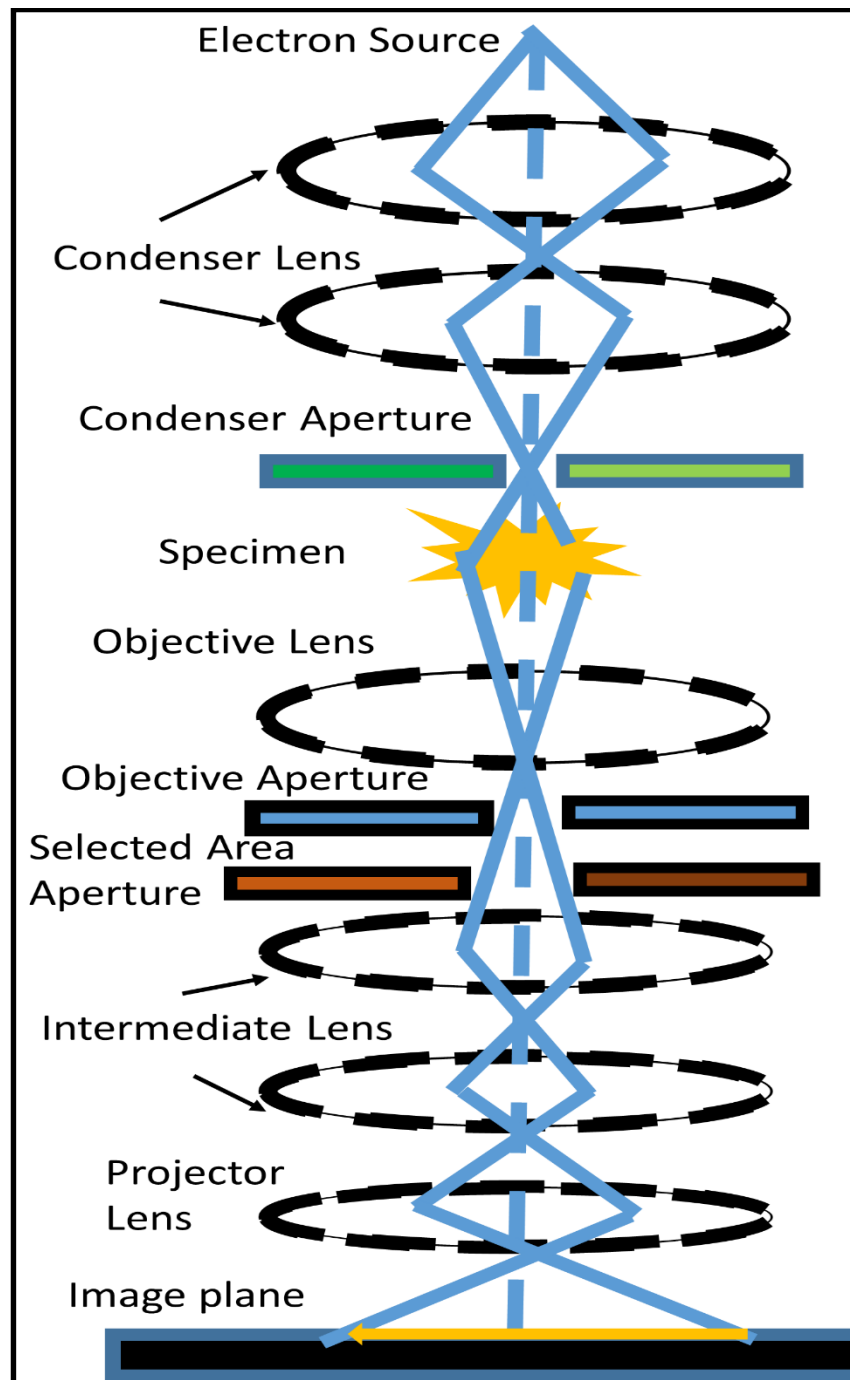


Figure 2.7: Different basic components used in the transmission electron microscope.



Figure 2.8: Transmission electron microscope used for morphology analysis.

2.2.3 Energy Dispersive X-ray Spectroscopy (EDX or EDS):

EDS is a systematic technique employed for the fundamental elemental investigation of a material. The fundamental principle of EDX is based on the fact that every individual element has an individual atomic structure and that gives a set of unique peaks in the electromagnetic emission spectrum. EDS setup primarily consists of 4 components; i) the excitation supply, ii) X-ray detector fitted in instrument, iii) pulse processor associated an instrument and iv) analyser. Excitation source (high energy electron beam) has been used to fall on the sample surface. This process emits X-rays and that are converted into voltage signals by the detector. This voltage signal is measured by the pulse processor and sent to an analyzer for the analysis and data display. The data analysis provides different elements present in the sample and the atomic percentage of each element present in the sample.

2.2.4 Optical characterizations

2.2.4.1 UV-VIS-NIR Spectrophotometer

The photograph of the UV-VIS-NIR spectrophotometer instrument (Perkin Elmer model no LS 55) has been shown in Figure 2.9. In UV-Vis spectrophotometer, the continuous chosen electromagnetic radiations are allowed to interact with the sample. With the absorption of the incident radiations, the electrons have been getting desirable energy and are excited to the higher levels which may include vibrational and

rotational energy levels. The different components of UV-VIS-NIR spectrophotometer have been shown in figure 2.10. Samples employed in the UV-VIS-NIR spectrophotometer consists of powder or powder dispersed in water (or any solvent) or thin film deposited on the substrate. Powdered samples dispersed in the solvent are taken in a cuvette and the reference cuvette contains the same solvent. In this, the radiations are passed through the reference and the sample material. Then, these are compared and transmittance intensities are recorded by the detector. Suppose I_0 is the incident intensity on both the cuvettes and the transmittance intensities are I_1 and I_2 for the reference cuvette and the sample cuvette respectively. Then, the absorbance has been calculated by the formula; $\log(I_1/I_2)$ [175].



Figure 2.9: UV-VIS-NIR spectrophotometer used for the analysis of QDs.

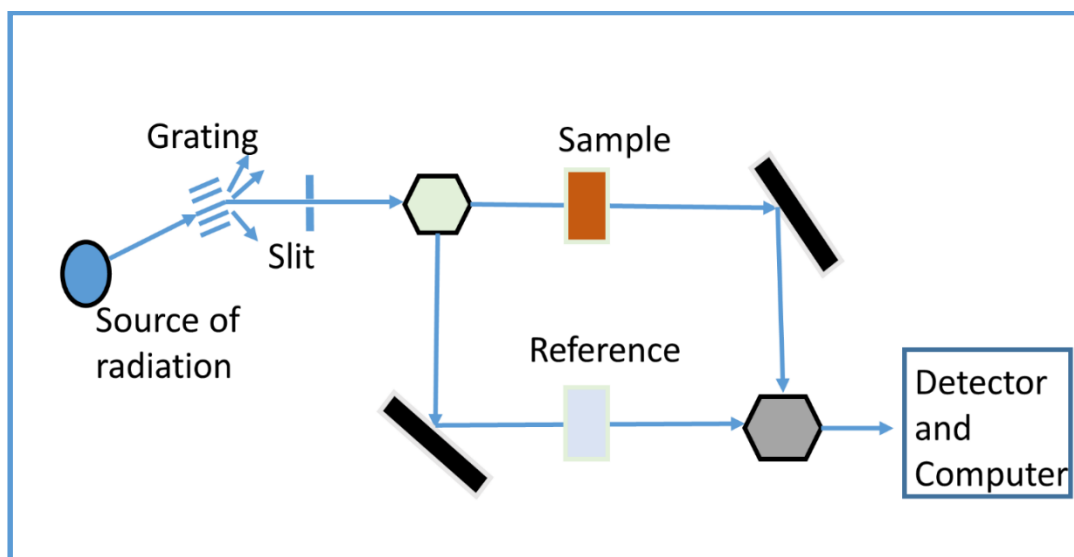


Figure 2.10: Block diagram to show the operation of UV-VIS-NIR Spectrophotometer.

2.2.4.2 Fourier transforms infrared spectroscopy (FTIR)

FTIR is the most useful technique for identifying materials organic or inorganic. The FTIR instrument (RZX (Perkin Elmer)) photograph has been shown in figure 2.11. The IR are absorbed by the molecules and excites the molecules into the higher energy levels (vibrational levels) is the fundamental principle of FTIR. The quantity of energy absorbed from the IR radiation depends upon the lowest state energy (at rest position) and excited state energy of vibrations of the molecules. These absorbed radiations show the fingerprints of the molecular structure. A simple block diagram of the FTIR spectrometer has been shown in figure 2.12. FTIR comprises of various parts like infrared supply, a beam splitter, detectors, and Fourier transform. Silicon carbide is the most commonly used source in FTIR. Most commonly used material for detectors in mid-IR is liquid nitrogen cooled mercury cadmium telluride. The FTIR spectrometer is associated with an interferometer to transform the wavelength from a broad IR supply. The intensity of the transmitted radiations has been measured using the detector and also the signal received within the type of an interferogram. This interferogram has the dimension of length. Fourier transform has been used to convert the dimension of the length into the dimension of wavenumber (in cm^{-1}). This data is further analyzed with a computer and presented as plots of intensity versus wavenumber.



Figure 2.11: FTIR photograph used for the analysis of QDs.

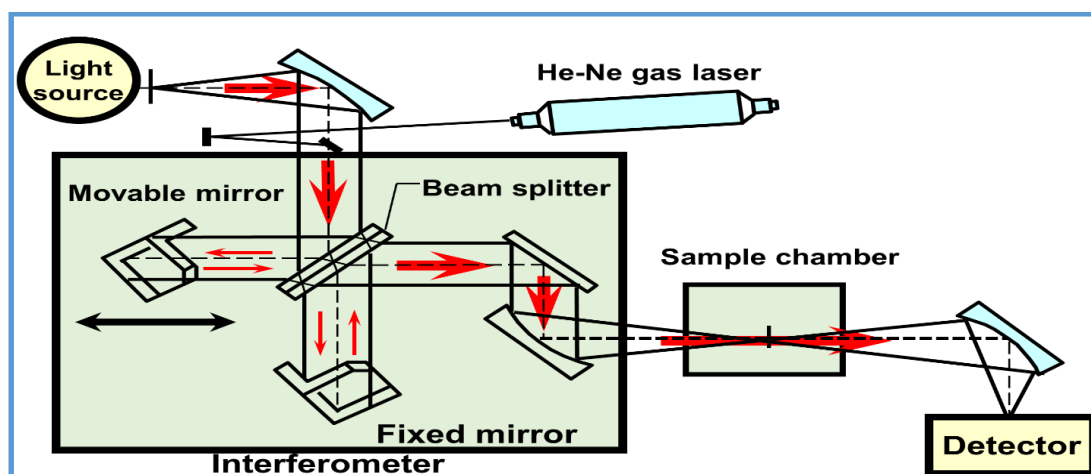


Figure 2.12: Arrangements of different components used in FTIR.

2.2.4.3 Raman spectroscopy

Raman spectroscopy is a useful molecular spectroscopy technique for identifying the information of molecular vibrations and the crystal structures. Raman spectroscopy is a non-destructive and a non-contact technique for probing interactions of materials at the molecular level. The Raman spectroscopy instrument (Reinsaw Raman Spectrometer) photograph has been shown in figure 2.13.

Raman spectroscopy consists of several components which include a source (consisting of laser light), Raman scattering (Raman effect) and detectors (figure 2.14). Monochromatic laser light has been directed to fall on the sample. The incident light creates an inelastic scattering inside the sample. In inelastic scattering, when incident photon interacts with the molecule resulting in an excitation of molecule to the upper virtual energy level for a short time. Then, the excited molecule eases itself by releasing a photon of light having different energy compared to the incident photon. After the scattering, the sample has been lying in a different rotational or vibrational state. This is known as the Raman effect. Raman effect has been related to the polarizability of the electron in a molecule. The scattered lights after striking on the sample have been captured by charge coupled device (CCD) detectors. Raman spectrometers use high-quality, optically well-matched components because the Raman scattering possesses a weak signal.

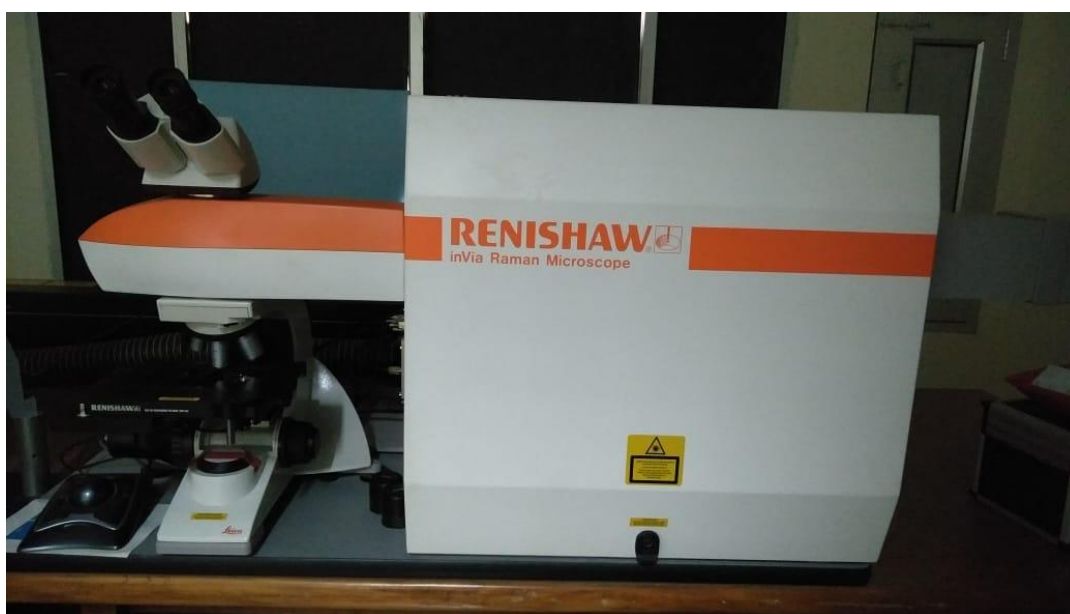


Figure 2.13: Raman Spectroscopy with Photoluminescence Spectrophotometer photograph used for the analysis of QDs.

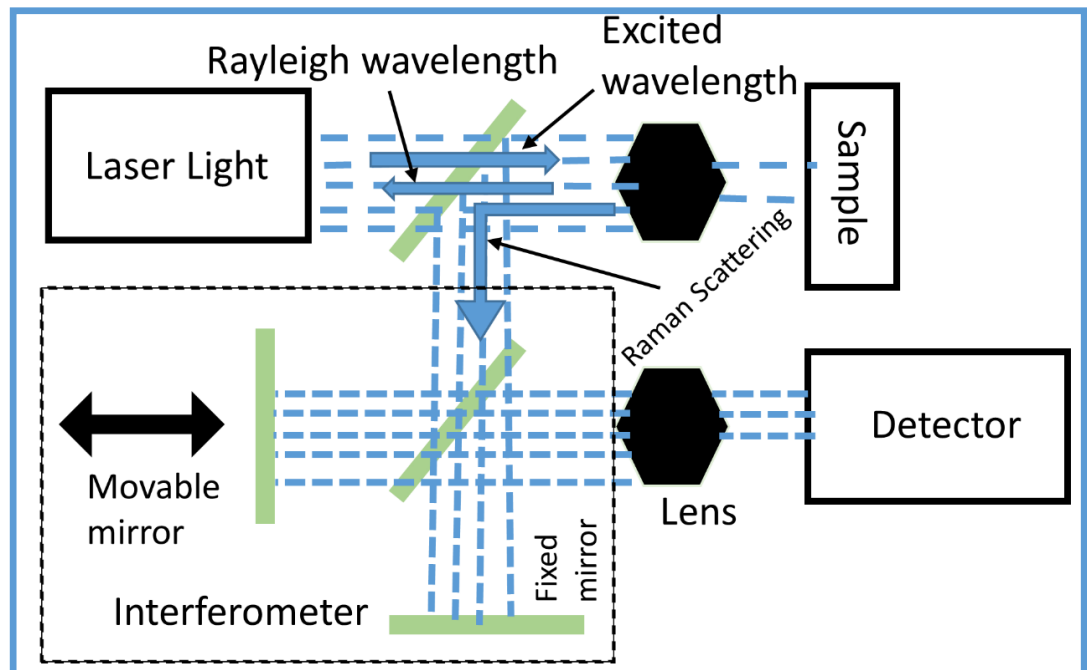


Figure 2.14: Different components used in Luminescence Spectrophotometer.

2.3 Some relevant equations

1. The crystallite size (D) of the nanoparticles and QDs are worked out by employing Scherrer's formula [176];

$$D = k\lambda / \beta \cos\theta \quad (2.3)$$

where λ , β and θ denote the wavelength of the X-rays used, FWHM and diffraction angle respectively.

2. The lattice parameters a , b and c of the unit cell have been calculated using the relation

$$\frac{1}{d^2} = \frac{h^2}{a^2} + \frac{k^2}{b^2} + \frac{l^2}{c^2} \quad (2.4)$$

For orthorhombic structure

where d is the space between successive planes.

3. The strain (ϵ) and the size of the nanoparticles and QDs have been calculated using Williamson-Hall (W-H) equation [177].

$$\beta \cos\theta = \frac{k\lambda}{D} + 4\epsilon \sin\theta \quad (2.5)$$

The dislocation density (δ) has been calculated by employing the formula [178]:

$$\delta = 1/D^2 \quad (2.6)$$

where D is the average crystallite size.

4. The optical band gap has been calculated using Tauc's Plot.

$$\alpha h\nu = K(h\nu - E_g)^n \quad (2.7)$$

where E_g is the optical bandgap of nanomaterial, K is a constant, and value of $n = 1/2, 3/2, 2$ and 3 for allowed direct transitions, prohibited direct transitions, allowed indirect transition, and prohibited indirect transitions respectively [179], [180].

5. According to Beer–Lambert's relation, the absorption coefficient;

$$\alpha = 2.303A/d \quad (2.8)$$

where A is the absorbance and d is the path traversed by light in the cuvette.

6. The optical energy band gap for the QDs have been calculated using the formula

$$E_{nano} = hc/\lambda \quad (2.9)$$

where λ , h and E_{nano} are the wavelength used, Planck's constant and energy band gap of the QDs respectively.

7. The size of QDs has been calculated using Brus (EMA) equation [15]

$$r = \frac{-\left(\frac{1.8e^2}{4\pi\epsilon\epsilon_0}\right) + \sqrt{\left(\frac{1.8e^2}{4\pi\epsilon\epsilon_0}\right)^2 + (E_g^{nano} - E_g^{bulk})\frac{\hbar^2}{2}\left(\frac{1}{m_e^*} + \frac{1}{m_h^*}\right)}}{2(E_g^{nano} - E_g^{bulk})} \quad (2.10)$$

where E_g , ϵ , ϵ_0 and m_e^* (m_h^*) are the bulk band gap of the material, dielectric constant of bulk material, vacuum permittivity and the effective masses of the electrons (holes) respectively.

8. Exciton radius has been calculated using Griffiths equation [181]

$$a_0 = \frac{4\pi\hbar^2\epsilon\epsilon_0}{e^2}\left(\frac{1}{m_e^*} + \frac{1}{m_h^*}\right) \quad (2.11)$$

where a_0 is Bohr exciton radius.

CHAPTER- 3 *

“Optimization of conditions for the synthesis of Ag₂Se QDs”

* “**S. CHAND** and P. SHARMA, *Synthesis and characterization of Ag-chalcogenide nanoparticles for possible applications in photovoltaics*, **Materials Science - Poland**, vol. 36, no. 3, pp. 375–380, 2018”.

“**S. Chand**, D. Sharma, V. Sharma, and P. Sharma, *Morphological and optical study of Ag₂Se quantum dots*, **AIP Conf. Proc.**, vol. 2009, pp. 1–5, 2018”.

The properties of QDs have been influenced by the various synthesis techniques and parameters involved in the techniques. Wet chemical approach is suitable for the synthesis of QDs for applications in the biological field. The various parameters of wet chemical approaches like initial precursors, pH, capping agents, the temperature of the solution during synthesis, *etc.* have been found to alter the structural, optical and electrical properties of nanocrystals. The various parameters of wet chemical approaches have also been responsible for deciding the size of QDs. Capping agents have been used to prevent the agglomeration of nanocrystals to obtain the desired size QDs. In some cases, excessive use of capping agent may inhibit the process of formation of nanocrystals. On the other side, in some cases, smaller use of capping agent may lead to the formation of large sized particles. This chapter includes the different conditions to synthesis Ag₂Se nanoparticles and QDs. The synthesized samples have been studied by X-ray diffraction, transmission electron microscope, UV-VIS-NIR absorption spectroscopy.

3.1 Introduction

During the last decade, semiconducting chalcogenide nanocrystal has appealed much attention because of their numerous applications in various fields. The binary chalcogenide semiconductors have been shown size-dependent optical properties due to quantum size effects. Silver selenide (Ag₂Se) is a representative of the silver chalcogenide class and occur in two phases [182]–[184]. The first phase is cubic (α -Ag₂Se) and forms above 133°C (high-temperature). This phase is also known as a superionic conductor. The second phase is orthorhombic (β -Ag₂Se) and forms below 133°C (low-temperature). This phase is nonmagnetic, possess narrow-band-gap and shows thermochromic properties [185]. Ag₂Se has numerous application in the field of the photodetector, magnetic field sensors, photo rechargeable secondary batteries, solar energy conversion, optoelectronics, switching devices, electrochemical potential memory devices, superionic conductor and luminescent devices, *etc.* [186]–[193]. Ag₂Se QDs have tunable optoelectronic properties means the emission wavelength can be tuned by changing the size of QDs due to quantum confinement. The surface modification of Ag₂Se using a capping agent can alter the properties like functionality,

charge, and reactivity due to the localization of the electron-hole pairs in three dimensions.

A number of methods have been used to synthesize silver selenide nanoparticles such as hydrothermal method, co-precipitation method, sol-gel method, sonochemical method *etc.* [194], [195]. However, the co-precipitation and hydrothermal methods have been adopted for the preparation of nanoparticles and QDs. The co-precipitation approach has been preferred over the other approaches because of its numerous advantages like economical raw materials, easy treatment as compared to the other methods. To prepare the nanoparticles of the small size, the capping agents (surfactant materials) have been used. To amend the surface of NCs, through the functional groups like N-H, O-H, COOH, and C-O, 2-mercaptoethanol and hydrazine hydrate (H.D.) have been used as the capping and reducing agents.

3.2 Synthesis and characterization of Ag₂Se nanoparticles

3.2.1 Experimental details

Ag₂Se nanoparticles have been synthesized by co-precipitation approach as given in detail in chapter 2. All the initial precursor materials have been of analytical reagent (AR) grade and used as received. The schematic diagram for the synthesis process has been shown in figure 3.1. Three samples of Ag₂Se material have been synthesized and named as sample a, sample b and sample c. Synthesis of samples requires the preparation of two solutions I & II. For the synthesis of sample a, dissolve AgCl (0.00698 mol) powder into 20 ml of double DW (solution I). The solution I has been continuously stirred until completely dissolving. Now, add 0.5311 ml of 2-MPA (2-Mercaptoethanol) into the solution I. Also, keep the continuous stirring of the solution for 5 minutes so that silver atoms have been capped with the 2-MPA. Thereafter, add 0.5767 g Na₂SeO₃ and 3.2417 mL of NH₂NH₂.H₂O (H.D.) to solution I. The solution I has been heated and stirred at a temperature of approximately 75 °C for 2 hours.

The solution II has been prepared by dissolving the required NaOH powder in double distilled water to form 4 molar solution. The solution II has been heated and stirred until vapour starts forming. Then, solution II has been poured dropwise to the solution I with continuous stirring. During stirring the pH of the solution has been maintained at 13 (table 3.1). The solution has been stirred until precipitation starts

forming. Then, cool the solution to attain room temperature. To remove the excess of capping agents, the precipitates (ppt) have been washed with DW 3 times after equal intervals of 8 hours. For structural characterization, the ppt are dried at 60 °C and powdered uniformly employing a mortar-pestle. In the same way, the sample b & c have been prepared following the same procedure but with a variation of the ratio of AgCl to the 2-MPA, Na₂SeO₃/H.D. and varying the pH in the solution (table 1).

Table 3.1: Different precursor ratios and other parameters used for the synthesis of Ag₂Se samples.

Sample No.	Precursors				Molar ratio AgCl/2-MPA	pH of solution	Molar ratio Na ₂ SeO ₃ /H.D.
	AgCl (g)	Na ₂ SeO ₃	2-MPA	H.D.			
	(gm)	(gm)	(mL)	(mL)			
Sample a	0.955	0.5765	0.531	3.24	1	13	0.05
Sample b	0.955	0.5765	0.531	3.24	1	11	0.05
Sample c	0.955	0.5765	0.312	6.47	1.5	11	0.025

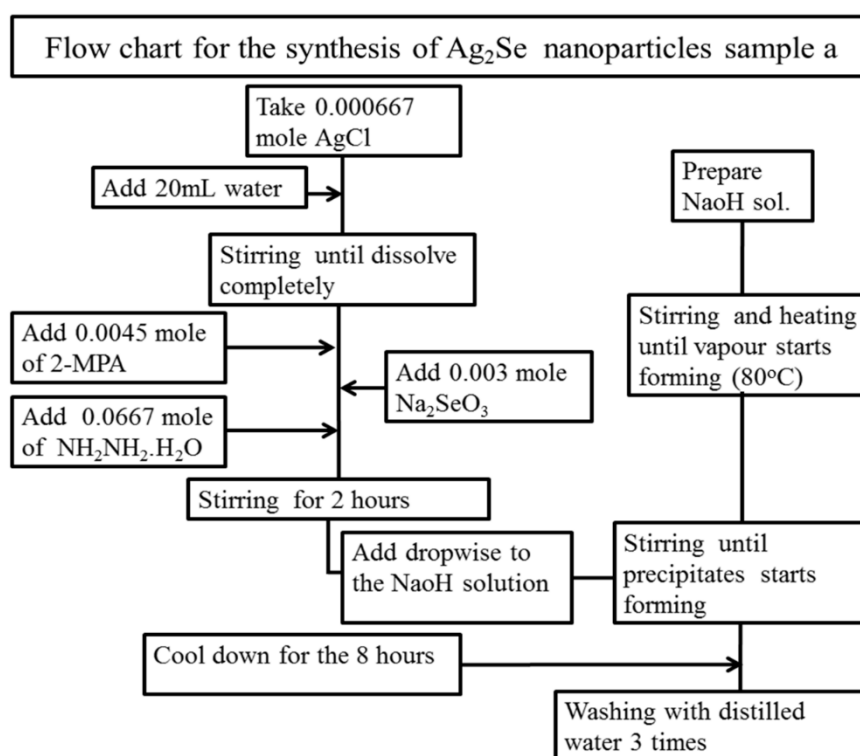


Figure 3.1: The schematic diagram of the synthesis process.

3.2.2 Structural properties

X-ray diffractograms of all the synthesized samples in the range 2θ from 20° to 60° have been shown in figure 3.2. Miller indices of synthesized samples have been found to correspond to the orthorhombic structure of Ag₂Se nanoparticles with the Joint Committee on Powder Diffraction Standards (JCPDS) card no 24-1041[196]. The peaks corresponding to each plane have been assigned h k l values using the standard JCPDS card no 24-1041. The full-width half maxima, Miller indices, d-spacing and lattice parameters of Ag₂Se nanoparticles has been given in Table 3.2. Diffraction peaks due to impurities have absent. This shows that pure Ag₂Se nanoparticles have synthesized.

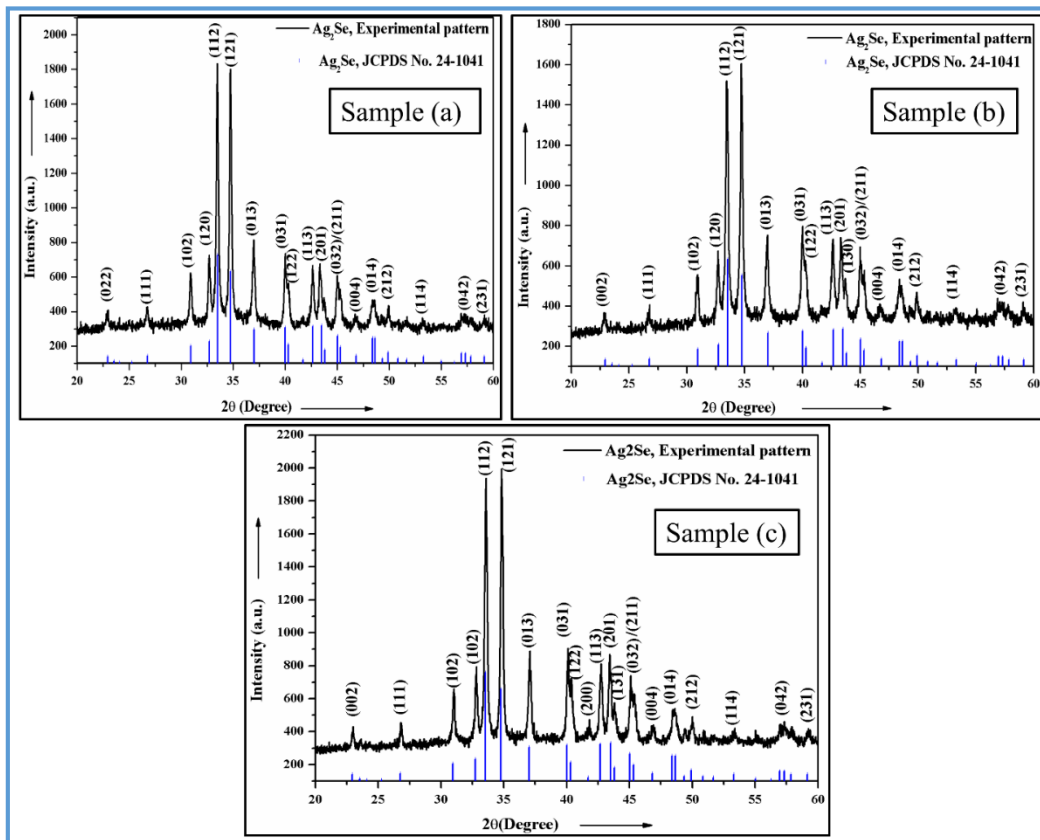


Figure 3.2: XRD patterns of different Ag₂Se nanoparticles.

The average crystallite size (D) for Ag₂Se samples has been calculated with the help of the Scherrer equation (2.3) by considering some high-intensity peaks [197].

The average crystallite size has been witnessed to increase from the sample a to c and has been given in table 3.2. The lattice constants values for samples have been calculated by taking different h k l values of planes. The values of lattice parameters have shown an irregular trend. From sample a to sample b, the lattice parameters have been detected to increase whereas from sample b to sample c the values of lattice parameters have been noticed to decrease.

Table 3.2: The various parameters calculated from XRD spectra of Ag₂Se samples.

Sample	2θ (°)	d (Interplanar spacing) (nm)		FWHM (°)	hkl	D (nm) (Crystallite size)		Lattice Constant (nm)	δ (nm ²) (x10 ⁻⁵)	
		Obs.	Stan.				Avg.			Avg.
a	30.92	0.288	0.289	0.26	102	31.68	33.5	a=0.4284 b=0.7032 c=0.7605	99.58	89.42
	32.69	0.273	0.273	0.25	120	33.10			91.26	
	33.48	0.267	0.267	0.25	112	33.17			90.89	
	34.75	0.257	0.258	0.24	121	34.66			83.19	
	36.98	0.242	0.242	0.24	013	34.88			82.15	
b	30.92	0.288	0.289	0.25	102	32.95	34.3	a=0.4315 b=0.7080 c=0.7778	92.07	85.15
	32.69	0.273	0.273	0.24	120	34.48			84.11	
	33.45	0.267	0.267	0.25	112	33.16			90.90	
	34.7	0.258	0.258	0.24	121	34.66			83.22	
	36.97	0.242	0.242	0.23	013	36.40			75.45	
c	31.03	0.287	0.289	0.23	102	35.83	37.4	a=0.4299 b=0.7055 c=0.7748	77.89	71.62
	32.82	0.272	0.273	0.22	120	37.63			70.62	
	33.58	0.266	0.267	0.22	112	37.70			70.35	
	34.81	0.257	0.258	0.23	121	36.18			76.38	
	37.08	0.242	0.242	0.21	013	39.88			62.86	

The broadening in the peaks of XRD data of different samples is present due to crystallite size, strain induced in the material and the instrument construction. Generally, the instrumental broadening has been subtracted by the software during characterization. Then the total peak broadening (β) has been written as;

$$\beta = \beta_D + \beta_\epsilon \quad (3.1)$$

where β_D and β_ϵ represent the contribution of crystallite size and strain respectively towards the broadening. Now, considering the crystallite size and strain amount towards the line broadening are independent to one another and the two carry a Cauchy-like profile. Then, the crystallite size and strain have been calculated by using the Williamson–Hall (W-H) equation (2.5) [198]. The Williamson–Hall (W-H) equation has also been known as uniform deformation model because it is considered strain to be alike in every directions of crystals. The strain induced in the material has been considered the same in all the directions. A graph has been plotted in between $\beta \cos \theta$ and $4 \sin \theta$ in y- and x-axis respectively. The slope and intercept of the linear fit of the graph have been worked out to calculate the strain and crystallite size in the figure 3.3.

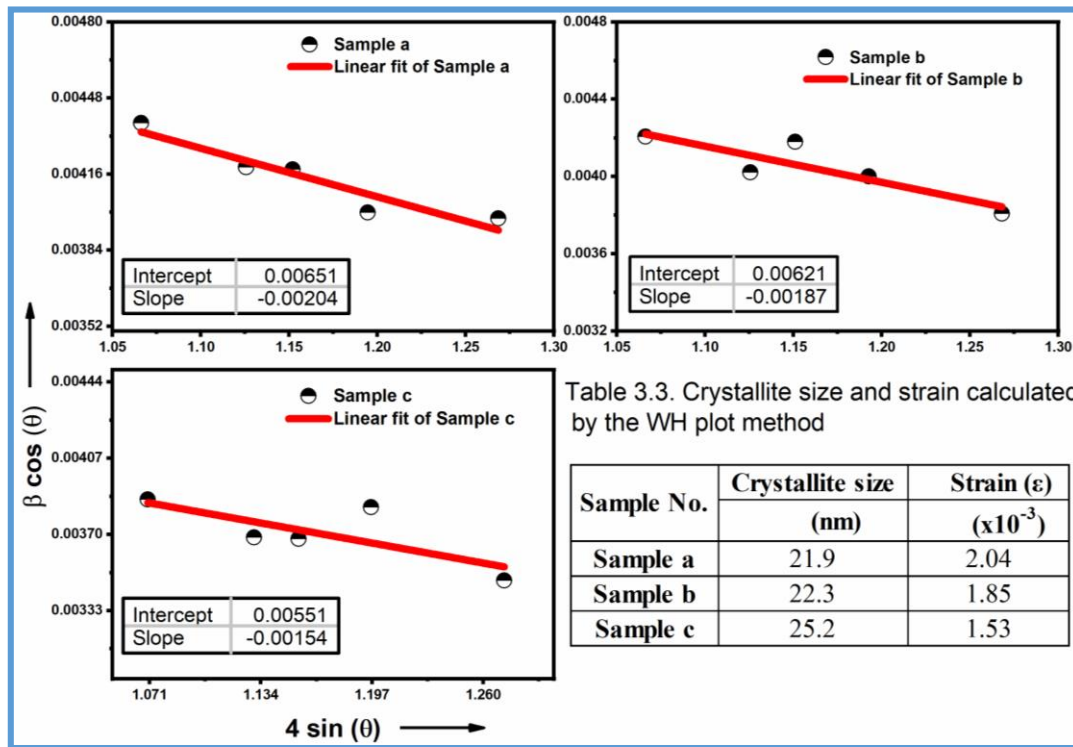


Figure 3.3: WH plot of Ag₂Se samples.

The crystallite size has been calculated for Ag₂Se samples using the WH plot and the values have been reported in table 3.3. The size calculated from the WH and the Scherrer method differ by approximately 10 nm. This difference arises because the

particle size calculated by the Scherrer formula, *i.e.* FWHM, contains a contribution from the strain of the material. The negative slope gives compressive strain within the material. The strain present in samples has been detected to decrease with an increase in the crystallite size. The dislocation density (δ) of material may be defined as “the length of dislocation lines per unit volume of the crystal” [199]. The δ has been calculated using the equation (2.6). The dislocation density has been noticed to decrease from the sample a to c (table 3.2). This decrease in average dislocation density from sample a to sample c might on account of a rise in the crystallite size.

3.3 Synthesis and characterization of Ag₂Se QDs

3.3.1 Experimental details

All the chemicals have been obtained from Alfa Aesar and used as received. Here, the precursors have been changed and again the co-precipitation route has been used for the synthesis of Ag₂Se samples. Three samples have been synthesized and named as sample 1, sample 2 and sample 3. Sample 1 has been prepared by adding the required amount of AgNO₃ powder in 20 ml of double DW. The solution has been mixed continuously until all the AgNO₃ powder dissolves completely. Then, the required amount of selenium powder and H.D. solution (Molar ratio (MR) of AgNO₃/H.D. equal to 0.5 M) has been put into the solution. The solution has been agitated continuously for 80 minutes at 70 °C with a slight variation in temperature *i.e.* ± 2 . The pH of the solution has been kept at 9 by adding NH₄OH solution. The ppt have been formed inside the solution. The solution is then kept to cool down to achieve the room temperature. Thereafter, ppt have been washed with DW two to three times. For structural characterization, the precipitates have been dried at 40°C and crash uniformly to form a fine powder. Similarly, sample 2 and sample 3 has been prepared with a change in the pH of the solution to 11 and 12 by ammonia solution respectively.

Another synthesis route *i.e.* hydrothermal approach has been employed for the synthesis of Ag₂Se sample named as sample 4. In this approach desired amount of silver nitrate, selenium powder and H.D. (MR of AgNO₃/H.D. equal to 0.09 M) have been placed in a beaker which is filled with 12 mL DW. The solution has been stirred for 5 minutes to mix the different precursors used. Then, the solution has been put into the hydrothermal reactor. The hydrothermal reactor has been positioned inside the furnace

and temperature maintained at 70 °C for 48 h. After this, the solution is then kept to cool down to achieve the room temperature. The dark coloured ppt have been obtained by centrifuging the solution at 4000 rpm for 15 minutes. The dark coloured ppt have been crushed uniformly to form a fine powder. This fine powder has been used for further characterization.

3.3.2 Structural properties

EDX spectrum has been utilized to obtain the elemental analysis of different samples (figure 3.4). The silver and selenium peaks present in all the samples have indicated that all the samples comprise of silver and selenium elements [200].

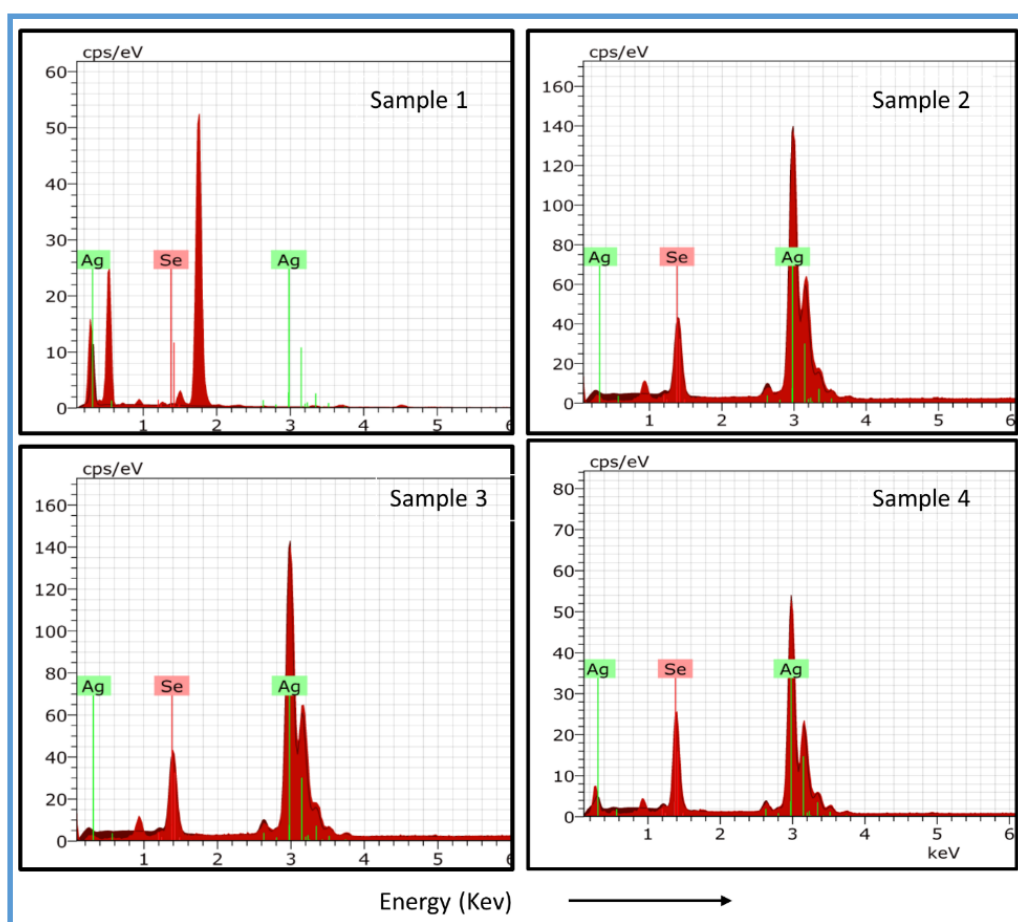


Figure 3.4: EDX spectra of different Ag₂Se samples.

The morphology of Ag₂Se samples has been shown in figure 3.5. The TEM image of sample 1 has shown both spherical and non-spherical shapes in a zig-zag chain but, spherical shapes are more prevalent [201].

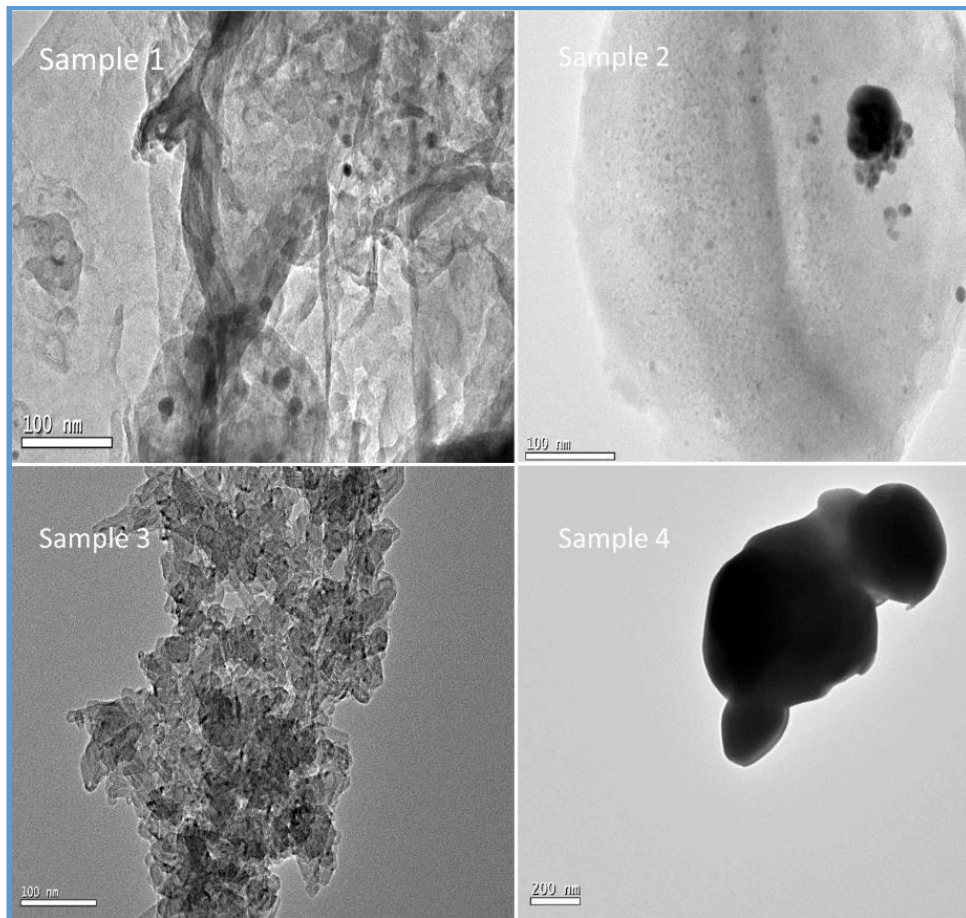


Figure 3.5: TEM images of Ag_2Se samples.

For sample 2, TEM image has indicated undecorated along with clumped nanocrystals. For sample 3, TEM image has indicated QW type assembly which are clumped with each other. This type of image has also been observed in carbon nanotubes [189]. In this image two dimensions *i.e.* height and breadth have fallen in localized dimensions and produces weak quantum confinement effects. The length of quantum wire has fallen in delocalized dimension. A TEM image of sample 4 has shown a bulk structured material. The size of nanocrystals from TEM pictures are computed by employing Image J software system (figure 3.6). The image J software has been used to calculate the size of individual NCs. The histogram plots of TEM images have been shown in figure 3.6. The size of NCs for sample 1 and 2 has been computed by taking the spherical shape of NCs. The size of sample 3 has been computed by selecting the length of the QW. The size and other parameters have been calculated by the Gauss fit of histogram plots (table 3.4).

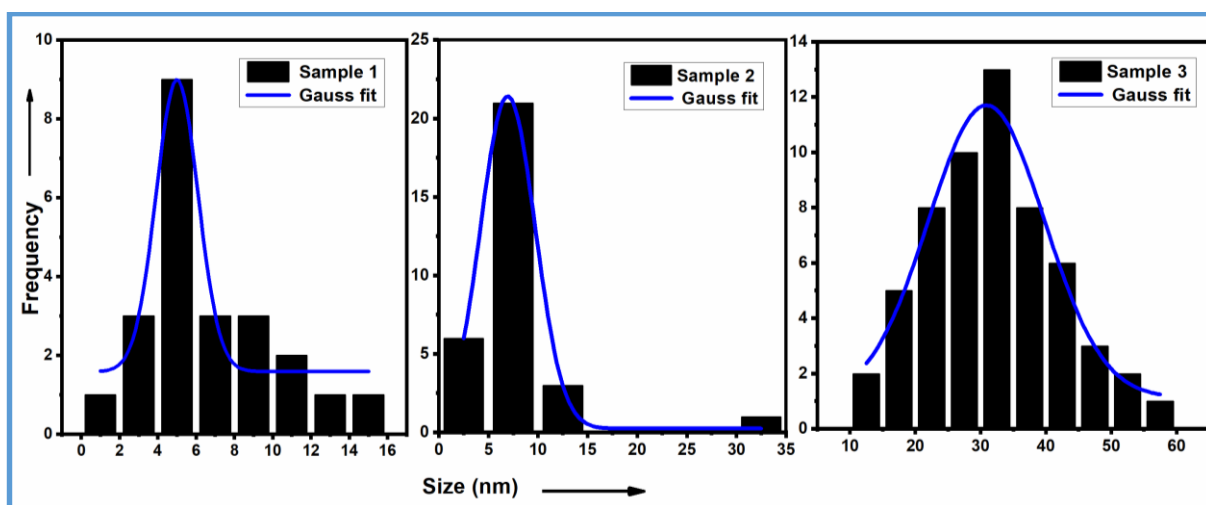


Figure 3.6: Histogram plots of Ag₂Se samples.

The NCs of sample 1 and sample 2 are smaller in size as compared to other samples (table 3.4). Sample 1 and sample 2 have shown the formation of Ag₂Se QDs because the size of samples lies in quantum confinement regime (table 3.4). The increase in the size of NCs from sample 1 to 3 is because of the rise in the potential of hydrogen in the solution. The rise in the potential of hydrogen in the solution will decrease the hydronium ions concentration in the solution. This decrease in the concentration of hydronium ion is responsible for the increase in hydrazine hydrate ions and that reduces the selenium powder to selenium ions making them easily available to form Ag₂Se.

The size of sample 4 has been detected to be the largest in comparison to the rest of the samples. This may be because of the hydrothermal technique used for the synthesis of Ag₂Se sample. In this technique, the longer synthesis time may be responsible for the increased growth of nanocrystals (Ostwald ripening). The second factor responsible for the increased size of nanoparticles may be the MR of AgNO₃/H.D. As the molar ratio of AgNO₃/H.D. decreases the number of H.D. molecules increases which leads to the increase in reduction of selenium to selenium ion and making them easily available for the formation of bulk Ag₂Se.

3.3.3 Optical properties

The absorption spectrum of Ag_2Se samples in the range 200 nm – 1100 nm acquired using UV-VIS-NIR spectrophotometer and has been shown in Figure 3.7. The samples have no clear exciton peak observed in absorbance spectra may due to size/shape inhomogeneity or specific electronic properties of the material [186].

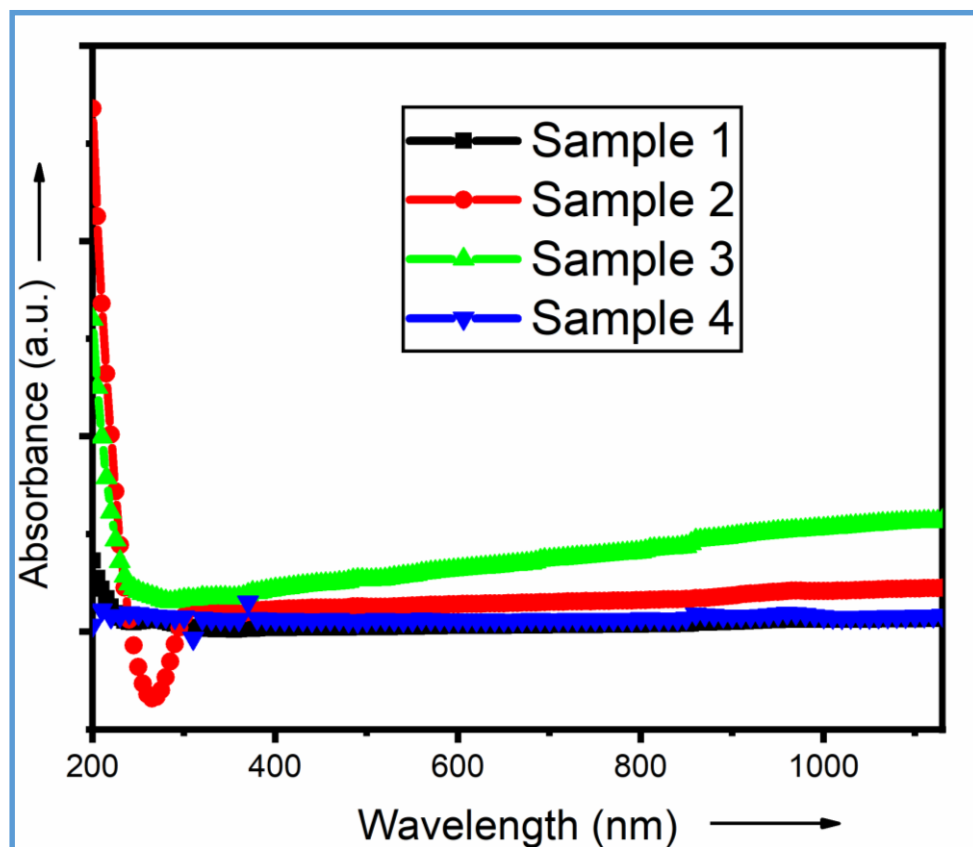


Figure 3.7: Absorption spectra of Ag_2Se material.

The bandgap of the Ag_2Se materials is observed by using the Tauc plot. An absorption coefficient (α) has been computed from equation (2.8). The equation (2.7) has been used to compute the bandgap of NCs using Tauc Plot. The optical bandgap has been predicted by increasing the linear portion length in the graph formed between $(\alpha h\nu)^2$ versus $h\nu$ which intersects the flat axis at any point [202]. This point of intersection gives the value of bandgap for the QDs (figure 3.8).

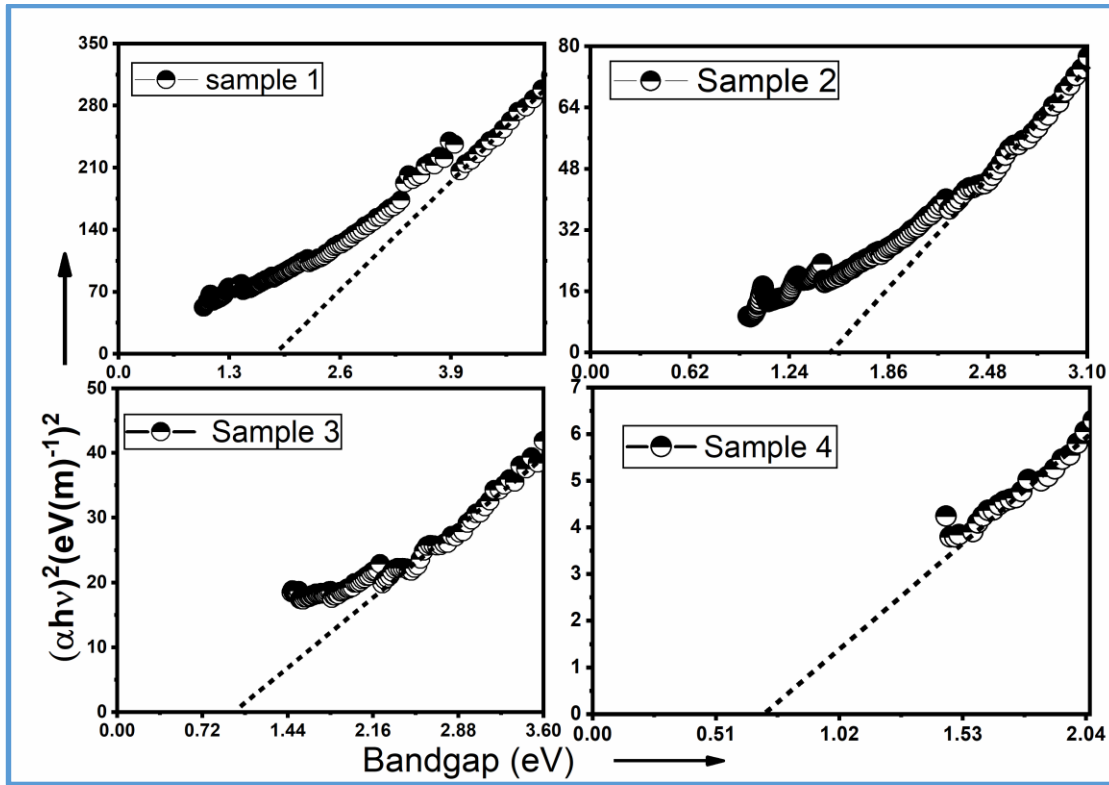


Figure 3.8: Tauc plot of Ag₂Se material.

Table 3.4: The various parameters calculated by TEM images and UV-VIS-NIR spectroscopy for Ag₂Se samples.

Name of samples	Size by TEM	Bandgap
	(nm)	(eV)
Sample 1	5	1.80
Sample 2	6.9	1.50
Sample 3	31.6	0.99
Sample 4	400	0.69

The values of bandgap obtained from figure 3.8 have been given in table 3.4. The maximum value of bandgap has been found for sample 1 and is due to the small crystallite size of Ag₂Se nanocrystals [44]. This has been observed due to the quantization of charges in localized space which has formed a number of discrete states below the conduction band and above the valence band. The formation of these discrete

states has increased the effective band gap of Ag₂Se nanocrystals [203]. The discreteness in the optical bandgap below the conduction band and above the valence band can form more than one electron-hole pair owning large binding energy for single photon incidence [9]. The bandgap of sample 2 is 1.5 eV and that indicates a slight decrease (0.3 eV) as compared to sample 1. This is due to the enhancement in the size of Ag₂Se NCs as evident from TEM images. Similarly, sample 3 and sample 4 have shown a decrease in bandgap because more than one dimensions of materials are in out of quantum confinement regime.

3.4 Conclusion

The co-precipitation and hydrothermal techniques have been used for the optimization of conditions for the synthesis of Ag₂Se QDs. The Ag₂Se samples have been synthesized by changing pH, MR and synthesis methods. The Ag₂Se QDs have been synthesized by co-precipitation approach by optimization of different parameters. The samples of Ag₂Se have been prepared by varying the ratio of AgCl /2-MPA, Na₂SeO₃/H.D. and varying the pH. The orthorhombic phase of the nanoparticles has been confirmed by XRD. The crystallite size of samples has been calculated using the Scherrer and WH plot method. The change in pH of the solution from 13 to 11 at a constant molar ratio of AgCl/2-MPA and Na₂SeO₃/H.D. leads to the formation of larger size Ag₂Se nanoparticles (> 10 nm). The change in the MR of AgCl/2-MPA and Na₂SeO₃/H.D. at constant pH of the solution also leads to the formation of larger size Ag₂Se nanoparticles (> 10 nm). Therefore, the initial precursors have been changed from AgCl to AgNO₃, Na₂SeO₃ to Se powder and in addition to this H.D. has been used both as capping agent as well as reducing agent. The temperature of the solution has also been changed from 75 °C to 70 °C. The presence of silver and selenium elements in Ag₂Se have been confirmed from EDX spectra. TEM images have been used to calculate the size and nature of nanocrystals. The band gap of QDs has been determined using the Tauc's plot. It has been observed that the nanocrystals' size varies from 5 nm to 31.6 nm with the change in pH of the solution at a constant molar ratio of Se/H.D. QDs have been formed for the lowest value of pH of the solution close to 9. The band gap has decreased with the increase in size of material. The hydrothermal approach has also been explored for the synthesis of Ag₂Se NCs. The MR of AgNO₃/H.D. has been

kept constant at 0.09 M during this synthesis. The final product obtained resulted in crystallites of large size of approximately 400 nm. So, the synthesis by the hydrothermal approach has been found to be unsuitable in comparison to the co-precipitation approach. In view of these results, the co-precipitation technique has been employed for the synthesis of silver chalcogenide QDs with the initial precursors AgNO₃, elemental Se or S, H.D. and ammonia (to regulate the pH).

CHAPTER- 4 *

“Structural, morphological and optical properties of co-precipitated Ag₂S QDs”

* **S. Chand**, E. Sharma, and P. Sharma, *Phase change induced quantization in NIR emitting Ag₂S nanocrystals: Structural and optical response for solar energy applications*, **Journal of Alloys and Compounds**, vol. 770, pp. 1173–1180, 2019”.

This chapter deals with the structural, optical and morphological properties of co-precipitated Ag₂S QDs. The chapter has been sectioned into four segments. The first segment includes the introduction of Ag₂S QDs, the second segment describes the synthesis of different sized Ag₂S QDs and their characterization, segment three reports the results obtained from X-ray diffraction, UV-VIS-NIR absorption spectroscopy, Raman spectroscopy and TEM for structural, optical properties and morphology of samples. The results have also been discussed in segment three. The fourth segment of the chapter concludes the results of Ag₂S QDs.

4.1 Introduction

CdX and PbX (X= S, Se, Te) are the most extensively studied semiconductor nanocrystals. These QDs have shown emission and absorption in visible and near IR region but, possess high toxicity because of the presence of lead (Pb) and cadmium (Cd) elements. These elements in QDs should be replaced by less toxic elements and with enhanced properties. Ag₂S QDs having low toxicity and may be a suitable alternative to CdX and PbX based QDs. The emission of Ag₂S QDs in visible or NIR region depends upon the size of QDs [204]. Ag₂S is a direct bandgap material comprises a narrow range *i.e.* 1.1- 0.9 eV [205]. It is advantageous in photovoltaics to transform solar energy into electrical energy [206]–[209]. Ag₂S can also be used in various fields like memory devices, biological diagnosis, IR detectors, electronics, *etc.* [41][43].

Ag₂S is a member of the Ag₂X (X= S, Se, Te) family and exists in three phases. The first phase is acanthite (α -Ag₂S) and this form below (100-170) °C (low-temperature). This phase has a monoclinic crystal structure [210]. The second phase is argentite (β -Ag₂S) and this forms above (100-170) °C but below 587 °C (medium-temperature). This phase has a cubic crystal structure and possesses superionic conductivity [211]–[213]. The third phase is face-centred cubic (γ -Ag₂S) and this forms above 587 °C (high-temperature) [214]. The electrical and optical properties of the Ag₂S NCs have been tuned by way of the size of the material becomes less than twice or thrice of Bohr's radius due to non-periodic alternation in the structure of material [215]. The nanocrystals synthesis by the bottom-up approach has been initially coined up by Bawendi and coworkers [216]. Ag₂S QDs formed in organic solutions depend

upon the medium of the solution, time of stirring, pH of the solution, nature of the ligands, temperature, etc. [217].

The synthesis of different sized Ag₂S QDs by changing the time involved to develop the NCs has been reported here. The precursor materials, pH, amount of capping agent and temperature of the solution have been kept constant during the synthesis process for all the samples. The structural, optical and morphological characterization of Ag₂S QDs have been performed.

4.2 Experimental details

Co-precipitation approach has been used to synthesize Ag₂S QDs which has been explained in detail in chapter 2. All the initial precursor are of high purity-like silver nitrate with purity 99.99%, sulfur powder (S) with purity 99.99%, 3-mercaptopropionic acid (3-MPA) with purity 99%, oleic acid with purity (98%) have been purchased from Alfa Aesar and used as received. Toulene and ammonium solution (35%) (Merck) have been used as received. Four samples of Ag₂S material have been synthesized and named as sample 1, sample 2, sample 3 and sample 4. Synthesis of samples requires the preparation of two solutions X & Y.

For the synthesis of sample 1, the solution X has been made by adding the 1 g of silver nitrate powder in 20 mL of double DW. The solution has been stirred continuously until silver nitrate completely dissolves. Then, the capping agents OA and 3-MPA have been added to the solution X according to the molar ratio AgNO₃/OA and AgNO₃/3-MPA *i.e.* 0.4 M and 0.3 M respectively with continuous stirring.

Solution Y has been made by adding 0.094 g of fine sulphur powder in toluene. Solution Y has been heated and stirred until sulphur powder dissolves completely. Then, solution Y has been added slowly to the solution X with continuous stirring at a temperature of approximately 75 °C ± 2 °C. During the stirring, the pH of the solution has been maintained equal to 7 by using NH₄OH solution. The mixed solution has been heated and stirred continuously at a temperature of 80 °C ± 2 °C for 5 minutes. Then, the solution has been quenched in water to attain room temperature quickly. To remove the excess of capping agents, the solution has been centrifuged and the precipitates have been washed with DW three times [218], [219]. For structural characterization, the ppt have been dried below 45 °C and powdered uniformly employing a mortar-pestle.

Similarly, the other three samples have been synthesized by varying the synthesis time as 10 minutes, 15 minutes and 60 minutes respectively.

4.3 Results and discussion

4.3.1 Structural properties

X-ray diffractograms of sample 1, sample 2, sample 3 and sample 4 in the range 2θ from 10° to 50° have been shown in figure 4.1. XRD pattern for sample 1 reveals that the peaks are matching with the one given in the JCPDS card no 24-0715. The JCPDS card no 24-0715 has represented the monoclinic phase of Ag_2S . For the other three samples, the figure shows the formation of mixed phases of cubic and monoclinic phases of Ag_2S confirmed from JCPDS card no 02-0998 and 24-0715.

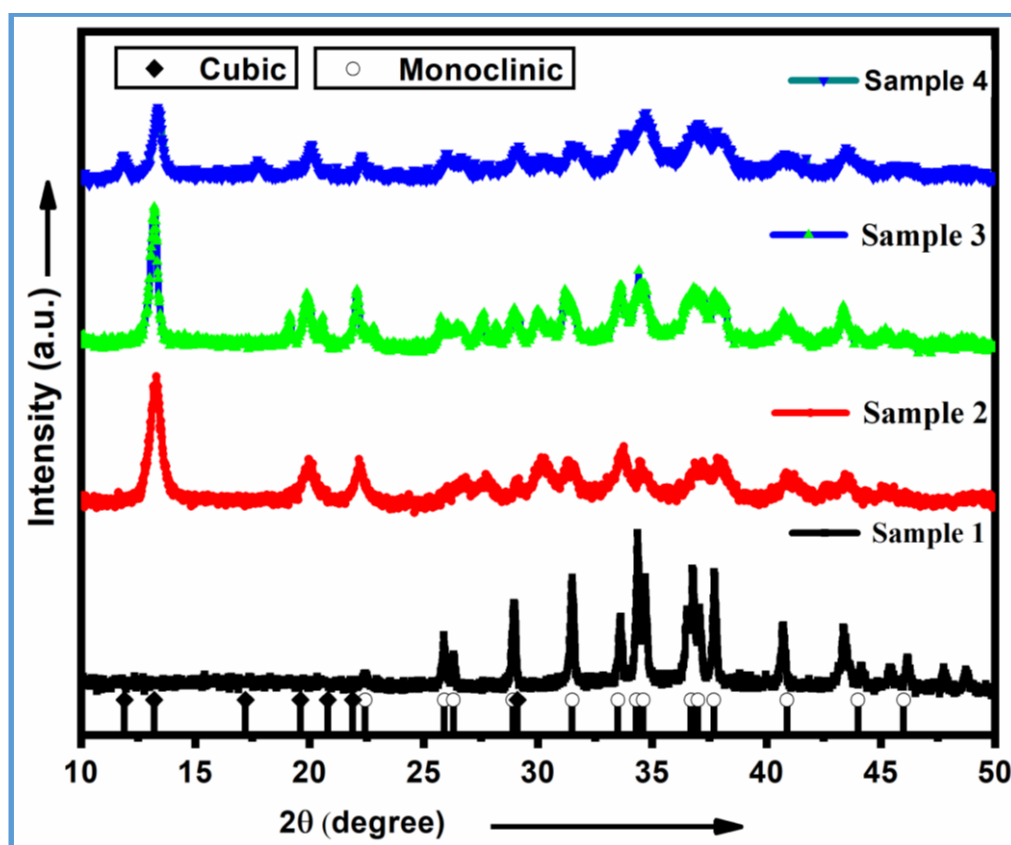


Figure 4.1: XRD patterns of different Ag_2S nanocrystals.

This has been described by various researchers that $\beta\text{-Ag}_2\text{S}$ occurs in between temperature range 443 K to 860 K [220]. The mixed monoclinic and cubic phases of Ag_2S material have been reported by researchers under high-pressure synthesis

conditions at a lower temperature < 443 K [221], [222]. In present work, we have been obtained mixed phases α -Ag₂S and β -Ag₂S at synthesis temperature 353 K with varying the synthesis time for all the samples.

4.3.2 Morphology of QDs

The morphology of Ag₂S samples has been studied using TEM (Figure 4.2). The TEM image of sample 1 has shown a mixed configuration (spherical, non-spherical) of NCs with stacking compactly. The Ag₂S nanocrystals have been found aggregated. Similarly, TEM images of other samples have shown a large number of aggregated NCs. The aggregation of NCs may be due to the use of high concentration of NCs during TEM characterization. TEM images are not able to detect clearly distinct lattice planes as depicted by XRD patterns may be due to the small size of NCs.

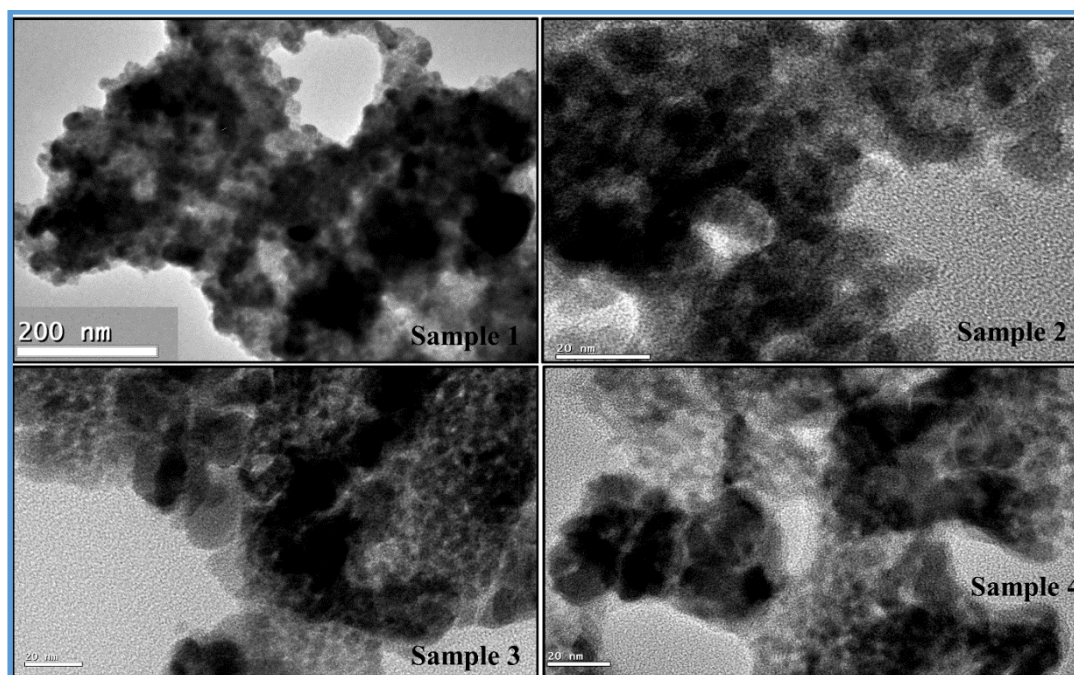


Figure 4.2: TEM images of Ag₂S samples.

The image J software has been used to calculate the size of Ag₂S nanocrystals from TEM images (figure 4.3). The size and other parameters have been calculated by the Gauss fit of histogram plots. Size and dispersion of NCs for different samples have been given in table 4.1. Sample 1 has been found in polydispersed nature whereas other samples have described mostly the monodisperse nature. The size of nanoparticles in

sample 1 is higher than other samples (table 4.1). The size of NCs has increased from sample 2 to sample 4. This enhancement in the size of NCs may be owing to the increase in the diffusion of monomers with the extension in synthesis time. The decrease in size of nanoparticles from sample 1 to sample 2 is large (approximately 20.3 nm) as compared to the increase in the size of NCs from sample 2 to sample 4 (approximately 1.1 nm). This large decrease in size of nanoparticles from sample 1 to sample 2 is due to the emergence of an additional phase (β -Ag₂S). All the samples except sample 1 have shown size less than 5 nm due to the presence of mixed phases and results in the origination of quantum confinements.

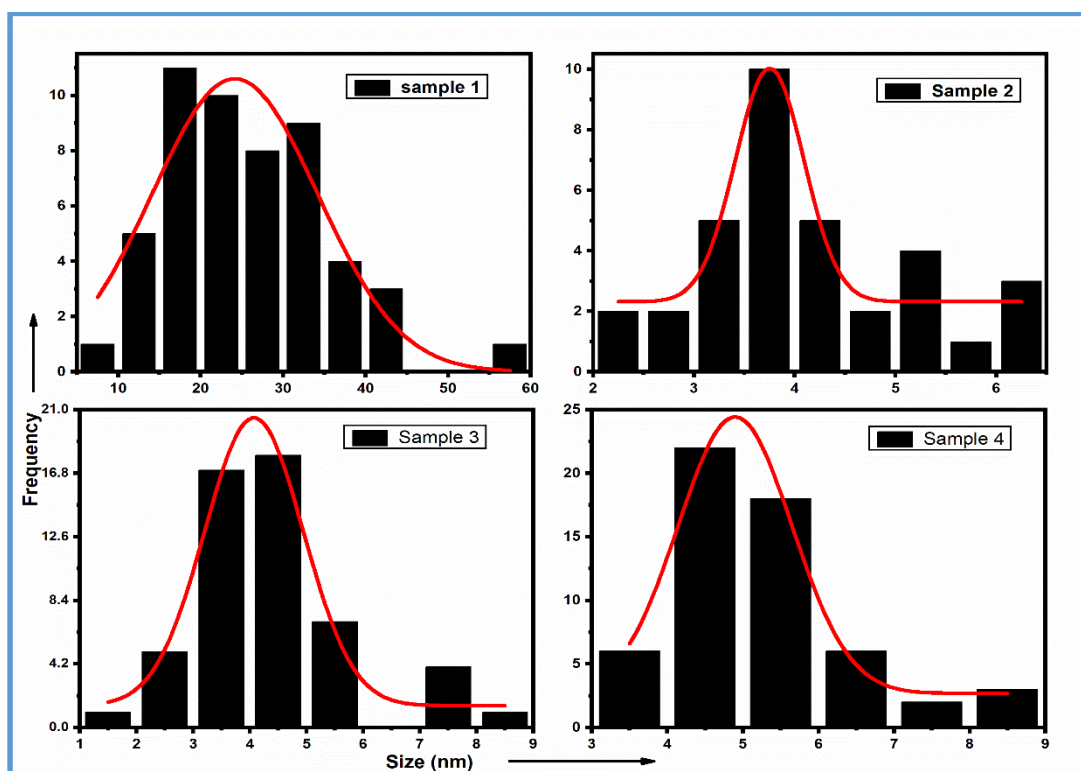


Figure 4.3: Histogram of Ag₂S samples with Gaussian fit.

The interplanar spacing of the nanocrystals for sample 3 has been found with the help of the HRTEM image (Figure 4.4 (a)). Figure 4.4 (b) of sample 3 has indicated the interplanar spacing equal to 0.25 nm by inverse fast Fourier transform. This value of interplanar spacing calculated from HRTEM image has shown a fair match with the interplanar separation found from XRD.

Table 4.1: Various parameters have been calculated from TEM and UV-VIS-NIR spectroscopy.

Name of samples	First exciton peak (nm)	Size from Brus equation (nm)	Size by TEM (nm)	Polydispersity (%)
Sample 1	1155	----	24.1 ± 10	42
Sample 2	796	3.1	3.7 ± 0.34	9
Sample 3	895	3.7	4.0 ± 0.86	22
Sample 4	947	4.2	4.8 ± 0.75	16

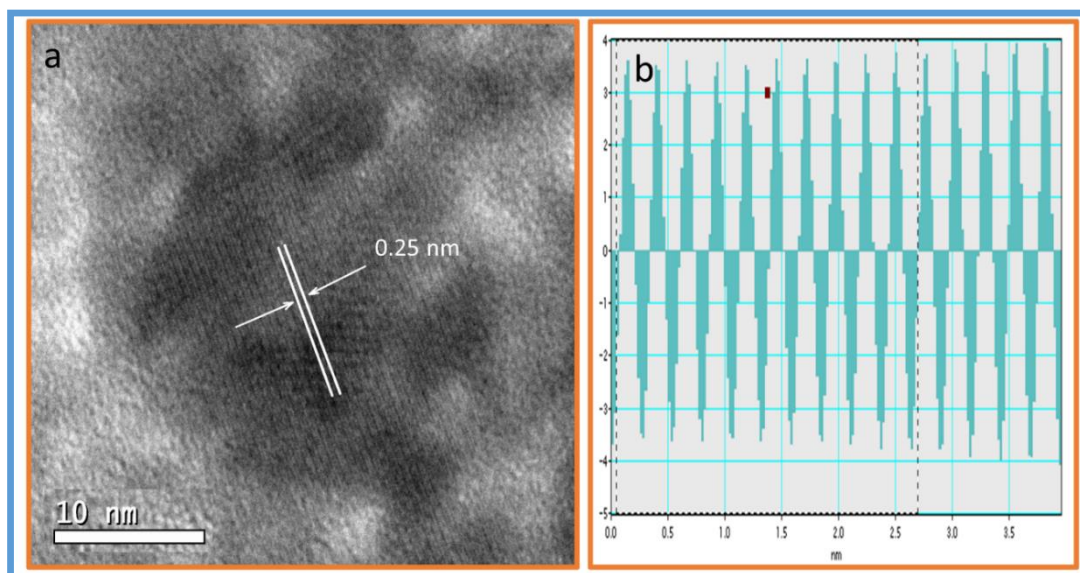


Figure 4.4: (a) The high-resolution TEM image, and (b) inverse fast Fourier transform configuration of sample 3 Ag₂S QDs.

4.3.3 Optical properties

Absorbance and Raman spectroscopy have been used to analyze the optical properties of different Ag₂S samples.

4.3.3.1 UV-VIS-NIR spectroscopy

This spectroscopy has been used to find the absorption spectrum of Ag₂S samples (figure 4.5). In absorbance spectra of sample 1, a peak (first absorption peak)

has been found at 1155 nm (inset of figure 4.5). This peak has resembled with the bulk bandgap of the Ag_2S [223], [224]. The first absorption peak of sample 2 has shown a blue shift as compared to sample 1. This blue shift may be due to the occurrence of quantum confinement in sample 2.

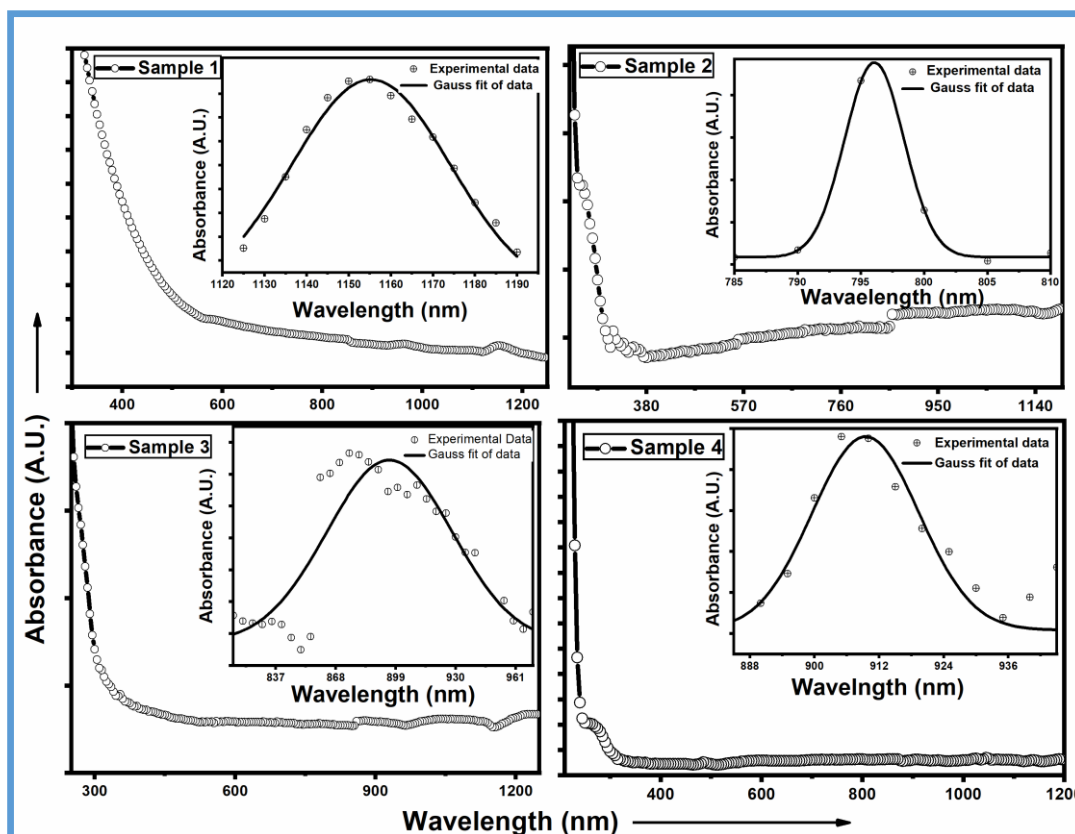


Figure 4.5: UV-VIS-NIR absorption spectra of various Ag_2S samples.

The first absorption peak of sample 3 and sample 4 has shown redshift with respect to sample 2. This behaviour has indicated that the quantum confinement decreases from sample 2 to sample 4. Brus equation (2.10) has also been used to calculate the size of QDs [15]. The bandgap (E_g^{nano}) of NCs has been calculated using the equation (2.9). In equation (2.9), λ is the wavelength corresponding to the first exciton peak in different samples. The size of QDs and first exciton peak of all the samples have been given in table 4.1. The size of nanoparticles in sample 1 has not been investigated using the Brus equation because the size of sample 1 has been observed to be out of the confinement regime. The size of QDs calculated by Brus equation has

shown an increasing trend from sample 2 to sample 4. The similar trend has also been observed for the size of QDs calculated from TEM images.

Griffiths equation (2.11) has been used to calculate the exciton radius of Ag₂S QDs [181]. From the literature, the values of ϵ , m_e^* and m_h^* equal to 8.36, 0.286 m_0 , and 1.096 m_0 respectively for Ag₂S material have been taken [5], [225]. Theoretically, the calculated value of exciton diameter has been found to be 4 nm. Therefore, if the size of NCs is greater than the exciton radius 2 nm but less than $3a_0$ then the NCs has to be considered in the “weak confinement region”. The size of QDs for sample 2 to 4 has been lying in between 2 nm to 5 nm as observed from TEM and Brus equation. This indicated that the sample 2 to sample 4 have belonged to a weak quantum confinement region and hence the quantum properties applicable to the material are weak.

4.3.3.2 Raman spectroscopy

Raman spectra of different Ag₂S nanocrystals have been shown in figure 4.6. Raman broadband for sample 1 has been observed at 243 cm^{-1} indicates the existence of α -Ag₂S (inset of figure 4.6) [226]. This Raman band observed at 243 cm^{-1} indicates the presence of asymmetric bending and stretching of Ag–S–Ag. The monoclinic structure of Ag₂S has been made up of two modes A_g and B_g. A_g mode corresponds to the vibrations of the Ag atoms and B_g mode corresponds to the vibrations of the S atoms. The B_g mode has represented the distorted body-centred cubic (bcc) configuration of S atoms in α -Ag₂S material. The B_g mode remains the same in bulk as well as nanocrystalline Ag₂S material. The A_g mode has been further divided into A_{g1} and A_{g2} modes. In A_{g1} mode, Ag atoms have occupied tetrahedral sites in a bcc configuration of the surrounding of S atoms. In A_{g2} mode, Ag atoms have occupied octahedral sites in a bcc configuration of the surrounding of S atoms. The distorted bcc arrangement of S atoms has remained the same on the phase transformation of α -Ag₂S to β -Ag₂S. So, Ag atoms corresponding to A_{g1} and A_{g2} modes have changed their configuration to achieve the phase change process.

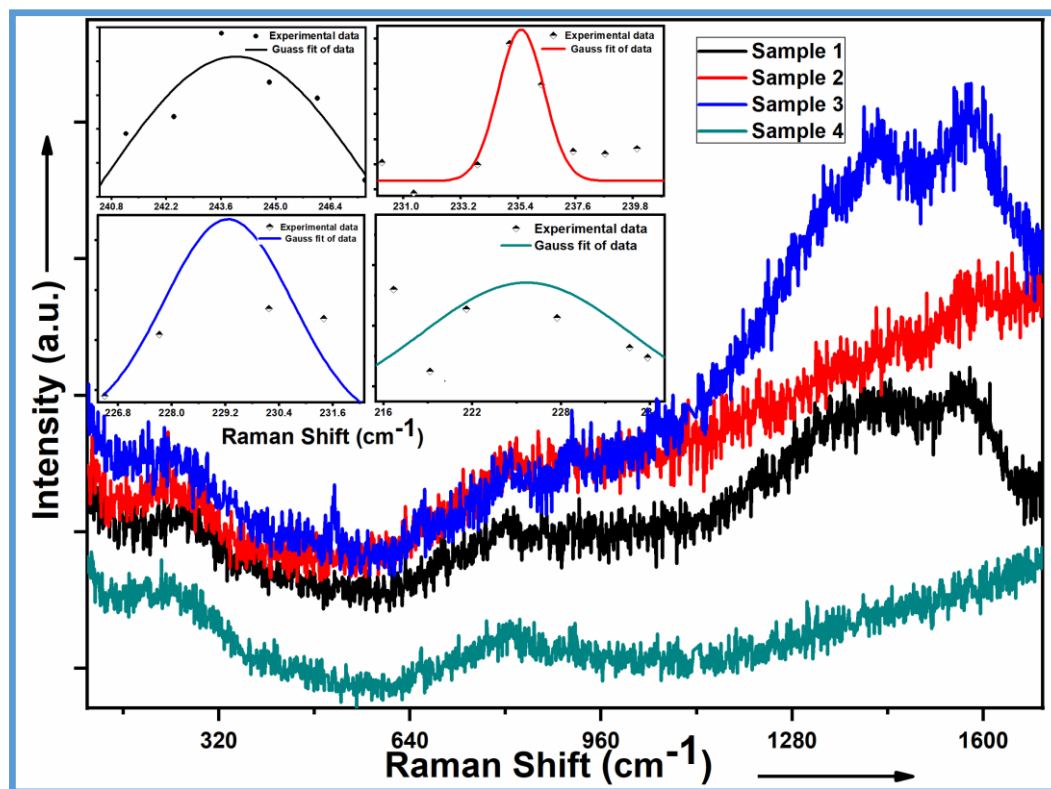


Figure 4.6: Raman spectra of Ag_2S samples.

The $\beta\text{-Ag}_2\text{S}$ phase has been composed of more number of Ag atoms configured in A_{g1} mode as compared to Ag atoms configured in A_{g2} mode [213]. The Raman band for sample 1 to 4 has been found to be shifted from 243 cm^{-1} to 223 cm^{-1} (inset of figure 4.6). This blue shift in the Raman band may be on account of two factors. The first factor depends upon the size of the NCs, *i.e.* with the decrease in the size of the NCs Raman band has shifted towards higher wavenumber [227]. The second factor depends upon the origin of the new $\beta\text{-Ag}_2\text{S}$ phase [228]. For Raman shift towards lower wavenumber from sample 1 to 2, the second factor has a more dominant effect; whereas for sample 2 to 4 the first factor has been predominant. The Raman band at 310 cm^{-1} has been found due to phonon density states [229]. The Raman bands at 808 cm^{-1} , 1410 cm^{-1} , and 1560 cm^{-1} have been observed due to CO_3 out of plane bending for Ag_2CO_3 molecules, CH_3 symmetric bending of $\text{AgC}_2\text{H}_3\text{O}_2$ molecules and O-C-O symmetric stretching of $\text{AgC}_2\text{H}_3\text{O}_2$ molecules respectively [226]. These peaks have indicated that OA presents on the surface of QDs and has been linked to the Ag atoms.

4.4 Conclusion

Ag₂S QDs have been synthesized by varying the synthesis time with co-precipitation approach. The size of QDs calculated from the histogram plot of TEM images has shown a good match with the size calculated from Brus equation. Quantum confinement has been observed in the Ag₂S samples due to the formation of β -Ag₂S phase which has been confirmed from XRD spectra. The quantum confinement has also been confirmed by the absorption spectra of Ag₂S QDs. The blue shift in wavelength has been observed with a decrease in size. The transformation of α -Ag₂S to β -Ag₂S phase has also been confirmed by Raman spectra. Raman spectra have also provided information about different groups present on the surface of QDs. The quantum confinement behaviour of QDs may be utilized to harvest energy in the IR and visible region of the electromagnetic spectrum.

CHAPTER- 5 *

Structural, morphological and optical properties of co-precipitated alloyed $\text{Ag}_2\text{Se}_x\text{S}_{1-x}$ QDs

* “**Subhash Chand**, A. Dahshan, N. Thakur, V. Sharma, Pankaj Sharma, *Alloyed $\text{Ag}_2\text{Se}_x\text{S}_{1-x}$ quantum dots with red to NIR shift: the band gap tuning with dopant content for energy harvesting applications* (2019) (**Communicated to SCI, Scopus Indexed Journal**).

With the advancement of technology, the size of devices decreases which results in several prominent factors. These factors mainly include quantum mechanical effects and statistical mechanical effects. The decrease in the dimensions of the equipment results in boosting the efficiency of energy consumption and also uses less area of the device. In quantum mechanical effect, the electronic and optical properties of materials have been changed dramatically as the size reduces below a certain limit. This chapter includes the synthesis of selenium alloyed Ag_2S QDs. The chapter has been sectioned into four segments. The first segment includes the introduction of alloyed Ag_2S QDs, the second segment describes the synthesis of different sized selenium alloyed Ag_2S QDs and their characterization, segment three reports the results obtained from X-ray diffraction, UV-VIS-NIR absorption spectroscopy, Raman spectroscopy and TEM for structural, optical properties and morphology of samples. The results have also been discussed in segment three. The fourth segment of the chapter concludes the results of selenium alloyed Ag_2S QDs.

5.1 Introduction

The various structural changes are taking place in materials with the addition of dopant/impurities or alloying. The alloying or doping at nanocrystal level has improved the advancement of semiconductor-based technologies. In electronic impurity doping, impurity atoms are injected into the electronic levels of semiconductor at equilibrium. The impurity atoms in nanocrystals have formed narrow donor level or acceptor levels in between the bandgap of the material. This inclusion of donor or acceptor level slightly shifts the Fermi level of the material. The band gap of material deforms due to the formation of tail states below LUMO and above HOMO which leads to the distortions in the crystal structure [230]. Reliable schemes are not straightway available for a large range of NCs for controlled doping of impurity atoms in the quantum-confined NCs material [231].

Ternary alloyed QDs have some superior properties than binary QDs [232]. Different bandgap materials have been synthesized by controlling the composition of ternary alloyed nanocrystals without considerable change in the particle size.

Researchers have reported that ternary alloyed nanocrystal devices were more efficient than pure binary alloy NCs based devices [233].

Silver-based chalcogenide QDs are preferred because of their low toxicity over the Cd/Pb based chalcogenide QDs [234]. These QDs emits in the visible and NIR region subject to the size and other properties of the material. Ag_2S and Ag_2Se are direct band gap type semiconductors. Selenium alloyed Ag_2S QDs may be used in the area of electronics, memory devices, biological diagnosis, etc. [235]. These may play a useful role in photovoltaics to convert solar energy to electrical energy [236].

In this chapter, a simple intermediate temperature co-precipitation approach has been described for alloying of semiconductor NCs with worthy control over the properties *i.e.* the band gap of the different samples by altering the amount of dopant. Selenium alloyed $\text{Ag}_2\text{Se}_x\text{S}_{1-x}$ QDs have been synthesized by using water as a solvent. Properties of QDs are highly influenced by the precursor materials, the medium used for synthesis, nature of the ligands, time of stirring, temperature, *etc.* The synthesis of different size $\text{Ag}_2\text{Se}_x\text{S}_{1-x}$ QDs has been reported by varying the x value from 0 to 1. The amount of capping agent and temperature of the solution have been kept constant during the synthesis process for all the samples. The structural, morphological and optical characterizations of selenium alloyed $\text{Ag}_2\text{Se}_x\text{S}_{1-x}$ QDs have been performed.

5.2 Experimental details

All the initial precursor *e.g.* silver nitrate with purity 99.99%, selenium powder with purity 99.99%, 3-mercaptopropionic acid with purity (99%) have been obtained from Alfa Aesar and have been used as received. Sulfur powder (S) with purity 99.995% has been obtained from Sigma Aldrich and has been used as received. Hydrazine hydrate (80%), acetone and ethanol have also been used as received (Merck). Selenium alloyed $\text{Ag}_2\text{Se}_x\text{S}_{1-x}$ QDs have been synthesized by co-precipitation approach which has been explained in detail in chapter 2. Four samples of selenium alloyed $\text{Ag}_2\text{Se}_x\text{S}_{1-x}$ QDs have been synthesized and named as S1, S2, S3 and S4. The synthesis of samples requires the preparation of two solutions X & Y.

For the synthesis of S1, solution X has been synthesized by adding the 1.4 g of AgNO_3 powder in 25 mL of double DW. The solution has been stirred continuously until silver nitrate completely dissolves. Then, the solution of capping agents 3-MPA

have been added to the solution X according to the molar ratio $\text{AgNO}_3/3\text{-MPA}$ *i.e.* 0.15 M with continuous stirring. Solution Y has been made by adding the 0.132 g of S powder in hydrazine hydrate. The solution Y has been heated ($75\text{ }^\circ\text{C} \pm 2\text{ }^\circ\text{C}$) and stirred until sulphur powder dissolves completely. After this, the solution Y has been allowed to attain the room temperature. Then, solution Y has been added slowly to the solution X with continuous stirring at a temperature of $50\text{ }^\circ\text{C} \pm 2\text{ }^\circ\text{C}$. The mixed solution has been heated and stirred continuously for 5 minutes at a temperature of $50\text{ }^\circ\text{C} \pm 2\text{ }^\circ\text{C}$ for 5 minutes.

Then, the mixed solution has been quenched in water to attain room temperature quickly. To evolve the QDs ppt, a small amount of ethanol has been added. To remove the excess of capping agents, the solution has been centrifuged and the precipitates have been washed with DW three times. For structural characterization, the ppt have been dried below $45\text{ }^\circ\text{C}$ and powdered uniformly employing a mortar-pestle. Similarly, the other three samples have been synthesized by varying the x mol % in $\text{Ag}_2\text{Se}_x\text{S}_{1-x}$ (x = 0.4, 0.6 and 1.0).

5.3 Results and discussion

5.3.1 Reaction mechanism

The possible reaction mechanism for $\text{Ag}_2\text{Se}_x\text{S}_{1-x}$ has been given in figure 5.1. In solution X, AgNO_3 powder has been decomposed by water molecules into AgOH and NO_3^- molecules. After this, the addition of 3-MPA cap the silver atoms (figure 5.1 (a)). Hydrophobic ends of 3-MPA connect to the Ag atoms and hydrophilic ends remain dispersed in water. For solution Y, sulfur/selenium powder has been added in hydrazine hydrate solution so, that it dissolves completely.

After this solution Y has been added to solution X. Then sulfur/selenium atoms from solution Y has been attached to the silver atoms of solution X. In this process, the entry of sulfur/selenium atoms for the crystallites formation of $\text{Ag}_2\text{Se}_x\text{S}_{1-x}$ (figure 5.1 (b)) depends upon the concentration of capping agents. The uniform crystal growth and other properties of Ag_2S nanocrystals have been disturbed by the introduction of selenium atoms inside the solution.

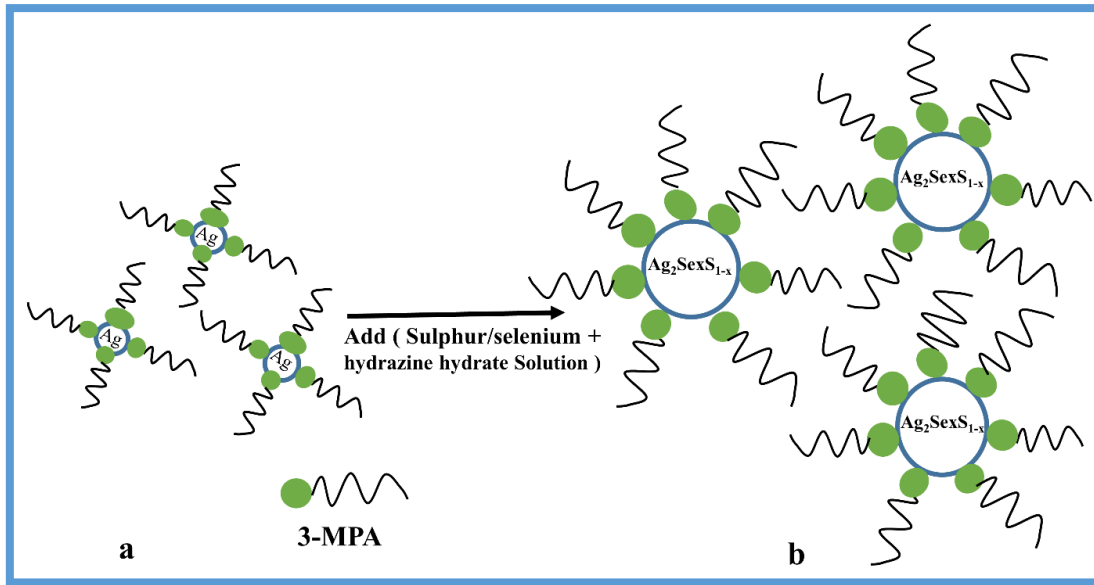


Figure 5.1: Synthesis of $\text{Ag}_2\text{Se}_x\text{S}_{1-x}$ QDs (a) the creation of Ag capped by 3-MPA NCs and (b) the creation of $\text{Ag}_2\text{Se}_x\text{S}_{1-x}$ QDs capped by 3-MPA.

5.3.2 Structural properties

X-ray diffractograms of $\text{Ag}_2\text{Se}_x\text{S}_{1-x}$ nanocrystals in the range 2θ from 20° to 60° have been shown in figure 5.2 (a). For S1, all the peaks in figure 5.2 (a) have resembled with the peaks indexed in the JCPDS card no 24-0715. The JCPDS card no 24-0715 has represented the monoclinic phase of Ag_2S . The peaks of S4 matches with the orthorhombic phase of Ag_2Se (JCPDS card no 24-1041). The samples S2 and S3 reveal that the peaks are lying in between the peaks of monoclinic Ag_2S and orthorhombic Ag_2Se phases. There is a slight shift in the XRD peaks positions for S1 to S4 indicates that the samples are alloyed materials, not core-shell structures (figure 5.2 (a)). The peaks shift (shown in dotted line in figure 5.2 (b)) from S1 to S3 have been found towards the higher angle and for the sample S4, a peak shift has been detected towards the lower angle as compared to S3. This peak shift may depend upon two factors: electronegativity and ionic size. The electronegativity of sulphur and selenium are 2.58 and 2.55 respectively and ionic size of sulphur and selenium are 0.184 nm and 0.198 nm respectively. The peak shift from S1 to S3, the effect of electronegativity of sulfur is more dominant as compared to the ionic size of selenium. This leads to a decrease in the interplanar spacing and which leads to shifting in diffraction angle peaks towards the higher side. In the S4, sulfur is absent. So, electronegativity effect of sulfur vanishes

and ionic size effect dominates which increase some lattice parameters and shift the diffraction peaks towards lower angles (Vegard's Law) [237]. Broad peaks in XRD configuration are due to the small size of NCs.

If the particle size and strain have Cauchy-like behaviour and their influences to the line widening are independent of each other. Then, the crystallite size and strain have been calculated using the Williamson–Hall (W-H) equation (2.5). The Williamson–Hall (W-H) equation has also been known as uniform deformation model because it is considered strain to be alike in every direction of crystals. The values of $\beta\cos\theta$ have been plotted on the ordinate and $4\varepsilon\sin\theta$ on the abscissa. The slope and intercept of the linear fit of the graph have been worked out to calculate the strain and crystallite size (Figure 5.3).

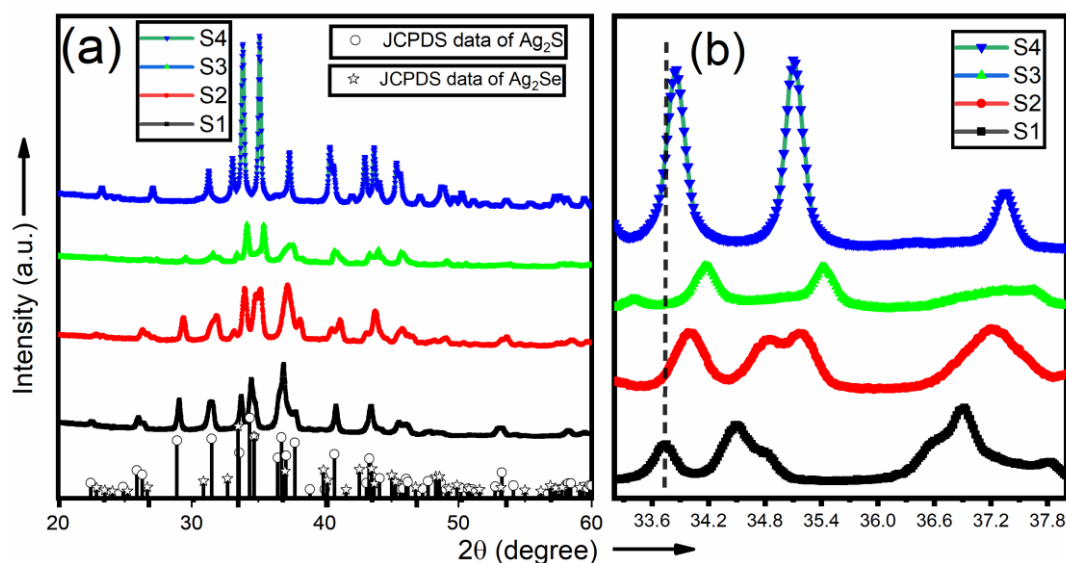


Figure 5.2: (a) XRD configurations of $\text{Ag}_2\text{Se}_x\text{S}_{1-x}$ NCs (b) XRD configurations of most intense peaks.

The crystallite size calculated for $\text{Ag}_2\text{Se}_x\text{S}_{1-x}$ samples from the WH plots has been given in table 5.1. The slope of S1 and S2 is positive due to the tensile strain inside the material (figure 5.3). The negative slope for S3 and S4 is due to the compressive strain inside the material. The dislocation density has been calculated by equation (2.6). The average dislocation density has been found to decrease from the S1 to S4 (table 5.1).

This decrease in average dislocation density may be due to an increase in crystallite size of samples.

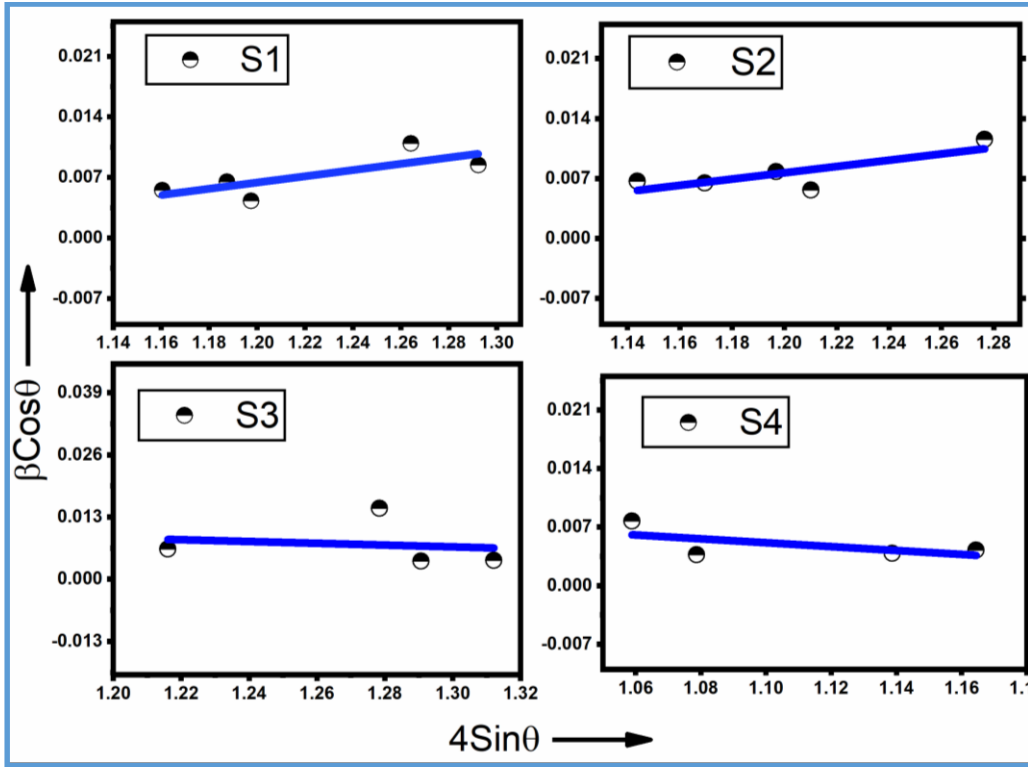


Figure 5.3: Williamson–Hall plot of $\text{Ag}_2\text{Se}_x\text{S}_{1-x}$ nanocrystals.

Table 5.1: Various parameters calculated by the WH PLOT and TEM images of $\text{Ag}_2\text{Se}_x\text{S}_{1-x}$ samples.

Name of samples	Size by WH Plot (D)	Strain	Dislocation density	Size by TEM (Xc)	Polydispersity
	(nm)			(nm)	
S1	3.7	0.03603	0.266858	3.5	32
S2	3.9	0.0367	0.259646	3.8	35
S3	4.5	-0.0187	0.223584	4.2	49
S4	4.6	-0.0232	0.216372	4.8	40

EDX has been performed to find the stoichiometry of different $\text{Ag}_2\text{Se}_x\text{S}_{1-x}$ samples. Stoichiometry for different $\text{Ag}_2\text{Se}_x\text{S}_{1-x}$ samples has been given in table 5.2. The EDX spectra of different samples have been shown in Figure 5.4. This is clear from figure 5.4 that the synthesized samples consist of silver, selenium and sulphur elements. A small deviation from their stoichiometry has been observed in all the samples. This may be due to the small size of Se alloyed $\text{Ag}_2\text{Se}_x\text{S}_{1-x}$ samples [238].

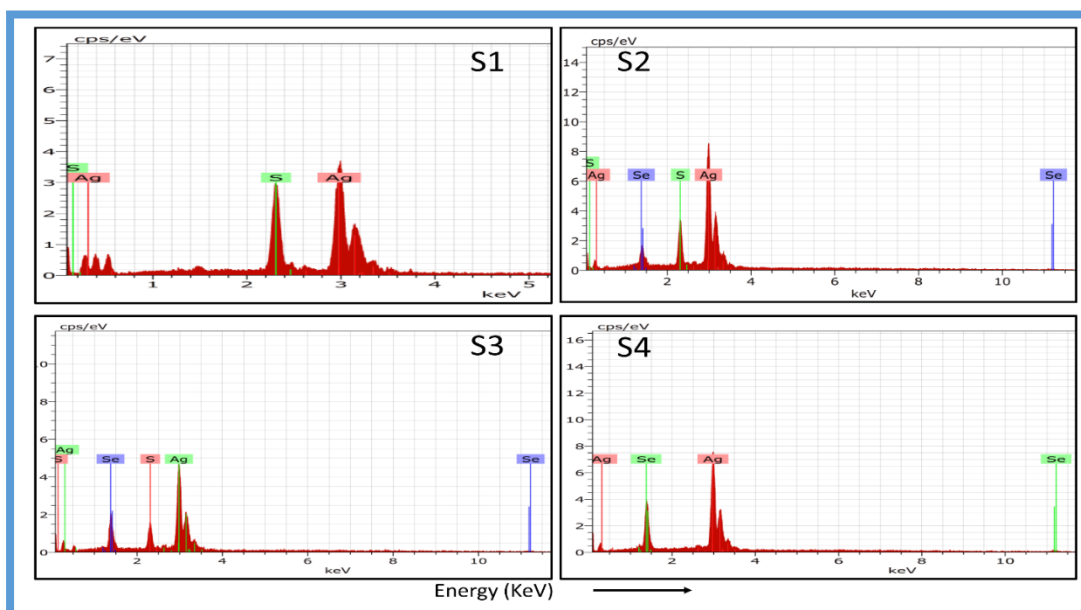


Figure 5.4: EDX spectrum of $\text{Ag}_2\text{Se}_x\text{S}_{1-x}$ nanocrystals.

Table 5.2. Atomic percentage for different elements in $\text{Ag}_2\text{Se}_x\text{S}_{1-x}$ samples.

Atomic %	Silver	Sulfur	Selenium
S1	55.49	44.51	0
S2	66.45	25.5	8.05
S3	61.96	19.71	18.33
S4	70.45	0	29.55

Surface binding of QDs has been analyzed by FTIR spectra (figure 5.5). Peaks present at 3786 cm^{-1} and 3435 cm^{-1} in all the samples are due to the $-\text{NH}$ group. Peaks observed for S1 to S4 at 2825 cm^{-1} - 2990 cm^{-1} are due to the $-\text{CH}_3$ stretching [239]. The $-\text{C}=\text{O}$ stretching of the carboxylic acid group has been designated for the appearance of peaks at 1710 cm^{-1} - 1780 cm^{-1} in S1 to S4 [200]. Peak present at 1080

cm^{-1} in S1 to S4 is due to the acetate group. Broad peak present in S1, S2, and S3 at 3435 cm^{-1} may be due to the $-\text{OH}$ group. The peaks present in S4 between 2316 cm^{-1} - 2344 cm^{-1} is designated to free $-\text{SH}$ group (inset of figure 5.5) [240]. This shows that samples S1 to S3 have been connected by thiol (capping agent) but, S4 has been connected by the carboxylic group (capping agent) on the surface of the nanocrystal.

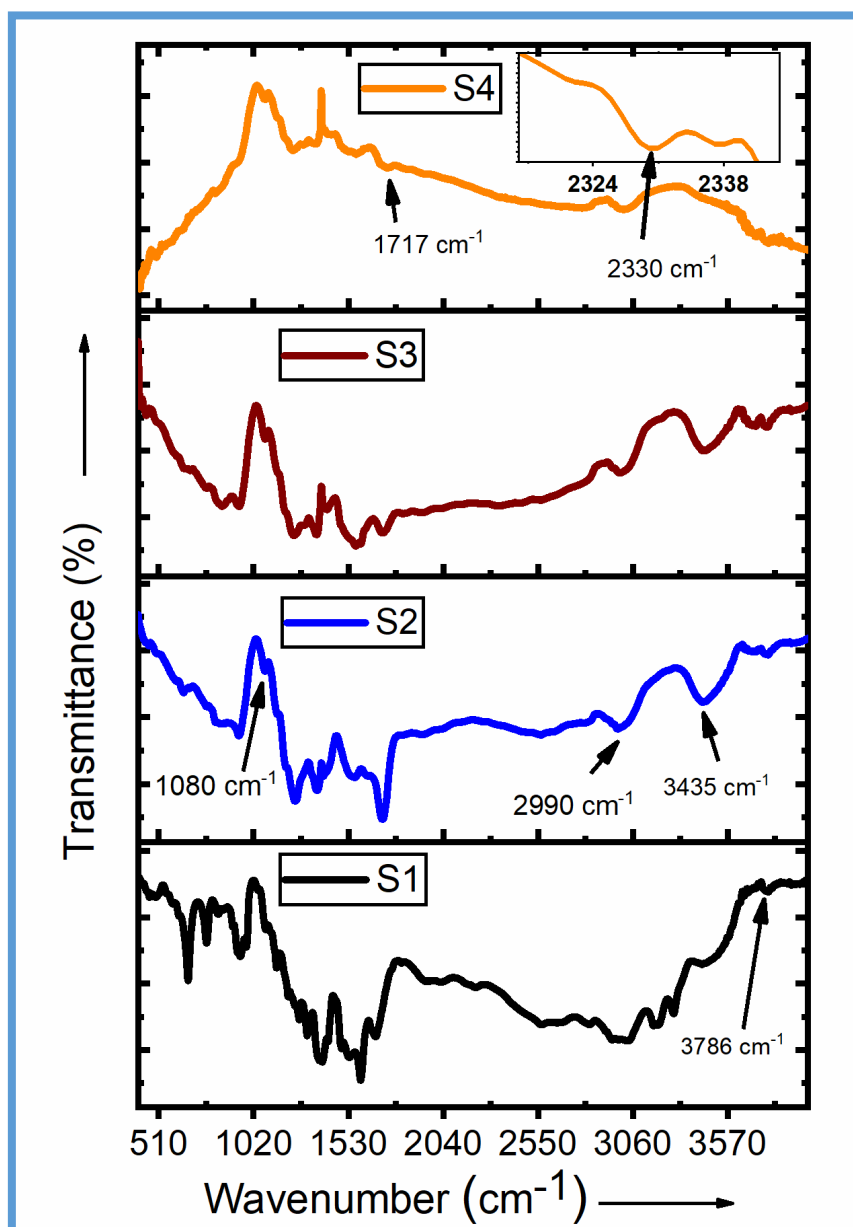


Figure 5.5: FTIR spectrum of different $\text{Ag}_2\text{Se}_x\text{S}_{1-x}$ samples.

This happens due to the increase in the concentration of selenium from S1 to S3 which leads to the decrease in thiol group binding and increases the carboxylic acid group binding to the surface of the nanocrystal.

5.3.3 Morphology of QDs

The morphology of $\text{Ag}_2\text{Se}_x\text{S}_{1-x}$ nanocrystals has been studied by TEM (Figure 5.6). TEM images of all the samples have shown mixed spherical, non-spherical and crystalline structure. The sample S1 illustrates different structures of the nanospheres with most of them are spherical. Similarly, samples S2 to S4 have been found to illustrate the mixed shapes with most of them are spherical. In samples S2 and S4, NCs have been found to form aggregate due to the high NCs concentration used for TEM analysis [241].

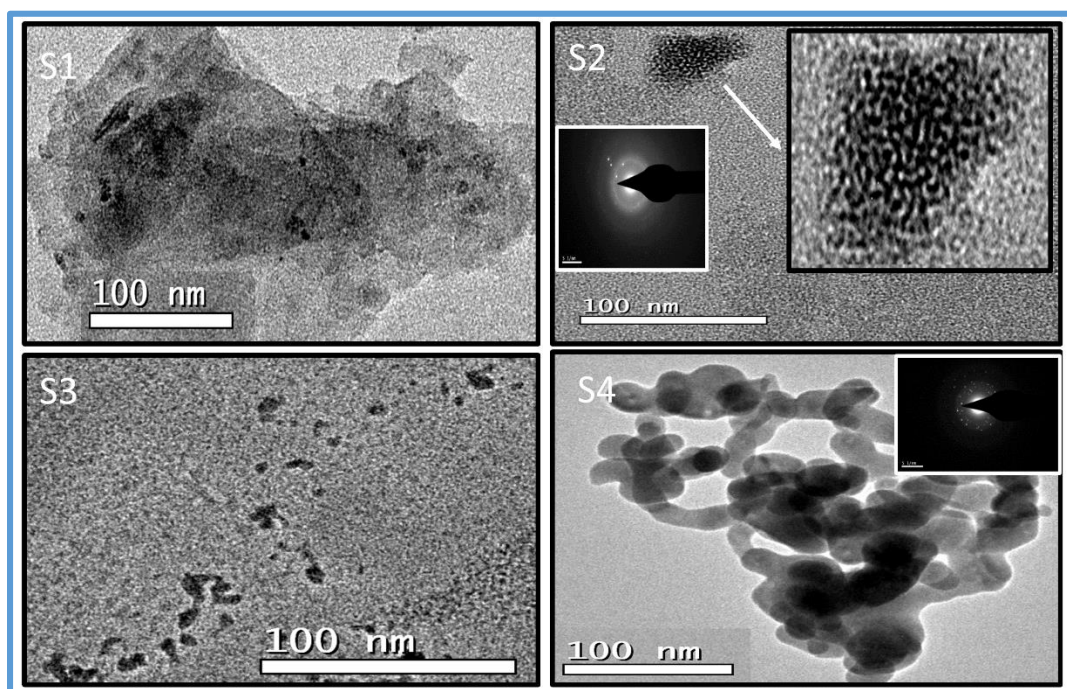


Figure 5.6: TEM images of $\text{Ag}_2\text{Se}_x\text{S}_{1-x}$ materials and SAD pattern of S2 and S4.

The image J software has been used to calculate the size of $\text{Ag}_2\text{Se}_x\text{S}_{1-x}$ nanocrystals from TEM images (figure 5.7). The size and other parameters have been calculated by the Gaussian fit of histogram plots. The size and dispersion of nanocrystals for different samples have been given in table 5.1. All the samples have been found in polydispersed nature. The size of NCs for all the samples has increased

from S1 to S4. The similar behaviour has been reported by Changyin *et al.* [242]. The composition dependent size of $\text{Ag}_2\text{Se}_x\text{S}_{1-x}$ NCs has shown a slight increase with an increase in the dopant concentration (figure 5.8). This increase in size from S1 to S4 may be due to the exchange of sulphur atoms having lower ionic radii (0.184 nm) with the selenium atoms of higher ionic radii (0.198 nm). The crystallite size obtained from XRD and TEM images shows a good agreement.

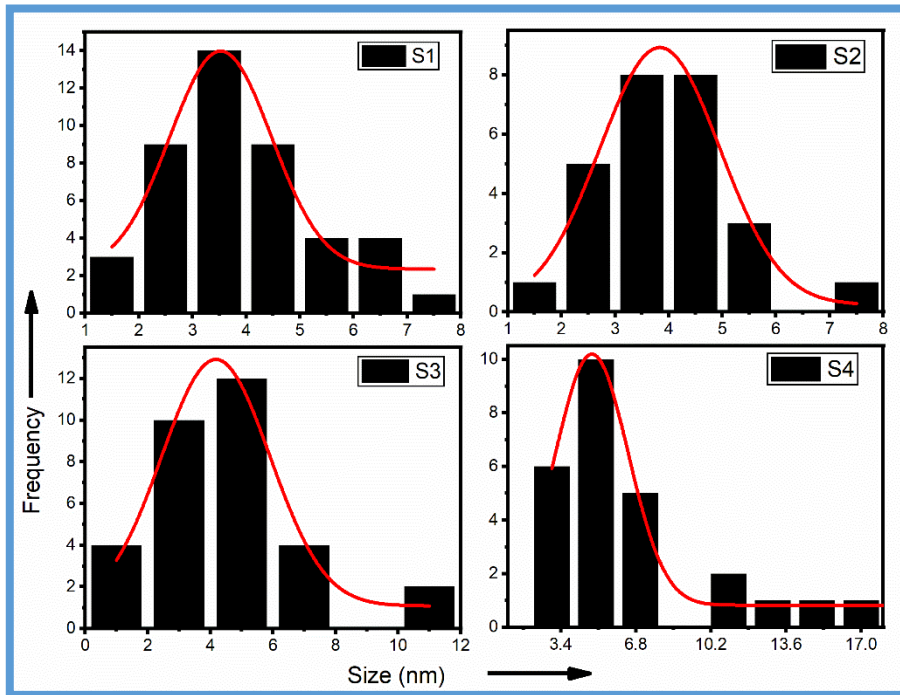


Figure 5.7: Histogram of different $\text{Ag}_2\text{Se}_x\text{S}_{1-x}$ samples.

Table 5.3: The different parameters calculated from TEM images, UV-VIS-NIR and Raman spectroscopy of $\text{Ag}_2\text{Se}_x\text{S}_{1-x}$ samples.

Name of samples	First exciton peak	Bandgap	Bandgap (By Tauc plot)	Size by Brus equation	Raman band
	(nm)	(eV)	(eV)	(nm)	(cm^{-1})
S1	905	1.37	1.35	3.8	243
S2	1024	1.21	1.21	---	239
S3	1138	1.09	1.09	---	236
S4	1352	0.92	0.88	4.1	233

Selected area diffraction (SAD) patterns of S2 and S4 have been shown in the inset of figure 5.6. Diffused rings in the S2 and S4 have shown the polycrystalline nature of the material. The sample S4 has shown intense light dots and less intensity diffused rings as compared to S2. This behaviour indicates that the sample S4 is more crystalline in nature as compared to sample S2.

5.3.4 Optical properties

Absorbance and Raman spectroscopy have been used to analyze the optical characteristics of different alloyed $\text{Ag}_2\text{Se}_x\text{S}_{1-x}$ materials.

5.3.4.1 UV-VIS-NIR spectroscopy

The spectroscopy has been used to find the absorption spectrum of $\text{Ag}_2\text{Se}_x\text{S}_{1-x}$ samples. In absorbance spectra of S1, a small peak (first exciton peak) has been found at 905 nm shown in figure 5.9. This peak has resembled with the nano bandgap of the Ag_2S material [223] [234]. Similarly, the first exciton peak has been observed for other samples and found to be shifted from 1024 nm to 1352 nm for S2 to S4 (table 5.3).

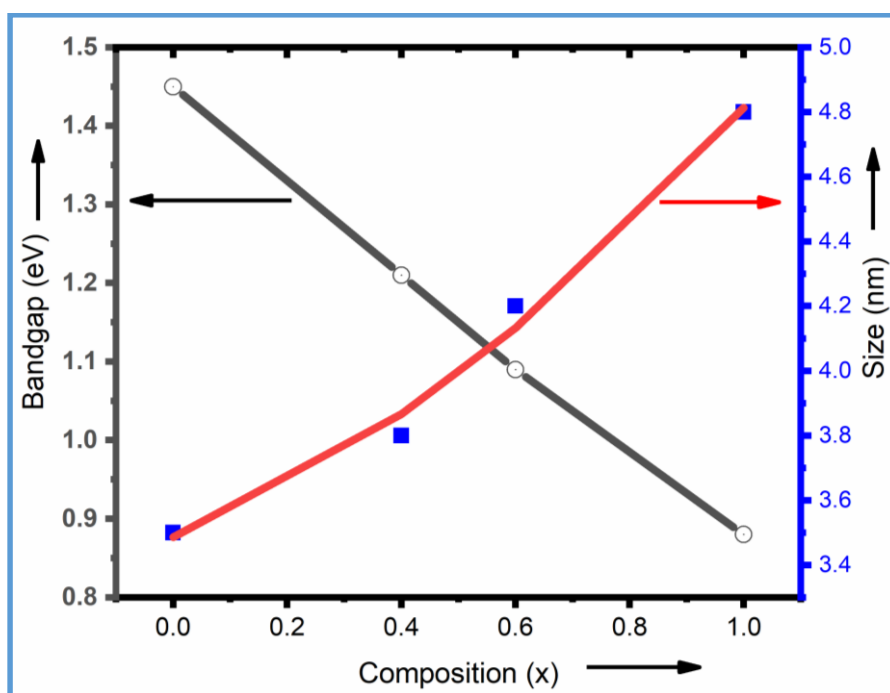


Figure 5.8: Variation of size (polynomial equation of order second has been used to fit data) and Bandgap with the composition of $\text{Ag}_2\text{Se}_x\text{S}_{1-x}$ NCs.

Overall, a redshift has been detected in the first exciton peak from S1 to S4 due to a decrease in quantum confinement. The small peak is observed around 850 nm in all the samples due to the grating change from NIR to the visible region (figure 5.9).

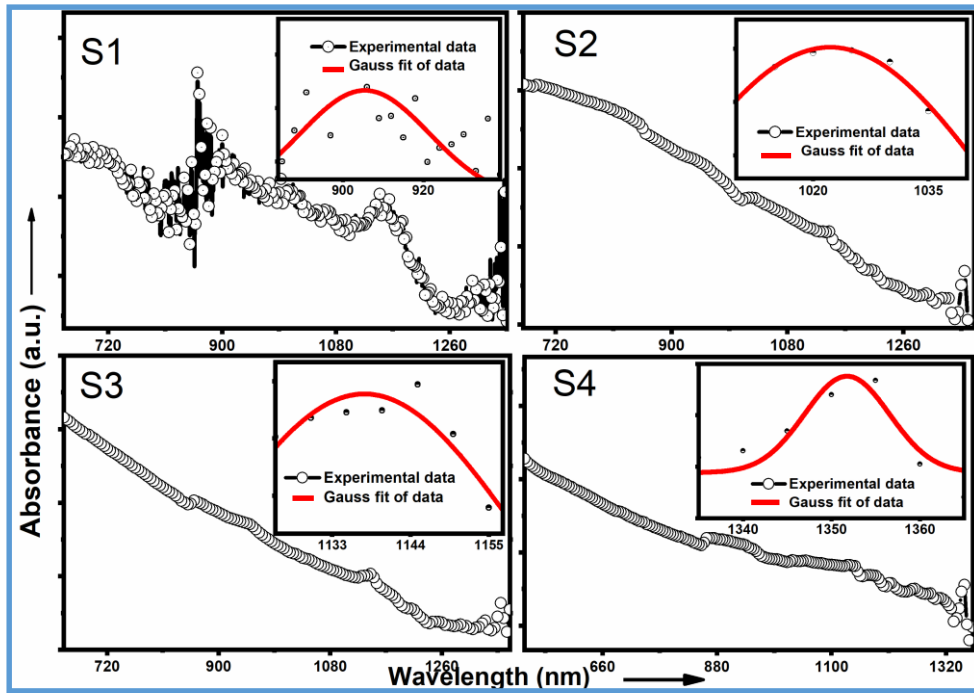


Figure 5.9: Absorption spectra of $\text{Ag}_2\text{Se}_x\text{S}_{1-x}$ samples.

The size of nanocrystals has been calculated with the help of Brus equation (2.10) [15]. The bandgap of NCs (E_g^{nano}) has been calculated by employing the equation (2.9). In equation (2.9) λ is the wavelength corresponding to the first exciton peak in absorption spectra. The values of E_g^{bulk} , m_e^* , m_h^* and ϵ for Ag_2S are 1.08 eV, $0.286m_0$, $1.096m_0$ and 8.36 respectively [243] and the values of E_g^{bulk} , m_e^* , m_h^* and ϵ for Ag_2Se are 0.18 eV, $0.12m_0$, $0.75m_0$ and 11 respectively [244]–[247]. The size of QDs and first exciton peak of all the Se alloyed $\text{Ag}_2\text{Se}_x\text{S}_{1-x}$ samples have been given in table 5.2. The size of the QDs has been noticed to increase from S1 to S4. A similar trend has been observed for the size of QDs estimated by image J software from TEM images.

Griffiths equation (2.11) has been used to calculate the exciton radius of Ag_2S and Ag_2Se QDs. The Bohr exciton radius of Ag_2S and Ag_2Se has been calculated and equal to be 2.0 nm and 5.6 nm respectively. The size of QDs for S1 is lying in between

2 nm to 5 nm as observed by TEM and Brus equation. This indicated that the S1 has belonged to “weak quantum confinement region” and is consistent with the result as revealed from the absorbance spectra. If the QD radius is less than a_0 , it is assumed to be in the “strong confinement regime” and quantum effects apply [248]. The size of QDs for S4 is less than 5.6 nm as observed by TEM and Brus equation. This indicated that the S4 has belonged to “strong quantum confinement region” and shown large quantum confinement as revealed from the first exciton peak of UV-VIS-NIR absorption spectra.

The bandgap of the $\text{Ag}_2\text{Se}_x\text{S}_{1-x}$ samples has been calculated by using the Tauc plot. The absorption coefficient (α) is calculated by equation (2.8). Bandgap calculated using the Tauc relation has been given in table 5.3. The increase in the size of nanocrystals from S1 to S4 has small (0.3 nm – 0.6 nm) but, a red shift in the first exciton peak (905 nm to 1352 nm) is enormous. This enormous redshift depends on two factors *i.e.* size and structure changes. Here, the second factor is more responsible for the change in the bandgap of the material.

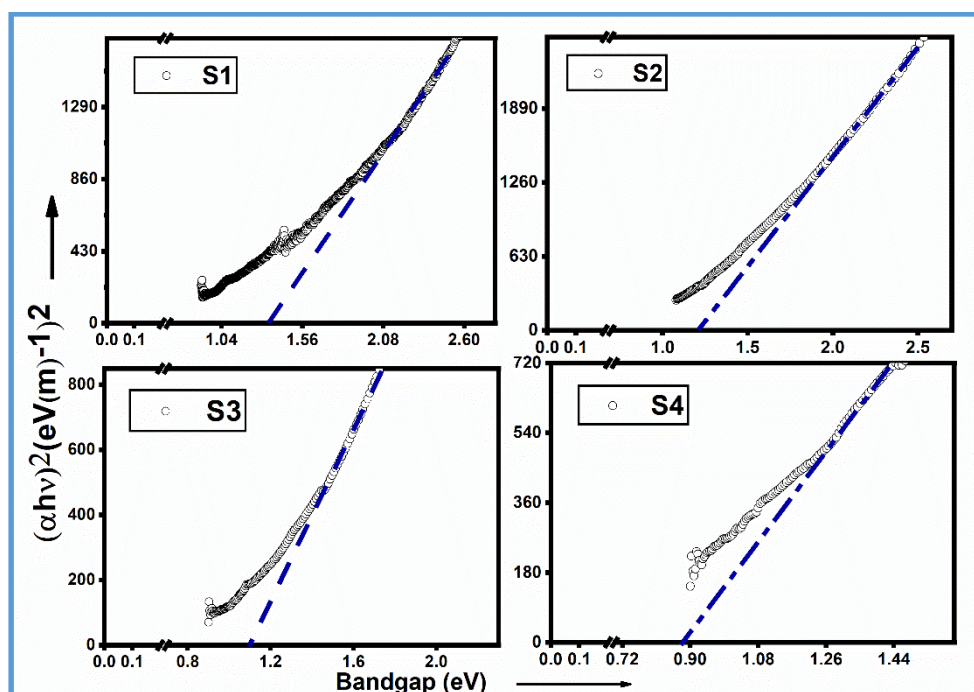


Figure 5.10: Tauc plot of $\text{Ag}_2\text{Se}_x\text{S}_{1-x}$ QDs.

The increase in the addition of alloying concentration from S1 to S4 leads to more structural changes in the material. The reason for this may be the electronegativity difference in sulphur and selenium atoms. Sulphur atoms are more electronegativity which attracts a shared pair of an electron more tightly as compared to selenium atoms. This phenomenon results in the modification of the energy levels of $\text{Ag}_2\text{Se}_x\text{S}_{1-x}$ nanocrystals.

The sample S1 has shown a maximum bandgap as compared to other samples which are due to the small crystallite size of Ag_2S . The formation of discrete states in the optical bandgap has increased the effective band gap of $\text{Ag}_2\text{Se}_x\text{S}_{1-x}$ NCs. The bandgap of nanocrystals has been detected to decrease from S1 to S4. The composition dependent bandgap of $\text{Ag}_2\text{Se}_x\text{S}_{1-x}$ nanocrystals has been shown in figure 5.8. Here, with the increase in dopant concentration, the bandgap of nanocrystals has decreased. This decrease in the bandgap is due to the replacement of sulphur ions (larger ionic radius) by selenium ions (smaller ionic radius) which produces the energy levels in between the bandgap.

5.3.4.2 Raman spectroscopy

Raman spectra of different $\text{Ag}_2\text{Se}_x\text{S}_{1-x}$ nanocrystals has been shown in figure 5.11. Raman broadband for sample 1 has been observed at 243 cm^{-1} indicates the presence of $\alpha\text{-Ag}_2\text{S}$ (figure 5.11) [226]. The Raman band has been observed at 243 cm^{-1} and ascribed to the asymmetric bending and stretching Ag-S-Ag . Raman broadband for S4 arises at 233 cm^{-1} indicates the existence of Ag_2Se [249]–[251]. The Raman band has been observed at 233 cm^{-1} due to Ag-Se and Se-Se stretching. The monoclinic structure of Ag_2S has made up of two modes A_g and B_g . A_g mode corresponds to vibrations of the Ag atoms and B_g mode corresponds to vibrations of the S atoms. The A_g mode has further divided into A_{g1} and A_{g2} modes. In A_{g1} mode, Ag atoms have occupied tetrahedral sites in a bcc configuration of the surrounding of S atoms. In A_{g2} mode, Ag atoms have occupied octahedral sites in a bcc configuration of the surrounding of S atoms. The B_g mode has represented the distorted body-centred cubic (bcc) configuration of S atoms in $\alpha\text{-Ag}_2\text{S}$ material. The B_g mode remains the same in bulk as well as nanocrystalline Ag_2S material. As the content of alloying increases from S1 to S4, more and more sulphur atoms have been replaced by the selenium atoms. Raman bands for S2 and S3 exist in between 243 cm^{-1} and 233 cm^{-1} (table 5.3). This

shift in Raman band towards lower wavenumber is due to the increase in the bond length (Ag-Se) from S1 to S4. The extra Raman band has been observed at 497 cm^{-1} in S3 is due to the photodecomposition products of Ag_2S on account of the large exposure time taken for obtaining the Raman spectra [226]. Raman bands in between 804 cm^{-1} to 853 cm^{-1} are due to the vibrations of the CO_3^{2-} ions in all the samples. These peaks have indicated that 3- MPA is present on the surface of QDs.

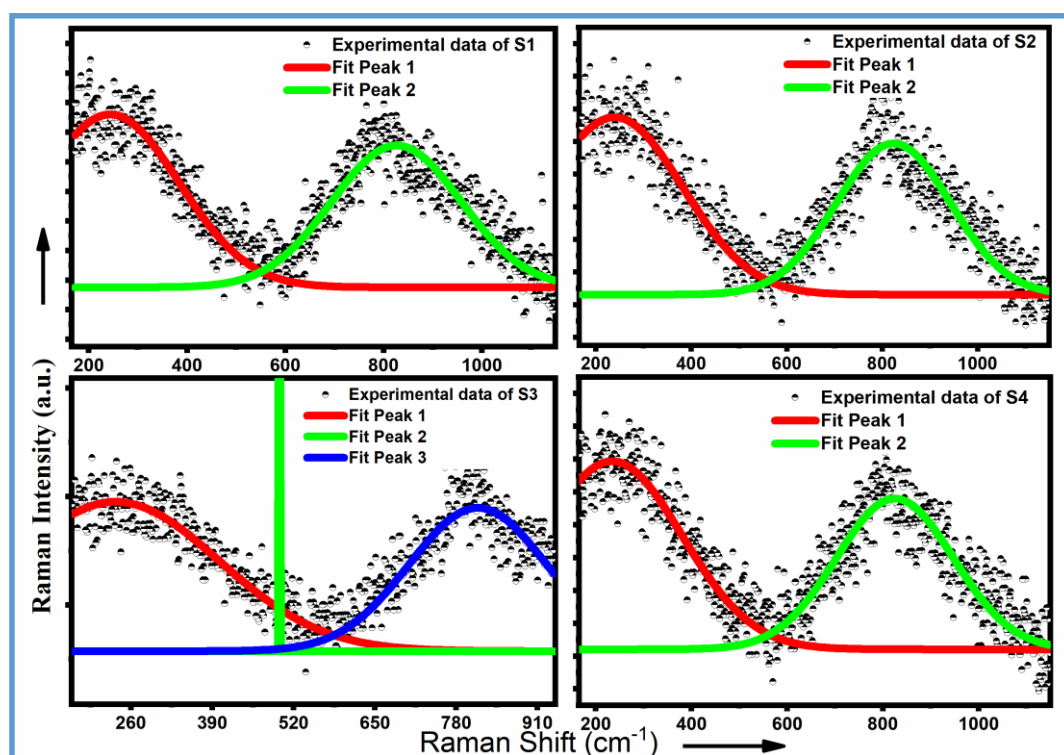


Figure 5.11: Raman spectra of $\text{Ag}_2\text{Se}_x\text{S}_{1-x}$ nanocrystals.

Quantum confinement in Se alloyed $\text{Ag}_2\text{Se}_x\text{S}_{1-x}$ QDs arises due to both the size and concentration of selenium ions. From the results, it is clear that the synthesized $\text{Ag}_2\text{Se}_x\text{S}_{1-x}$ QDs are appropriate for energy harvesting in the visible to NIR region.

5.4 Conclusion

The co-precipitation technique has been used to synthesize the $\text{Ag}_2\text{Se}_x\text{S}_{1-x}$ QDs. FTIR spectra of different materials have provided information about that attachment of surfactant (3-MPA) to the surface of the QDs. The size of the QDs has been calculated

by WH plot, histogram plot of TEM images and Brus equation. These three approaches have revealed approximately the same size. SAD patterns have illustrated the crystallinity of the samples. The values of bandgap have been calculated by Tauc plot and indicate the quantum confinement in all the $\text{Ag}_2\text{Se}_x\text{S}_{1-x}$ samples. The obtained results show that the quantum confinement depends upon both the size and composition of the material. Raman spectra have provided information about the formation of the desired alloyed structure. The synthesized QDs may be suitable for devices requiring quantum confinement that are influenced by even a little change in size.

CHAPTER- 6

Summary and Future Work

In this thesis, binary and alloyed silver chalcogenide nanoparticles and QDs have been synthesized by the bottom-up approach. The co-precipitation and hydrothermal approaches of wet chemical methods are employed. The summary of the results has been described below.

6.1 Summary

The co-precipitation and hydrothermal techniques have been used for the optimization of conditions for the synthesis of Ag_2Se QDs. The Ag_2Se samples have been synthesized by changing pH, molar ratio and synthesis methods. The Ag_2Se QDs have been synthesized by co-precipitation approach by optimization of different parameters. The samples of Ag_2Se have been prepared by varying the ratio of $\text{AgCl}/2\text{-MPA}$, $\text{Na}_2\text{SeO}_3/\text{H.D.}$ and varying the pH. The orthorhombic phase of the nanoparticles has been confirmed by XRD. The crystallite size of samples has been calculated using the Scherrer and WH plot method. The change in pH of the solution from 13 to 11 at a constant molar ratio of $\text{AgCl}/2\text{-MPA}$ and $\text{Na}_2\text{SeO}_3/\text{H.D.}$ leads to the formation of larger size Ag_2Se nanoparticles (> 10 nm). The change in the MR of $\text{AgCl}/2\text{-MPA}$ and $\text{Na}_2\text{SeO}_3/\text{H.D.}$ at constant pH of the solution also leads to the formation of larger size Ag_2Se nanoparticles (> 10 nm). Therefore, the initial precursors have been changed from AgCl to AgNO_3 , Na_2SeO_3 to Se powder and in addition to this H.D. has been used both as capping agent as well as reducing agent. The temperature of the solution has also been changed from 75°C to 70°C . The presence of silver and selenium elements in Ag_2Se have been confirmed from EDX spectra. TEM images have been used to calculate the size and nature of nanocrystals. The band gap of QDs has been determined using the Tauc's plot. It has been observed that the nanocrystals' size varies from 5 nm to 31.6 nm with the change in pH of the solution at a constant molar ratio of $\text{Se}/\text{H.D.}$ QDs have been formed for the lowest value of pH of the solution close to 9. The band gap has decreased with the increase in size of material. The hydrothermal approach has also been explored for the synthesis of Ag_2Se NCs. The MR of $\text{AgNO}_3/\text{H.D.}$ has been kept constant at 0.09 M during this synthesis. The final product obtained resulted in crystallites of large size of approximately 400 nm. So, the synthesis by the hydrothermal approach has been found to be unsuitable in comparison to the co-precipitation

approach. In view of these results, the co-precipitation technique has been employed for the synthesis of silver chalcogenide QDs with the initial precursors AgNO_3 , elemental Se or S, H.D. and ammonia (to regulate the pH).

Ag_2S QDs have been synthesized by varying the synthesis time with co-precipitation approach. Initial precursors AgNO_3 , S powder, capping agent 3- MPA and OA have been used for the synthesis of Ag_2S QDs. The different samples of Ag_2S have been prepared by varying the synthesis time from 5 minutes to 60 minutes at a constant molar ratio of $\text{AgNO}_3/3\text{-MPA}$, AgNO_3/OA and the pH of the solution. The temperature of the solution has been maintained at $80\text{ }^\circ\text{C} \pm 2\text{ }^\circ\text{C}$. The structural and optical characterization has been performed on different Ag_2S samples. XRD data indicated the presence of monoclinic, mixed monoclinic and cubic phases in the different samples. The size of QDs calculated from the histogram plot of TEM images has shown a good match with the size calculated from Brus equation. Quantum confinement has been observed in the Ag_2S samples due to the formation of $\beta\text{-Ag}_2\text{S}$ phase which has been confirmed from XRD spectra. The quantum confinement has also been confirmed by the absorption spectra of Ag_2S QDs. The blue shift in wavelength has been observed with a decrease in size. The transformation of $\alpha\text{-Ag}_2\text{S}$ to $\beta\text{-Ag}_2\text{S}$ phase has also been confirmed by Raman spectra. Raman spectra have also provided information about different groups present on the surface of QDs. The quantum confinement behaviour of quantum dots may be employed to harvest energy in the IR and visible region of the electromagnetic spectrum.

The co-precipitation technique has been used to synthesize the Se alloyed $\text{Ag}_2\text{Se}_x\text{S}_{1-x}$ QDs. Initial precursors AgNO_3 , S powder, capping agent 3- MPA and reducing agent H.D. have been used for the synthesis of Se doped Ag_2S QDs. Different sample of $\text{Ag}_2\text{Se}_x\text{S}_{1-x}$ QDs have been prepared by varying the x mol % ($x = 0, 0.4, 0.6$ and 1.0) at constant molar ratio of $\text{AgNO}_3/3\text{-MPA}$ equal to 0.15 and constant synthesis time 5 minutes. The temperature of the solution has been maintained at $50\text{ }^\circ\text{C} \pm 2\text{ }^\circ\text{C}$. FTIR spectra of different materials have provided information about that attachment of surfactant (3-MPA) to the surface of the QDs. The size of the QDs has been calculated by WH plot, histogram plot of TEM images and Brus equation. These three approaches have revealed approximately the same size. SAD patterns have illustrated the crystallinity of the samples. The values of bandgap have been calculated by Tauc plot

and indicate the quantum confinement in all the Se alloyed $\text{Ag}_2\text{Se}_x\text{S}_{1-x}$ samples. The obtained results show that the quantum confinement depends upon both the size and composition of the material. Raman spectra have provided information about the formation of the desired alloyed structure. The synthesized QDs may be suitable for devices requiring quantum confinement that are influenced by even a little change in size

6.2 Future work

The future work of this thesis has given in the following points:

- To use silver chalcogenide QDs for the photovoltaic cell. QDs should be deposited in thin film form in between electron and hole transport layer. These may increase the efficiency of the photovoltaic cell through MEG. QDSSCs are the alternate of dye-sensitized solar cells. In QDSSC, the quantum dots are adhered with the bulk bandgap material (*e.g.* TiO_2) as depicted in figure 6 (a).

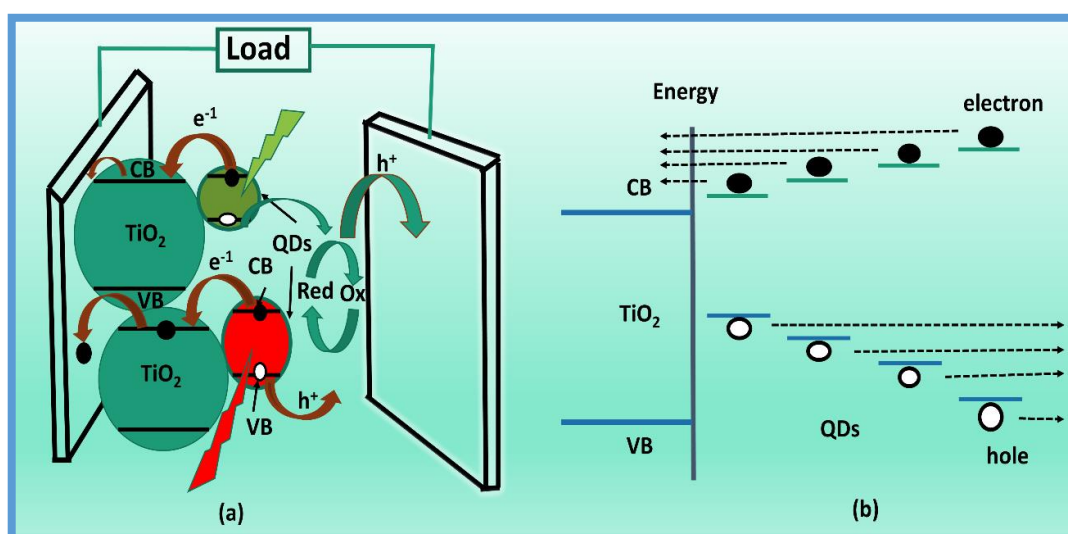
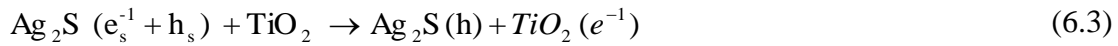


Figure 6.1. (a) Operating principle of QDSSC. (b) Role of quantum confinement on the charge transfer from quantum dots to the TiO_2 .

Generally, in QDSSC two factors are significant i.e. long term colloidal stability (long alkyl chain organic ligands) and effective charge transfer from QDs to TiO_2 (shorter and conductive ligands). So, to satisfy both conditions ligands 3-MPA (shorter and conductive ligands) and OA (long term stabilization) have been used for the synthesis of Ag_2S QDs. Carboxylic group of 3-MPA has a large attraction to bond with TiO_2 and

another end has attached to the Ag₂S QDs. This arrangement may rapidly transfer an electron from QDs to TiO₂. Electron and hole are formed in conduction band and valence band upon suitable radiation on Ag₂S QD. The incident radiation energy decides the transition of an electron from e_p⁻¹ to h_p (p level energies) or e_s⁻¹ to h_s (s level energies) as given in equation 6.1. Electron and hole in its excited state may lose its energy in three mechanisms first is to emit a photon second is to generate a phonon and third is to transfer the electron to TiO₂ and hole remain in Ag₂S as given in equation 6.2 and 6.3.



For effective energy transformation of excited electron-hole pair, the third mechanism *i.e.* to loose energy have to be dominant. The third mechanism to loose energy of excited electron-hole pair increases with the decrease in size of QDs due to size quantization effects (in figure 6 (b)). The main driving force (energy difference between the acceptor and donor systems) for the rapid electron transfer between Ag₂S and TiO₂ is governed by the energy difference between the conduction band energies of Ag₂S and TiO₂. The driving force for the rapid electron transfer increases with the increase in the bandgap of QDs. Similarly, Se alloyed Ag₂Se_xS_{1-x} quantum dots may be tested. In the quantum confinement, bandgap of nanocrystal increase with the decreases in size. This phenomenon creates silver chalcogenide QDs suitable for harvesting energy in visible to NIR regions.

➤ The synthesized QDs may be used as imaging, targeting and bio labelling. Conjugation of silver chalcogenide QDs with biomolecules like peptides and antibodies could be used to target tumors in vivo. Before the use of these QDs in vivo imaging compatibility of the QDs with other cells should be checked. There may be chances of degrading of the coating by photocatalytic and oxidative conditions. Silver chalcogenide QDs have less toxicity as compared to other cadmium and lead-based QDs.

Bibliography

Bibliography

- [1] J. E. Demuth, R. J. Hamers, R. M. Tromp, and M. E. Welland, "A scanning tunneling microscope for surface science studies," *IBM J. Res. Dev.*, vol. 30, no. 4, pp. 396–402, 1986.
- [2] C. Gerber, G. Binnig, H. Fuchs, O. Marti, and H. Rohrer, "Scanning tunneling microscope combined with a scanning electron microscope," *Rev. Sci. Instrum.*, vol. 57, no. 2, pp. 221–224, Feb. 1986.
- [3] A. I. Ekimov and O. A.A., "Quantum size effect in three-dimensional microscopic semiconductor crystals," *JEPT Lett.*, vol. 34, no. 6, pp. 363–366, 1981.
- [4] L. E. Brus, "Electron-electron and electron-hole interactions in small semiconductor crystallites: The size dependence of the lowest excited electronic state," *J. Chem. Phys.*, vol. 80, no. 9, pp. 4403–4409, 1984.
- [5] Y. Zhang, Y. Liu, C. Li, X. Chen, and Q. Wang, "Controlled Synthesis of Ag₂S Quantum Dots and Experimental Determination of the Exciton Bohr Radius," *J. Phys. Chem. C*, vol. 118, no. 9, pp. 4918–4923, 2014.
- [6] P. Harrison, *Quantum wells, wires and dots*. 2005.
- [7] H. S. Mansur and A. A. P. Mansur, "CdSe quantum dots stabilized by carboxylic-functionalized PVA: Synthesis and UV-vis spectroscopy characterization," *Mater. Chem. Phys.*, vol. 125, no. 3, pp. 709–717, 2011.
- [8] V. Klimov, *Nanocrystal quantum dots*, Second edi. Taylor & Francis Group, 2010.
- [9] R. J. Ellingson *et al.*, "Highly efficient multiple exciton generation in colloidal PbSe and PbS quantum dots," *Nano Lett*, vol. 5, no. 5, pp. 865–871, 2005.
- [10] N. Zettili, *Quantum mechanics Concepts and Applications*, Second edi., vol. 50, no. 2. wiley, 2009.
- [11] G. . La Rocca, "Wannier–Mott Excitons in Semiconductors," vol. 31, no. 03, pp. 97–128, 2003.
- [12] V. P. M. P., "Multielectron theory of excitons in semiconductors," *Sov. Phys. JETP*, vol. 27, no. 1, pp. 324–331, 1968.
- [13] S. Baskoutas and A. F. Terzis, "Size-dependent band gap of colloidal quantum dots," *J. Appl. Phys.*, vol. 99, no. 1, pp. 013708(1–4), 2006.

- [14] E. O. Chukwuocha, M. C. Onyeaju, and T. S. T. Harry, “Theoretical Studies on the Effect of Confinement on Quantum Dots Using the Brus Equation,” *World J. Condens. Matter Phys.*, vol. 2, pp. 96–100, 2012.
- [15] L. Brus, “Electronic wave functions in semiconductor clusters: experiment and theory,” *J. Phys. Chem.*, vol. 90, no. 12, pp. 2555–2560, 1986.
- [16] Y. Kayanuma, “Quantum-size effects of interacting electrons and holes in semiconductor microcrystals with spherical shape,” *Phys. Rev. B*, vol. 38, no. 14, pp. 9797–9805, Nov. 1988.
- [17] Y. Kayanuma and H. Momiji, “Incomplete confinement of electrons and holes in microcrystals,” *Phys. Rev. B*, vol. 41, no. 14, pp. 10261–10263, May 1990.
- [18] D. J. Norris, A. Sacra, C. B. Murray, and M. G. Bawendi, “Measurement of the size dependent hole spectrum in CdSe quantum dots,” *Phys. Rev. Lett.*, vol. 72, no. 16, pp. 2612–2615, 1994.
- [19] D. J. Norris and M. G. Bawendi, “Measurement and assignment of the size-dependent optical spectrum in CdSe quantum dots,” *Phys. Rev. B*, vol. 53, no. 24, pp. 16338–16346, Jun. 1996.
- [20] Y. Wang, A. Suna, W. Mahler, and R. Kasowski, “PbS in polymers. From molecules to bulk solids,” *J. Chem. Phys.*, vol. 87, no. 12, pp. 7315–7322, 1987.
- [21] Y. Nosaka, “Finite depth spherical well model for excited states of ultrasmall semiconductor particles. An application,” *J. Phys. Chem.*, vol. 95, no. 13, pp. 5054–5058, 1991.
- [22] P. C. Hiemenz and R. Rajagopalan, *Principles of colloid and surface chemistry*, 3rd ed. NEW YORK: MARCEL DEKKER, INC, 1997.
- [23] H. Zhu, N. Song, and T. Lian, “Controlling charge separation and recombination rates in CdSe/ZnS type I core-shell quantum dots by shell thicknesses,” *J. Am. Chem. Soc.*, vol. 132, no. 42, pp. 15038–15045, 2010.
- [24] C. T. Smith *et al.*, “Energy structure of CdSe/CdTe type II colloidal quantum dots—Do phonon bottlenecks remain for thick shells?,” *Sol. Energy Mater. Sol. Cells*, vol. 158, pp. 160–167, Dec. 2016.
- [25] X. Yuan *et al.*, “Dual emissive manganese and copper co-doped Zn-In-S quantum dots as a single color-converter for high color rendering white-light-emitting diodes,” *ACS Appl. Mater. Interfaces*, vol. 7, no. 16, pp. 8659–8666,

- 2015.
- [26] J. M. Allan, M. Abdul Mumin, W. Z. Xu, Q. Al Sharari, and P. A. Charpentier, "Surface functionalized bare and core-shell quantum dots in poly(ethylene-co-vinyl acetate) for light selective nanocomposite films," *Sol. Energy Mater. Sol. Cells*, vol. 123, pp. 30–40, 2014.
- [27] L. Liu, Q. Peng, and Y. Li, "An Effective Oxidation Route to Blue Emission CdSe Quantum Dots," *Inorg. Chem.*, vol. 47, no. 8, pp. 3182–3187, Apr. 2008.
- [28] H. Lin, C. Wang, J. Wu, Z. Xu, Y. Huang, and C. Zhang, "Colloidal synthesis of MoS₂ quantum dots: Size-dependent tunable photoluminescence and bioimaging," *New J. Chem.*, vol. 39, no. 11, pp. 8492–8497, 2015.
- [29] E. Rajaei and M. A. Borji, "Impact of Dot Size on Dynamical Characteristics of InAs/GaAs Quantum Dot Lasers," *J. Nanoelectron. Optoelectron.*, vol. 12, no. 9, pp. 945–951, 2017.
- [30] A. Ganesan, A. Houtepen, and R. Crisp, "Quantum Dot Solar Cells: Small Beginnings Have Large Impacts," *Appl. Sci.*, vol. 8, no. 10, p. 1867, 2018.
- [31] S. Dhara and P. K. Giri, "Size Dependent Anisotropic Strain and Optical Properties of Strained Si Nanocrystals," *J. Nanosci. Nanotechnol.*, vol. 11, no. 10, pp. 9215–9221, 2011.
- [32] S. Taniguchi and M. Green, "The synthesis of CdTe/ZnS core/shell quantum dots using molecular single-source precursors," *J. Mater. Chem. C*, vol. 3, no. 32, pp. 8425–8433, 2015.
- [33] K. Tanaka and K. Shimakawa, *Amorphous Chalcogenide Semiconductors and Related Materials*. Springer, 2011.
- [34] L. Yan *et al.*, "Near-infrared light emitting diodes using PbSe quantum dots," *RSC Adv.*, vol. 5, no. 67, pp. 54109–54114, 2015.
- [35] J. E. Murphy *et al.*, "PbTe colloidal nanocrystals: Synthesis, characterization, and multiple exciton generation," *J. Am. Chem. Soc.*, vol. 128, no. 10, pp. 3241–3247, 2006.
- [36] H. Zhao, M. Chaker, and D. Ma, "Effect of CdS shell thickness on the optical properties of water-soluble, amphiphilic polymer-encapsulated PbS/CdS core/shell quantum dots," *J. Mater. Chem.*, vol. 21, no. 43, pp. 17483–17491, 2011.

- [37] J. Zhang, R. W. Crisp, J. Gao, D. M. Kroupa, M. C. Beard, and J. M. Luther, "Synthetic Conditions for High-Accuracy Size Control of PbS Quantum Dots.," *J. Phys. Chem. Lett.*, vol. 6, no. 10, pp. 1830–1833, 2015.
- [38] A. Aboulaich *et al.*, "One-pot noninjection route to CdS quantum dots via hydrothermal synthesis," *ACS Appl. Mater. Interfaces*, vol. 4, no. 5, pp. 2561–2569, 2012.
- [39] G. Sreedhar, A. Sivanantham, S. Venkateshwaran, S. K. Panda, and M. Eashwar, "Enhanced photoelectrochemical performance of CdSe quantum dot sensitized SrTiO₃," *J. Mater. Chem. A*, vol. 3, no. 25, pp. 13476–13482, 2015.
- [40] S. K. Haram *et al.*, "Quantum confinement in CdTe quantum dots: Investigation through cyclic voltammetry supported by density functional theory (DFT)," *J. Phys. Chem. C*, vol. 115, no. 14, pp. 6243–6249, 2011.
- [41] I. Hocaoglu *et al.*, "Development of highly luminescent and cytocompatible near-IR-emitting aqueous Ag₂S quantum dots," *J. Mater. Chem.*, vol. 22, no. 29, pp. 14674–14681, 2012.
- [42] Y.-P. Gu, R. Cui, Z.-L. Zhang, Z.-X. Xie, and D.-W. Pang, "Ultra-Small Near-Infrared Ag₂Se Quantum Dots with Tunable Fluorescence for in-vivo Imaging.," *J. Am. Chem. Soc.*, vol. 134, no. 1, pp. 79–82, 2012.
- [43] W. J. Mir, A. Swarnkar, R. Sharma, A. Katti, K. V. Adarsh, and A. Nag, "Origin of Unusual Excitonic Absorption and Emission from Colloidal Ag₂S Nanocrystals: Ultrafast Photophysics and Solar Cell," *J. Phys. Chem. Lett.*, vol. 6, no. 19, pp. 3915–3922, 2015.
- [44] M. Langevin, D. Lachance-quirion, and A. M. Ritcey, "Size-Dependent Extinction Coefficients and Transition Energies of Near-Infrared β -Ag₂Se Colloidal Quantum Dots," *J. Phys. Chem. C*, vol. 117, no. 5424–5428, pp. 5424–5428, 2013.
- [45] C. Zhu, P. Jiang, Z. Zhang, D. Zhu, Z. Tian, and D. Pang, "Ag₂Se Quantum Dots with Tunable Emission in the Second Near-Infrared Window," *ACS Appl. Mater. Interfaces*, vol. 5, p. 1186–1189, 2013.
- [46] C. Chen, X. He, L. Gao, and N. Ma, "Cation exchange-based facile aqueous synthesis of small, stable, and nontoxic near-infrared Ag₂Te/ZnS core/shell quantum dots emitting in the second biological window," *ACS Appl. Mater.*

- Interfaces*, vol. 5, no. 3, pp. 1149–1155, 2013.
- [47] P. Jiang, Z.-Q. Tian, C.-N. Zhu, Z.-L. Zhang, and D.-W. Pang, “Emission-Tunable Near-Infrared Ag₂S Quantum Dots,” *Chem. Mater.*, vol. 24, no. 1, pp. 3–5, 2012.
- [48] M. Yarema *et al.*, “Infrared Emitting and Photoconducting Colloidal Silver Chalcogenide Nanocrystal Quantum Dots from a Silylamide Promoted Synthesis,” *ACS Nano*, vol. 5, no. 5, pp. 3758–3765, 2011.
- [49] A. Sahu, A. Khare, D. D. Deng, and D. J. Norris, “Quantum confinement in silver selenide semiconductor nanocrystals,” *Chem. Commun.*, vol. 48, no. 44, pp. 5458–60, 2012.
- [50] H.-Y. Yang, Y.-W. Zhao, Z.-Y. Zhang, H.-M. Xiong, and S.-N. Yu, “One-pot synthesis of water-dispersible Ag₂S quantum dots with bright fluorescent emission in the second near-infrared window,” *Nanotechnology*, vol. 24, no. 5, p. 055706, 2013.
- [51] C. Ji *et al.*, “Temperature-Dependent Photoluminescence of Ag₂Se Quantum Dots,” *J. Phys. Chem. C*, vol. 119, no. 24, pp. 13841–13846, 2015.
- [52] L.-J. Shi *et al.*, “Near-infrared Ag₂Se quantum dots with distinct absorption features and high fluorescence quantum yields,” *RSC Adv.*, vol. 6, no. 44, pp. 38183–38186, 2016.
- [53] J. Kim *et al.*, “Highly fluorescent CdTe quantum dots with reduced cytotoxicity—A Robust biomarker,” *Sens. Bio-Sensing Res.*, vol. 3, no. December, pp. 46–52, Mar. 2015.
- [54] I. V. Martynenko, A. P. Litvin, F. Purcell-Milton, A. V. Baranov, A. V. Fedorov, and Y. K. Gun’ko, “Application of semiconductor quantum dots in bioimaging and biosensing,” *J. Mater. Chem. B*, vol. 5, no. 33, pp. 6701–6727, 2017.
- [55] X. Gao, “Multifunctional quantum dots for cellular and molecular imaging,” in *2007 29th Annual International Conference of the IEEE Engineering in Medicine and Biology Society*, 2007, pp. 524–525.
- [56] D. Ren, B. Wang, C. Hu, and Z. You, “Quantum dot probes for cellular analysis,” *Anal. Methods*, vol. 9, no. 18, pp. 2621–2632, 2017.
- [57] F. F. Marshall, X. Gao, S. Nie, J. W. Simons, J. A. Petros, and L. Yang, “In vivo molecular and cellular imaging with quantum dots,” *Curr. Opin. Biotechnol.*,

- vol. 16, no. 1, pp. 63–72, 2004.
- [58] P. Malinowski *et al.*, “Thin-Film Quantum Dot Photodiode for Monolithic Infrared Image Sensors,” *Sensors*, vol. 17, no. 12, p. 2867, Dec. 2017.
- [59] R. Y. Wang, R. Tangirala, S. Raoux, J. L. Jordan-Sweet, and D. J. Milliron, “Ionic and electronic transport in Ag 2S nanocrystal-GeS 2 matrix composites with size-controlled Ag 2S nanocrystals,” *Adv. Mater.*, vol. 24, no. 1, pp. 99–103, 2012.
- [60] Zhenyue Luo, Daming Xu, and Shin-Tson Wu, “Emerging Quantum-Dots-Enhanced LCDs,” *J. Disp. Technol.*, vol. 10, no. 7, pp. 526–539, Jul. 2014.
- [61] F. Hetsch, N. Zhao, S. V. Kershaw, and A. L. Rogach, “Quantum dot field effect transistors,” *Mater. Today*, vol. 16, no. 9, pp. 312–325, 2013.
- [62] P. Prabhakaran, W. J. Kim, K.-S. Lee, and P. N. Prasad, “Quantum dots (QDs) for photonic applications,” *Opt. Mater. Express*, vol. 2, no. 5, p. 578, 2012.
- [63] A. Zakery and S. R. Elliott, “Optical properties and applications of chalcogenide glasses: A review,” *J. Non. Cryst. Solids*, vol. 330, no. 1–3, pp. 1–12, 2003.
- [64] B. J. Eggleton, B. Luther-Davies, and K. Richardson, “Chalcogenide photonics,” *Nat. Photonics*, vol. 5, pp. 141–148, 2011.
- [65] A. Abrutis *et al.*, “Hot-Wire Chemical Vapor Deposition of Applications,” *Chem. Mater.*, vol. 20, no. 5, pp. 3557–3559, 2008.
- [66] Y. Avishai and K. Kikoin, “Tunneling Through Quantum Dots with Discrete Symmetries,” in *Encyclopedia of Complexity and Systems Science*, New York, NY: Springer New York, 2013, pp. 1–16.
- [67] Y. M. Beltukov and A. A. Greshnov, “The quantum Hall effect in quantum dot systems,” *J. Phys. Conf. Ser.*, vol. 568, no. 5, p. 052011, Dec. 2014.
- [68] M. C. Beard, A. G. Midgett, M. C. Hanna, J. M. Luther, B. K. Hughes, and A. J. Nozik, “Comparing multiple exciton generation in quantum dots to impact ionization in bulk semiconductors: implications for enhancement of solar energy conversion,” *Nano Lett.*, vol. 10, no. 8, pp. 3019–27, 2010.
- [69] S. I. Sadovnikov and A. I. Gusev, “Recent progress in nanostructured silver sulfide: from synthesis and nonstoichiometry to properties,” *J. Mater. Chem. A*, vol. 5, no. 34, pp. 17676–17704, Sep. 2017.
- [70] K. Nagasuna, T. Akita, M. Fujishima, and H. Tada, “Photodeposition of Ag₂S

- quantum dots and application to photoelectrochemical cells for hydrogen production under simulated sunlight,” *Langmuir*, vol. 27, no. 11, pp. 7294–7300, 2011.
- [71] G. Hong *et al.*, “In vivo fluorescence imaging with Ag₂S quantum dots in the second near-infrared region,” *Angew. Chemie - Int. Ed.*, vol. 51, no. 39, pp. 9818–9821, 2012.
- [72] R. Gui, H. Jin, Z. Wang, and L. Tan, “Recent advances in synthetic methods and applications of colloidal silver chalcogenide quantum dots,” *Coord. Chem. Rev.*, vol. 296, no. October 2014, pp. 91–124, Jul. 2015.
- [73] P. J. Wu, J. W. Yu, H. J. Chao, and J. Y. Chang, “Silver-based metal sulfide heterostructures: Synthetic approaches, characterization, and application prospects,” *Chem. Mater.*, vol. 26, no. 11, pp. 3485–3494, 2014.
- [74] P. V. Kamat, “Quantum Dot Solar Cells. Semiconductor Nanocrystals as Light Harvesters,” *J. Phys. Chem. C*, vol. 112, no. 48, pp. 18737–18753, 2008.
- [75] Z. Liu *et al.*, “High-efficiency hybrid solar cells based on polymer/PbS_x Se_{1-x} nanocrystals benefiting from vertical phase segregation,” *Adv. Mater.*, vol. 25, no. 40, pp. 5772–5778, 2013.
- [76] J. Duan, H. Zhang, Q. Tang, B. He, and L. Yu, “Recent advances in critical materials for quantum dot-sensitized solar cells: a review,” *J. Mater. Chem. A*, vol. 3, no. 34, pp. 17497–17510, 2015.
- [77] Z. R. Abrams, M. Gharghi, A. Niv, C. Gladden, and X. Zhang, “Theoretical efficiency of 3rd generation solar cells: Comparison between carrier multiplication and down-conversion,” *Sol. Energy Mater. Sol. Cells*, vol. 99, pp. 308–315, 2012.
- [78] H. Boustanji, S. Jaziri, and J. L. Lazzari, “Contribution of a single quantum dots layer in intermediate band solar cells: A capacitance analysis,” *Sol. Energy Mater. Sol. Cells*, vol. 159, pp. 633–639, 2017.
- [79] I. M. Dharmadasa, “Third generation multi-layer tandem solar cells for achieving high conversion efficiencies,” *Sol. Energy Mater. Sol. Cells*, vol. 85, no. 2, pp. 293–300, 2005.
- [80] D. Sharma, R. Jha, and S. Kumar, “Quantum dot sensitized solar cell: Recent advances and future perspectives in photoanode,” *Sol. Energy Mater. Sol. Cells*,

- vol. 155, pp. 294–322, 2016.
- [81] H.-J. Lin, S. Vedraïne, J. Le-Rouzo, S.-H. Chen, F. Flory, and C.-C. Lee, “Optical properties of quantum dots layers: Application to photovoltaic solar cells,” *Sol. Energy Mater. Sol. Cells*, p. Ahead of Print, 2013.
- [82] A. Kechiantz, A. Afanasev, and J. L. Lazzari, “Releasing confined holes from type-II quantum dots by inelastic scattering with hot photoelectrons,” *Sol. Energy Mater. Sol. Cells*, vol. 144, pp. 767–774, 2016.
- [83] S. Dhomkar *et al.*, “Feasibility of submonolayer ZnTe/ZnCdSe quantum dots as intermediate band solar cell material system,” *Sol. Energy Mater. Sol. Cells*, vol. 117, pp. 604–609, 2013.
- [84] Y. Zhou *et al.*, “Efficiency enhancement for bulk-heterojunction hybrid solar cells based on acid treated CdSe quantum dots and low bandgap polymer PCPDTBT,” *Sol. Energy Mater. Sol. Cells*, vol. 95, no. 4, pp. 1232–1237, 2011.
- [85] X. Yao *et al.*, “Inverted quantum-dot solar cells with depleted heterojunction structure employing CdS as the electron acceptor,” *Sol. Energy Mater. Sol. Cells*, vol. 137, pp. 287–292, 2015.
- [86] P. V Kamat, “Quantum Dot Solar Cells . The Next Big Thing in Photovoltaics,” *J. Phys. Chem. Lett.*, vol. 4, no. 6, p. 908–918, 2013.
- [87] A. J. Nozik *et al.*, “Semiconductor Quantum Dots and Quantum Dot Arrays and Applications of Multiple Exciton Generation to Third-Generation Photovoltaic Solar Cells,” *Chem. Rev.*, vol. 110, no. 11, pp. 6873–6890, 2010.
- [88] M. R. Kim and D. Ma, “Quantum-dot-based solar cells: Recent advances, strategies, and challenges,” *J. Phys. Chem. Lett.*, vol. 6, no. 1, pp. 85–99, 2015.
- [89] J. Gao, A. F. Fidler, and V. I. Klimov, “Carrier multiplication detected through transient photocurrent in device-grade films of lead selenide quantum dots,” *Nat. Commun.*, vol. 6, p. , 2015.
- [90] B. Bertrand *et al.*, “Fast spin information transfer between distant quantum dots using individual electrons,” *Nat. Nanotechnol.*, no. May, pp. 6–11, 2016.
- [91] I. Neder *et al.*, “Dephasing time of GaAs electron-spin qubits coupled to a nuclear bath exceeding 200 μ s,” *Nat. Phys.*, vol. 7, no. 2, pp. 109–113, 2010.
- [92] R. Hanson and D. D. Awschalom, “Coherent manipulation of single spins in semiconductors,” *Nature*, vol. 453, no. 7198, pp. 1043–1049, 2008.

- [93] C. T. Matea *et al.*, “Quantum dots in imaging, drug delivery and sensor applications,” *Int. J. Nanomedicine*, vol. 12, pp. 5421–5431, 2017.
- [94] Hsin-Chih Yeh, E. Simone, Chunyang Zhang, and Tza-Huei Wang, “Single biomolecule detection with quantum dots in a microchannel,” in *17th IEEE International Conference on Micro Electro Mechanical Systems. Maastricht MEMS 2004 Technical Digest*, 2004, no. Figure 4, pp. 371–374.
- [95] L. Chen, Y. Liu, C. Lai, R. M. Berry, and K. C. Tam, “Aqueous synthesis and biostabilization of CdS@ZnS quantum dots for bioimaging applications,” *Mater. Res. Express*, vol. 2, no. 10, p. 105401, 2015.
- [96] J. Li and J.-J. Zhu, “Quantum dots for fluorescent biosensing and bio-imaging applications,” *Analyst*, vol. 138, no. 9, pp. 2506–2515, 2013.
- [97] S. Sadeghi, B. Ganesh Kumar, R. Melikov, M. Mohammadi Aria, H. Bahmani Jalali, and S. Nizamoglu, “Quantum dot white LEDs with high luminous efficiency,” *Optica*, vol. 5, no. 7, p. 793, 2018.
- [98] S. Bhaumik, A. Guchhait, and A. J. Pal, “Light-emitting diodes based on nontoxic zinc-alloyed silver-indium-sulfide (AIZS) nanocrystals,” *Phys. E Low-Dimensional Syst. Nanostructures*, vol. 58, no. May 2016, pp. 124–129, 2014.
- [99] M. K. Choi, J. Yang, T. Hyeon, and D.-H. Kim, “Flexible quantum dot light-emitting diodes for next-generation displays,” *npj Flex. Electron.*, vol. 2, no. 1, pp. 1–14, 2018.
- [100] H.-Y. Lin *et al.*, “Optical cross-talk reduction in a quantum-dot-based full-color micro-light-emitting-diode display by a lithographic-fabricated photoresist mold,” *Photonics Res.*, vol. 5, no. 5, p. 411, Oct. 2017.
- [101] S. Cao, W. Ji, J. Zhao, W. Yang, C. Li, and J. Zheng, “Color-tunable photoluminescence of Cu-doped Zn–In–Se quantum dots and their electroluminescence properties,” *J. Mater. Chem. C*, vol. 4, no. 3, pp. 581–588, 2016.
- [102] H. Kang *et al.*, “High-performance polymer tandem devices combining solar cell and light-emitting diode,” *Sol. Energy Mater. Sol. Cells*, vol. 107, pp. 148–153, 2012.
- [103] S. Coe, W.-K. Woo, M. Bawendi, V. Bulović, and V. Bulovic, “Electroluminescence from single monolayers of nanocrystals in molecular

- organic devices,” *Nat. Lett.*, vol. 420, no. 6917, pp. 800–803, 2002.
- [104] Q. Sun *et al.*, “Bright, multicoloured light-emitting diodes based on quantum dots,” *Nat. Photonics*, vol. 1, no. 12, pp. 717–722, 2007.
- [105] S. Liu *et al.*, “Top-emitting quantum dots light-emitting devices employing microcontact printing with electricfield-independent emission.,” *Sci. Rep.*, vol. 6, no. February, p. 22530, 2016.
- [106] O. Wada and C. Jin, “Ultrafast, Energy-Efficient Photonic Switches Based on Semiconductor Nanostructures,” in *Asia Communications and Photonics Conference 2013*, 2013, no. November 2014, p. ATh3B.4.
- [107] E. A. Dias, J. I. Saari, P. Tyagi, and P. Kambhampati, “Improving optical gain performance in semiconductor quantum dots via coupled quantum shells,” *J. Phys. Chem. C*, vol. 116, no. 9, pp. 5407–5413, 2012.
- [108] M. Zhou *et al.*, “Transfer Charge and Energy of Ag@CdSe QDs-rGO Core-Shell Plasmonic Photocatalyst for Enhanced Visible Light Photocatalytic Activity,” *ACS Appl. Mater. Interfaces*, vol. 7, no. 51, pp. 28231–28243, 2015.
- [109] P. Kalisman, Y. Nakibli, and L. Amirav, “Perfect Photon-to-Hydrogen Conversion Efficiency,” *Nano Lett.*, vol. 16, no. 3, pp. 1776–1781, 2016.
- [110] P. V Kamat, “Meeting the Clean Energy Demand: Nanostructure Architectures for Solar Energy Conversion,” *J. Phys. Chem. C*, vol. 111, no. 7, pp. 2834–2860, Feb. 2007.
- [111] M. Shalom, S. Rühle, I. Hod, S. Yahav, and A. Zaban, “Energy level alignment in CdS quantum dot sensitized solar cells using molecular dipoles,” *J. Am. Chem. Soc.*, vol. 131, no. 29, pp. 9876–9877, 2009.
- [112] S. Rühle, M. Shalom, and A. Zaban, “Quantum-Dot-Sensitized Solar Cells,” *ChemPhysChem*, vol. 11, no. 11, pp. 2290–2304, Jul. 2010.
- [113] Q. Zhang *et al.*, “Highly efficient CdS/CdSe-sensitized solar cells controlled by the structural properties of compact porous TiO₂ photoelectrodes,” *Phys. Chem. Chem. Phys.*, vol. 13, no. 10, p. 4659, 2011.
- [114] P. V Kamat, “Quantum Dot Solar Cells. Semiconductor Nanocrystals as Light Harvesters,” *J. Phys. Chem. C*, vol. 112, no. 48, pp. 18737–18753, 2008.
- [115] J. H. Bang and P. V. Kamat, “Quantum Dot Sensitized Solar Cells. A Tale of Two Semiconductor Nanocrystals: CdSe and CdTe,” *ACS Nano*, vol. 3, no. 6,

- pp. 1467–1476, Jun. 2009.
- [116] A. Kongkanand, K. Tvrđy, K. Takechi, M. Kuno, and P. V Kamat, “Quantum Dot Solar Cells. Tuning Photoresponse through Size and Shape Control of CdSe–TiO₂ Architecture,” *J. Am. Chem. Soc.*, vol. 130, no. 12, pp. 4007–4015, Mar. 2008.
- [117] R. G. Aswathy, Y. Yoshida, T. Maekawa, and D. S. Kumar, “Near-infrared quantum dots for deep tissue imaging,” *Anal. Bioanal. Chem.*, vol. 397, no. 4, pp. 1417–1435, 2010.
- [118] E. I. Altinoğlu and J. H. Adair, “Near infrared imaging with nanoparticles,” *Wiley Interdiscip. Rev. Nanomedicine Nanobiotechnology*, vol. 2, no. 5, pp. 461–477, 2010.
- [119] P. Sharma, S. Brown, G. Walter, S. Santra, and B. Moudgil, “Nanoparticles for bioimaging,” *Adv. Colloid Interface Sci.*, vol. 123–126, no. SPEC. ISS., pp. 471–485, Nov. 2006.
- [120] J. V. Frangioni, A. Nakayama, Y. T. Lim, S. Kim, N. E. Stott, and M. G. Bawendi, “Selection of Quantum Dot Wavelengths for Biomedical Assays and Imaging,” *Mol. Imaging*, vol. 2, no. 1, pp. 50–64, 2003.
- [121] J. V. Frangioni, “In vivo near-infrared fluorescence imaging,” *Curr. Opin. Chem. Biol.*, vol. 7, no. 5, pp. 626–634, 2003.
- [122] M. Tomasulo, I. Yildiz, and F. M. Raymo, “pH-sensitive quantum dots,” *J. Phys. Chem. B*, vol. 110, no. 9, pp. 3853–3855, 2006.
- [123] N. Sahu, N. Brahme, and R. Sharma, “Effect of capping agent on the particle size of CdSe nanoparticles,” *Luminescence*, vol. 31, no. 7, pp. 1400–1406, Nov. 2016.
- [124] S. Sain and S. K. Pradhan, “Mechanochemical solid state synthesis of (Cd_{0.8}Zn_{0.2})S quantum dots: Microstructure and optical characterizations,” *J. Alloys Compd.*, vol. 509, no. 10, pp. 4176–4184, 2011.
- [125] M. F. Bertino *et al.*, “Quantum dots by ultraviolet and x-ray lithography,” *Nanotechnology*, vol. 18, no. 31, p. 315603, 2007.
- [126] S. Sain, S. Patra, and S. K. Pradhan, “Quickest ever single-step mechanosynthesis of Cd_{0.5}Zn_{0.5}S quantum dots: Nanostructure and optical characterizations,” *Mater. Res. Bull.*, vol. 47, no. 4, pp. 1062–1072, 2012.

- [127] V. Nandwana *et al.*, “Direct patterning of quantum dot nanostructures via electron beam lithography,” *J. Mater. Chem.*, vol. 21, no. 42, pp. 16859–16862, 2011.
- [128] D. Beke *et al.*, “Characterization of luminescent silicon carbide nanocrystals prepared by reactive bonding and subsequent wet chemical etching,” *Appl. Phys. Lett.*, vol. 99, no. 21, pp. 213108(1–4), 2011.
- [129] J. Yang *et al.*, “A top-down strategy towards monodisperse colloidal lead sulphide quantum dots,” *Nat. Commun.*, vol. 4, p. 1695, 2013.
- [130] D. C. Aveline, L. Baumgartel, B. Ahn, and N. Yu, “Focused ion beam engineered whispering gallery mode resonators with open cavity structure,” *Opt. Express*, vol. 20, no. 16, pp. 18091–18096, 2012.
- [131] P. Colson, C. Henrist, and R. Cloots, “Nanosphere Lithography: A Powerful Method for the Controlled Manufacturing of Nanomaterials,” *J. Nanomater.*, vol. 2013, pp. 1–19, 2013.
- [132] T. J. Merkel, K. P. Herlihy, J. Nunes, R. M. Orgel, J. P. Rolland, and J. M. DeSimone, “Scalable, Shape-Specific, Top-Down Fabrication Methods for the Synthesis of Engineered Colloidal Particles,” *Langmuir*, vol. 26, no. 16, pp. 13086–13096, Aug. 2010.
- [133] T.-S. Wong, B. Brough, and C.-M. Ho, “Creation of functional micro/nano systems through top-down and bottom-up approaches,” *Mol. Cell. Biomech.*, vol. 6, no. 1, pp. 1–55, Mar. 2009.
- [134] A. Valizadeh *et al.*, “Quantum dots: synthesis, bioapplications, and toxicity,” *Nanoscale Res. Lett.*, vol. 7, no. 1, pp. 480(1–14), 2012.
- [135] S. Pandey and S. B. Mishra, “Sol-gel derived organic-inorganic hybrid materials: Synthesis, characterizations and applications,” *J. Sol-Gel Sci. Technol.*, vol. 59, no. 1, pp. 73–94, 2011.
- [136] B. B. Lakshmi, P. K. Dorhout, and C. R. Martin, “0024.Chem.Mater.1997,9,857.pdf,” vol. 4756, no. 8, pp. 857–862, 1997.
- [137] D. Segal, “Chemical synthesis of ceramic materials,” *J. Mater. Chem.*, vol. 7, no. 8, pp. 1297–1305, 1997.
- [138] H. Yu, Y. Liu, and S. L. Brock, “Tuning the optical band gap of quantum dot assemblies by varying network density,” *ACS Nano*, vol. 3, no. 7, pp. 2000–

- 2006, 2009.
- [139] A. Hitihami-Mudiyanselage, K. Senevirathne, and S. L. Brock, "Assembly of phosphide nanocrystals into porous networks: Formation of InP gels and aerogels," *ACS Nano*, vol. 7, no. 2, pp. 1163–1170, 2013.
- [140] S. Pawsey, K. K. Kalebaila, I. Moudrakovski, J. A. Ripmeester, and S. L. Brock, "Pore structure and interconnectivity of CdS aerogels and xerogels by hyperpolarized xenon NMR," *J. Phys. Chem. C*, vol. 114, no. 31, pp. 13187–13195, 2010.
- [141] H. Yu and S. L. Brock, "Effects of nanoparticle shape on the morphology and properties of porous CdSe assemblies (aerogels)," *ACS Nano*, vol. 2, no. 8, pp. 1563–1570, 2008.
- [142] L. Nahar and I. U. Arachchige, "Sol-Gel Methods for the Assembly of Metal and Semiconductor Nanoparticles," *JSM Nanotechnol Nanomed*, vol. 1, no. 1, pp. 1004 (1–6), 2013.
- [143] S. Bag, I. U. Arachchige, and M. G. Kanatzidis, "Aerogels from metal chalcogenides and their emerging unique properties," *J. Mater. Chem.*, vol. 18, no. 31, pp. 3628–3632, 2008.
- [144] I. U. Arachchige and S. L. Brock, "Sol-gel methods for the assembly of metal chalcogenide quantum dots," *Acc. Chem. Res.*, vol. 40, no. 9, pp. 801–809, 2007.
- [145] L. Korala, Z. Wang, Y. Liu, S. Maldonado, and S. L. Brock, "Uniform thin films of CdSe and CdSe(ZnS) core(shell) quantum dots by sol-gel assembly: Enabling photoelectrochemical characterization and electronic applications," *ACS Nano*, vol. 7, no. 2, pp. 1215–1223, 2013.
- [146] M. R. Gaeeni, M. Tohidian, and M. Majles-Ara, "Green synthesis of CdSe colloidal nanocrystals with strong green emission by the sol-gel method," *Ind. Eng. Chem. Res.*, vol. 53, no. 18, pp. 7598–7603, 2014.
- [147] Y.-C. Pu and Y.-J. Hsu, "Multicolored Cd(1-x)Zn(x)Se quantum dots with type-I core/shell structure: single-step synthesis and their use as light emitting diodes," *Nanoscale*, vol. 6, no. 7, pp. 3881–3888, 2014.
- [148] R. K. Capek, D. Yanover, and E. Lifshitz, "Size control by rate control in colloidal PbSe quantum dot synthesis," *Nanoscale*, vol. 7, no. 12, pp. 5299–5310, 2015.

- [149] C. Burda, X. Chen, R. Narayanan, and M. A. El-Sayed, "Chemistry and Properties of Nanocrystals of Different Shapes," *Chem. Rev.*, vol. 105, no. 4, pp. 1025–1102, 2005.
- [150] R. Li, Z. Ye, W. Kong, H. Wu, X. Lin, and W. Fang, "Controllable synthesis and growth mechanism of dual size distributed PbSe quantum dots," *RSC Adv.*, vol. 5, no. 3, pp. 1961–1967, 2015.
- [151] B. Gao, C. Shen, S. Yuan, Y. Yang, and G. Chen, "Synthesis of highly emissive CdSe quantum dots by aqueous precipitation method," *J. Nanomater.*, vol. 2013, pp. 4–11, 2013.
- [152] M. Wang *et al.*, "Fluorescence enhancement detection of uric acid based on water-soluble 3-mercaptopropionic acid-capped core/shell ZnS:Cu/ZnS," *RSC Adv.*, vol. 4, no. 48, pp. 25183–25188, 2014.
- [153] Y. Chang *et al.*, "Preparation of highly luminescent BaSO₄ protected CdTe quantum dots as conversion materials for excellent color-rendering white LEDs," *J. Mater. Chem. C*, vol. 3, no. 12, pp. 2831–2836, 2015.
- [154] Y. Chang *et al.*, "A water–ethanol phase assisted co-precipitation approach toward high quality quantum dot–inorganic salt composites and their application for WLEDs," *Green Chem.*, vol. 17, no. 8, pp. 4439–4445, 2015.
- [155] L. Tan, A. Wan, T. Zhao, R. Huang, and H. Li, "Aqueous synthesis of multidentate-polymer-capping Ag₂Se quantum dots with bright photoluminescence tunable in a second near-infrared biological window," *ACS Appl. Mater. Interfaces*, vol. 6, no. 9, pp. 6217–6222, 2014.
- [156] A. S. Kumari, K. G. Mangatayaru, and G. Veerabhadram, "Synthesis , Characterization of ZnS nanoparticles by Coprecipitation method using various capping agents - Photocatalytic activity and Kinetic study," *IOSR J. Appl. Chem.*, vol. 6, no. 1, pp. 1–9, 2013.
- [157] A. Rahdar, H. A. Eivari, and R. Sarhaddi, "Study of structural and optical properties of ZnS : Cr nanoparticles synthesized by co-precipitation method," *Indian J. Sci. Technol.*, vol. 5, no. 1, pp. 1855–1858, 2012.
- [158] A. M. Jagtap, J. Khatei, and K. S. Koteswara Rao, "Exciton-phonon scattering and nonradiative relaxation of excited carriers in hydrothermally synthesized CdTe quantum dots," *Phys Chem Chem Phys*, vol. 17, no. 41, pp. 27579–27587,

- 2015.
- [159] D. Zhao, J.-T. Li, F. Gao, C. Zhang, and Z. He, “Facile synthesis and characterization of highly luminescent UV-blue-emitting ZnSe/ZnS quantum dots via a one-step hydrothermal method,” *RSC Adv.*, vol. 4, no. 87, pp. 47005–47011, 2014.
- [160] L. Yang, J. Zhu, and D. Xiao, “Microemulsion-mediated hydrothermal synthesis of ZnSe and Fe-doped ZnSe quantum dots with different luminescence characteristics,” *RSC Adv.*, vol. 2, no. 21, pp. 8179–8188, 2012.
- [161] H. Han, G. Di Francesco, and M. M. Maye, “Size Control and Photophysical Properties of Quantum Dots Prepared via a Novel Tunable Hydrothermal Route,” *J. Phys. Chem. C*, vol. 114, no. 45, pp. 19270–19277, 2010.
- [162] C. Ma *et al.*, “One-step hydrothermal synthesis of cobalt and potassium codoped CdSe quantum dots with high visible light photocatalytic activity,” *CrystEngComm*, vol. 17, no. 7, pp. 1701–1709, 2015.
- [163] W. C. Liu, B. L. Guo, X. S. Wu, F. M. Zhang, C. L. Mak, and K. H. Wong, “Facile hydrothermal synthesis of hydrotropic Cu₂ZnSnS₄ nanocrystal quantum dots: band-gap engineering and phonon confinement effect,” *J. Mater. Chem. A*, vol. 1, no. 9, pp. 3182–3186, 2013.
- [164] J. Cheng, X. Zhou, and H. Xiang, “Fluorescent metal ion chemosensors via cation exchange reactions of complexes, quantum dots, and metal–organic frameworks,” *Analyst*, vol. 140, no. 21, pp. 7082–7115, 2015.
- [165] Z. Deng, F. L. Lie, S. Shen, I. Ghosh, M. Mansuripur, and A. J. Muscat, “Water-based route to ligand-selective synthesis of ZnSe and Cd-doped ZnSe quantum dots with tunable ultraviolet A to blue photoluminescence,” *Langmuir*, vol. 25, no. 1, pp. 434–442, 2009.
- [166] A. Nag, J. Kundu, and A. Hazarika, “Seeded-growth, nanocrystal-fusion, ion-exchange and inorganic-ligand mediated formation of semiconductor-based colloidal heterostructured nanocrystals,” *CrystEngComm*, vol. 16, no. 40, pp. 9391–9407, 2014.
- [167] A. Jaiswal, S. S. Ghosh, and A. Chattopadhyay, “Quantum dot impregnated-chitosan film for heavy metal ion sensing and removal,” *Langmuir*, vol. 28, no. 44, pp. 15687–15696, 2012.

- [168] G. Trevisi, L. Seravalli, P. Frigeri, and S. Franchi, “Low density InAs/(In)GaAs quantum dots emitting at long wavelengths,” *Nanotechnology*, vol. 20, no. 41, p. 415607, 2009.
- [169] W. C. Fan *et al.*, “Magneto-optical properties of ZnMnTe/ZnSe quantum dots,” *J. Cryst. Growth*, vol. 323, no. 1, pp. 380–382, 2011.
- [170] Q. Chen *et al.*, “A new route toward light emission from Ge: tensile-strained quantum dots,” *Nanoscale*, vol. 7, no. 19, pp. 8725–8730, 2015.
- [171] H. Groiss *et al.*, “Size control and midinfrared emission of epitaxial PbTeCdTe quantum dot precipitates grown by molecular beam epitaxy,” *Appl. Phys. Lett.*, vol. 91, no. 22, p. 222106, 2007.
- [172] M. J. Humphry, B. Kraus, a. C. Hurst, a. M. Maiden, and J. M. Rodenburg, “Ptychographic electron microscopy using high-angle dark-field scattering for sub-nanometre resolution imaging,” *Nat. Commun.*, vol. 3, p. 730, 2012.
- [173] H. Yang, W. Luan, S. Tu, and Z. M. Wang, “Synthesis of nanocrystals via microreaction with temperature gradient: towards separation of nucleation and growth,” *Lab Chip*, vol. 8, no. 3, pp. 451–455, 2008.
- [174] A. B. Shah *et al.*, “High-index facets in gold nanocrystals elucidated by coherent electron diffraction,” *Nano Lett.*, vol. 13, no. 4, pp. 1840–1846, 2013.
- [175] Z. Hens and I. Moreels, “Light absorption by colloidal semiconductor quantum dots,” *J. Mater. Chem.*, vol. 22, no. 21, pp. 10406–10415, 2012.
- [176] A. L. Patterson, “The scherrer formula for X-ray particle size determination,” *Phys. Rev.*, vol. 56, no. 10, pp. 978–982, 1939.
- [177] V. Mote, Y. Purushotham, and B. Dole, “Williamson-Hall analysis in estimation of lattice strain in nanometer-sized ZnO particles,” *J. Theor. Appl. Phys.*, vol. 6, no. 1, pp. 2–9, 2012.
- [178] K. A. Aly, N. M. Khalil, Y. Algamal, and Q. M. A. Saleem, “Estimation of lattice strain for zirconia nano-particles based on Williamson- Hall analysis,” *Mater. Chem. Phys.*, vol. 193, pp. 182–188, 2017.
- [179] E. A. Davis and N. F. Mott, “Conduction in non-crystalline systems V. Conductivity, optical absorption and photoconductivity in amorphous semiconductors,” *Philos. Mag.*, vol. 22, no. 179, pp. 903–922, 1970.
- [180] Fridman, “Optical Properties and Electronic Structure of Amorphous

- Germanium,” *Phys. Status Solidi*, vol. 15, no. 2, pp. 627–637, 1966.
- [181] D. J. Griffiths, *Introduction to Quantum Mechanics*. Prentice Hall: Upper Saddle River, 1995.
- [182] J. Wang *et al.*, “Tetragonal - Orthorhombic - Cubic phase transitions in Ag₂Se nanocrystals,” *Chem. Mater.*, vol. 26, no. 19, pp. 5647–5653, 2014.
- [183] B. Gates *et al.*, “Synthesis and Characterization of Crystalline Ag₂Se Nanowires Through a Template-Engaged Reaction at Room Temperature,” *Adv. Funct. Mater.*, vol. 12, no. 10, pp. 679–686, 2002.
- [184] A. Sahu, D. Braga, O. Waser, M. S. Kang, D. Deng, and D. J. Norris, “Solid-Phase Flexibility in Ag₂Se Semiconductor Nanocrystals,” *Nano Lett.*, vol. 14, no. 1, pp. 115–121, 2014.
- [185] F. X. Yang, F. X. Liu, and X. L. Yu, “Synthesis and Optimum of Silver Selenide Nanopowder via Room Temperature Conversion Method,” *Adv. Mater. Res.*, vol. 535–537, pp. 349–352, 2012.
- [186] R. Xie, M. Rutherford, and X. Peng, “Formation of high-quality I-III-VI semiconductor nanocrystals by tuning relative reactivity of cationic precursors,” *J. Am. Chem. Soc.*, vol. 131, no. 15, pp. 5691–5697, 2009.
- [187] A. Tubtintae, M. W. Lee, and G. J. Wang, “Ag₂Se quantum-dot sensitized solar cells for full solar spectrum light harvesting,” *J. Power Sources*, vol. 196, no. 15, pp. 6603–6608, 2011.
- [188] D. T. Schoen, C. Xie, and Y. Cui, “Electrical switching and phase transformation in silver selenide nanowires,” *J. Am. Chem. Soc.*, vol. 129, no. 14, pp. 4116–4117, 2007.
- [189] S.-Y. Zhang, C. Fang, W. Wei, B. Jin, Y. Tian, and Y. Shen, “Synthesis and Electrochemical Behavior of Crystalline Ag₂Se Nanotubes,” *J. Phys. Chem. C*, vol. 111, pp. 4168–4174, 2007.
- [190] A. Husmann, J. B. Betts, G. S. Boebinger, A. Migliori, T. F. Rosenbaum, and M. L. Saboungi, “Megagauss sensors,” *Nature*, vol. 417, no. 6887, pp. 421–424, 2002.
- [191] M. T. Ng, C. Boothroyd, and J. J. Vittal, “Shape and size control of Ag₂Se nanocrystals from a single precursor [(Ph₃P)₃Ag₂(SeC{O}Ph)₂],” *Chem. Commun.*, vol. 2, no. 30, pp. 3820–3822, 2005.

- [192] M. Ferhat and J. Nagao, “Thermoelectric and transport properties of β -Ag₂Se compounds,” *J. Appl. Phys.*, vol. 88, no. 2, pp. 813–816, 2000.
- [193] W. Wang, Y. Geng, Y. Qian, M. Ji, and Y. Xie, “Novel room temperature method to nanocrystalline Ag₂Se,” *Mater. Res. Bull.*, vol. 34, no. 6, pp. 877–882, 1999.
- [194] M. Jafari, M. Salavati-Niasari, K. Saberyan, and H. Sabarou, “A Simple Sonochemical Route for Synthesis Silver Selenide Nanoparticles From SeCl₄ and Silver Salicylate,” *Synth. React. Inorganic, Met. Nano-Metal Chem.*, vol. 45, no. 1, pp. 58–67, 2015.
- [195] J. Hu *et al.*, “Hydrothermal growth of β -Ag₂Se tubular crystals,” *Chem. Commun.*, vol. 2000, no. 8, pp. 715–716, 2000.
- [196] M. Kristl, S. Gyergyek, and J. Kristl, “Synthesis and characterization of nanosized silver chalcogenides under ultrasonic irradiation,” *Mater. Express*, vol. 5, no. 4, pp. 359–366, 2015.
- [197] P. Bindu and S. Thomas, “Estimation of lattice strain in ZnO nanoparticles: X-ray peak profile analysis,” *J. Theor. Appl. Phys.*, vol. 8, no. 4, pp. 123–134, 2014.
- [198] V. Mote, Y. Purushotham, and B. Dole, “Williamson-Hall analysis in estimation of lattice strain in nanometer-sized ZnO particles,” *J. Theor. Appl. Phys.*, vol. 6, no. 1, p. 6, 2012.
- [199] V. Bilgin, S. Kose, F. Atay, and I. Akyuz, “The effect of substrate temperature on the structural and some physical properties of ultrasonically sprayed CdS films,” *Mater. Chem. Phys.*, vol. 94, no. 1, pp. 103–108, 2005.
- [200] D. W. Ayele, “A facile one-pot synthesis and characterization of Ag₂Se nanoparticles at low temperature,” *Egypt. J. Basic Appl. Sci.*, vol. 3, no. 2, pp. 149–154, 2016.
- [201] D. S. MORE, M. J. MOLOTO, and N. MOLOTO, “Hexadecylamine-capped silver selenide nanoparticles: temperature study,” *Chalcogenide Lett.*, vol. 13, no. 5, pp. 233–238, 2016.
- [202] M. C. S. KUMAR and B. PRADEEP, “Optical constants of co-evaporated Ag₂Se thin films with proton irradiation,” *J. Ovonic Res.*, vol. 6, no. 3, pp. 143–148, 2010.
- [203] G. Pellegrini, G. Mattei, and P. Mazzoldi, “Finite depth square well model:

- Applicability and limitations,” *J. Appl. Phys.*, vol. 97, no. 7, 2005.
- [204] I. Hocaoglu *et al.*, “Emission tunable, cyto/hemocompatible, near-IR-emitting Ag₂S quantum dots by aqueous decomposition of DMSA,” *Nanoscale*, vol. 6, no. 20, pp. 11921–11931, 2014.
- [205] P. Jiang, Z. Tian, and C. Zhu, “Emission-tunable near-infrared Ag₂S quantum dots,” *Chem. Mater.*, vol. 24, pp. 3–5, 2012.
- [206] J. Amaya Suárez, J. J. Plata, A. M. Márquez, and J. Fernández Sanz, “Ag₂S Quantum Dot-Sensitized Solar Cells by First Principles: The Effect of Capping Ligands and Linkers,” *J. Phys. Chem. A*, vol. 121, no. 38, pp. 7290–7296, 2017.
- [207] H. Shen, X. Jiao, D. Oron, J. Li, and H. Lin, “Efficient electron injection in non-toxic silver sulfide (Ag₂S) sensitized solar cells,” *J. Power Sources*, vol. 240, pp. 8–13, 2013.
- [208] Y. Guo *et al.*, “Improved performance in Ag₂S/P3HT hybrid solar cells with a solution processed SnO₂ electron transport layer,” *RSC Adv.*, vol. 6, no. 81, pp. 77701–77708, 2016.
- [209] J. Xue *et al.*, “Recent progress in synthetic methods and applications in solar cells of Ag₂S quantum dots,” *Mater. Res. Bull.*, vol. 106, pp. 113–123, 2018.
- [210] S. I. Sadovnikov, A. I. Gusev, and A. A. Rempel, “Artificial silver sulfide Ag₂S: Crystal structure and particle size in deposited powders,” *Superlattices Microstruct.*, vol. 83, pp. 35–47, 2015.
- [211] P. Vashishtat, I. Ebbsjo, R. Dejus, and K. Skold, “Ionic motion in superionic ag₂s,” *J. Phys. C Solid State Phys.*, vol. 18, no. 11, pp. L291–L296, 1985.
- [212] W. Andreoni, “Microscopic model of β -Ag₂S,” *Solid State Commun.*, vol. 38, no. 9, pp. 837–839, Jun. 1981.
- [213] S. Hull, D. A. Keen, D. S. Sivia, P. A. Madden, and M. Wilson, “The high-temperature superionic behaviour of Ag₂S,” *J. Physics-Condensed Matter*, vol. 14, no. 1, pp. L9–L17, 2002.
- [214] S. I. Sadovnikov and A. I. Gusev, “Universal approach to the synthesis of silver sulfide in the forms of nanopowders, quantum dots, Core-Shell Nanoparticles, and Heteronanostructures,” *Eur. J. Inorg. Chem.*, vol. 2016, no. 31, pp. 4944–4957, 2016.
- [215] A. Khare, A. W. Wills, L. M. Ammerman, D. J. Norris, and E. S. Aydil, “Size

- control and quantum confinement in $\text{Cu}_2\text{ZnSnS}_4$ nanocrystals,” *Chem. Commun.*, vol. 47, no. 42, pp. 11721–11723, 2011.
- [216] C. B. Murray, C. R. Kagan, and M. G. Bawendi, “Self-organization of CdSe nanocrystallites into three-dimensional quantum dot superlattices,” *Science (80-.)*, vol. 270, no. 5240, pp. 1335–1338, 1995.
- [217] W. P. Lim, Z. Zhang, H. Y. Low, and W. S. Chin, “Preparation of Ag₂S nanocrystals of predictable shape and size,” *Angew. Chemie - Int. Ed.*, vol. 43, no. 42, pp. 5685–5689, 2004.
- [218] Y. Shen, M. Y. Gee, and A. B. Greytak, “Purification technologies for colloidal nanocrystals,” *Chem. Commun.*, vol. 53, no. 5, pp. 827–841, 2017.
- [219] B. Hou, D. Parker, G. P. Kissling, J. A. Jones, D. Cherns, and D. J. Fermin, “Structure and Band Edge Energy of Highly Luminescent CdSe(1-x)Te(x) Alloyed Quantum Dots,” *J. Phys. Chem. C*, vol. 117, no. 13, pp. 6814–6820, 2013.
- [220] A. J. Frueh, “The crystallography of silver sulphide, Ag₂S,” *Zeitschrift für Krist.*, vol. 110, no. 1–6, pp. 136–144, 1958.
- [221] D. Santamaría-Pérez *et al.*, “Compression of silver sulfide: X-ray diffraction measurements and total-energy calculations,” *Inorg. Chem.*, vol. 51, no. 9, pp. 5289–5298, 2012.
- [222] P. Wang, R. Zhao, L. Wu, and M. Zhang, “Effect of Y doping on high-pressure behavior of Ag₂S nanocrystals,” *RSC Adv.*, vol. 7, no. 56, pp. 35105–35110, 2017.
- [223] L. Tan, S. Liu, Q. Yang, and Y. Shen, “Facile assembly of oppositely charged silver sulfide nanoparticles into photoluminescent mesoporous nanospheres,” *Langmuir*, vol. 31, no. 13, pp. 3958–3964, 2015.
- [224] H. Meherzi-Maghraoui *et al.*, “Structural , optical and transport properties of Ag₂S films deposited chemically from aqueous solution,” *Thin Solid Films*, vol. 288, pp. 217–223, 1996.
- [225] P. Lalanne and J. P. Hugonin, “Interaction between optical nano-objects at metallo-dielectric interfaces,” *Nat. Phys.*, vol. 2, no. 8, pp. 551–556, 2006.
- [226] I. Martina, R. Wiesinger, and M. Schreiner, “Micro-Raman Characterisation of Silver Corrosion Products : Instrumental Set Up and Reference Database,” *e-*

- Preservation Sci.*, vol. 9, pp. 1–8, 2012.
- [227] Y. Gao, X. Zhao, P. Yin, and F. Gao, “Size-Dependent Raman Shifts for nanocrystals,” *Sci. Rep.*, vol. 6, no. 1, p. 20539, 2016.
- [228] G. Marucci, A. Monno, and I. D. van der Werf, “Non invasive micro-Raman spectroscopy for investigation of historical silver salt gelatin photographs,” *Microchem. J.*, vol. 117, no. November, pp. 220–224, 2014.
- [229] O. Alekperov, Z. Jahangirli, and R. Paucar, “First-principles lattice dynamics and Raman scattering in ionic conductor β -Ag₂S,” *Phys. Status Solidi*, vol. 253, no. 10, pp. 2049–2055, 2016.
- [230] R. E. Bailey and S. Nie, “Alloyed semiconductor quantum dots: Tuning the optical properties without changing the particle size,” *J. Am. Chem. Soc.*, vol. 125, no. 23, pp. 7100–7106, 2003.
- [231] L. A. Swafford *et al.*, “Homogeneously alloyed CdS_xSe_{1-x} nanocrystals: Synthesis, characterization, and composition/size-dependent band gap,” *J. Am. Chem. Soc.*, vol. 128, no. 37, pp. 12299–12306, 2006.
- [232] W. Ma, J. M. Luther, H. Zheng, Y. Wu, and A. P. Alivisatos, “Photovoltaic Devices Employing Ternary PbS_xSe_{1-x} Nanocrystals,” *Nano Lett.*, vol. 9, no. 4, pp. 1699–1703, 2009.
- [233] J. Zhang *et al.*, “Bright Gradient-Alloyed CdSe_xS_{1-x} quantum Dots Exhibiting Cyan-Blue Emission,” *Chem. Mater.*, vol. 28, no. 2, pp. 618–625, 2016.
- [234] R. Tang, J. Xue, B. Xu, D. Shen, G. P. Sudlow, and S. Achilefu, “Tunable Ultrasmall Visible-to- Extended Near-Infrared Emitting Silver Sulfide Quantum Dots for Integrin-Targeted Cancer Imaging,” *ACS Nano*, vol. 9, no. 1, pp. 220–230, 2015.
- [235] M. Y. Qin *et al.*, “In vivo cancer targeting and fluorescence-CT dual-mode imaging with nanoprobe based on silver sulfide quantum dots and iodinated oil,” *Nanoscale*, vol. 7, no. 46, pp. 19484–19492, 2015.
- [236] M. R. Kim and D. Ma, “Quantum-dot-based solar cells: Recent advances, strategies, and challenges,” *J. Phys. Chem. Lett.*, vol. 6, pp. 85–99, 2015.
- [237] A. R. Denton and N. W. Ashcroft, “Vegards law,” *Phys. Rev. A*, vol. 43, no. 6, pp. 3161–3164, 1991.
- [238] S. I. Sadovnikov, A. I. Gusev, and A. A. Rempel, “Nanocrystalline silver sulfide

- Ag₂S,” *Rev. Adv. Mater. Sci.*, vol. 41, pp. 7–19, 2015.
- [239] L. Tan, A. Wan, and H. Li, “Ag₂S quantum dots conjugated chitosan nanospheres toward light-triggered nitric oxide release and near-infrared fluorescence imaging,” *Langmuir*, vol. 29, no. 48, pp. 15032–15042, 2013.
- [240] L. Tan, A. Wan, and H. Li, “Conjugating S-nitrosothiols with glutathione stabilized silver sulfide quantum dots for controlled nitric oxide release and near-infrared fluorescence imaging,” *ACS Appl. Mater. Interfaces*, vol. 5, p. 11163–11171, 2013.
- [241] K. P. Remya, T. Udayabhaskararao, and T. Pradeep, “Low-Temperature Thermal Dissociation of Ag Quantum Clusters in Solution and Formation of Monodisperse Ag₂S Nanoparticles,” *J. Phys. Chem. C*, vol. 116, no. 49, pp. 26019–26026, 2012.
- [242] C. Ji *et al.*, “Synthesis and characterization of Ag₂S_xSe_{1-x} nanocrystals and their photoelectrochemical property,” *Nanotechnology*, vol. 28, no. 6, p. 065602, 2017.
- [243] S. N. Mostafa and M. A. Abd-Elreheem, “Electrochemical Investigations on silver sulphide,” *Electrochim. Acta*, vol. 30, no. 5, pp. 635–639, May 1985.
- [244] A. Sahu, A. Khare, D. D. Deng, and D. J. Norris, “Quantum confinement in silver selenide semiconductor nanocrystals,” *Chem. Commun.*, vol. 48, no. 44, pp. 5458–5460, 2012.
- [245] V. V. Gorbachev and I. M. Putilin, “The effective mass of charge carriers in Ag₂Se,” *Phys. Status Solidi*, vol. 69, no. 2, pp. K153–K156, 1975.
- [246] B. Ramezanloo, M. Molaei, and M. Karimipour, “Red emissive Ag₂Se quantum dots (QDs) with room-temperature synthesis of both orthorhombic and superionic cubic phases via stirring approach,” *J. Lumin.*, vol. 204, pp. 419–423, 2018.
- [247] C. M. Fang, R. A. De Groot, and G. A. Wieggers, “Ab initio band structure calculations of the low-temperature phases of Ag₂Se, Ag₂Te and Ag₃AuSe₂,” *J. Phys. Chem. Solids*, vol. 63, no. 3, pp. 457–464, 2002.
- [248] F. W. Wise, “Lead salt quantum dots: The limit of strong quantum confinement,” *Acc. Chem. Res.*, vol. 33, no. 11, pp. 773–780, 2000.
- [249] M. Pandiaraman and N. Soundararajan, “Micro-Raman studies on thermally

- evaporated Ag₂Se thin films,” *J. Theor. Appl.*, vol. 6, no. 1, pp. 1–5, 2012.
- [250] A. Ali and W.-C. Oh, “Synthesis of Ag₂Se–graphene–TiO₂ nanocomposite and analysis of photocatalytic activity of CO₂ reduction to CH₃OH,” *Bull. Mater. Sci.*, vol. 40, no. 7, pp. 1319–1328, 2017.
- [251] P. Naumov, O. Barkalov, H. Mirhosseini, C. Felser, and S. A. Medvedev, “Atomic and electronic structures evolution of the narrow band gap semiconductor Ag₂Se under high pressure,” *J. Phys. Condens. Matter*, vol. 28, no. 38, p. 385801, 2016.

